LARAMIDE SHORTENING IN THE CLARK MOUNTAIN THRUST COMPLEX: REINTERPRETATION OF THE TIMING OF THE WINTERS PASS THRUST, MOJAVE DESERT, SE CALIFORNIA

By

Hayden M. Kombrink

Bachelor of Science – Earth and Space Exploration
Arizona State University
2019

A thesis submitted in partial fulfillment
of the requirements for the

Master of Science – Geoscience

Department of Geoscience
College of Sciences
The Graduate College

University of Nevada, Las Vegas
May 2024

Copyright by Hayden M. Kombrink 2024
All Rights Reserved

Thesis Approval

The Graduate College
The University of Nevada, Las Vegas

April 5, 2024

This thesis prepared by

Hayden M. Kombrink

entitled

Laramide Shortening in the Clark Mountain Thrust Complex: Reinterpretation of the Timing of the Winters Pass Thrust, Mojave Desert, SE California

is approved in partial fulfillment of the requirements for the degree of

Master of Science – Geoscience
Department of Geoscience

Michael Wells, Ph.D.
Examination Committee Chair

Andrew Martin, Ph.D.
Examination Committee Member

Kevin Konrad, Ph.D.
Examination Committee Member

George Rhee, Ph.D.
Graduate College Faculty Representative

Alyssa Crittenden, Ph.D.
Vice Provost for Graduate Education & Dean of the Graduate College

ABSTRACT

The transition to flat slab subduction, around ~90-80 Ma during the Laramide orogeny, marks a pivotal shift in the style of deformation for the North American Cordillera. Late Cretaceous deformation associated with the change in subduction angle is observed throughout the Mojave, paradoxically manifesting as extensional strain deforming the thickened crust formed during the Sevier orogeny. The Winters Pass thrust, located in the Mesquite Mountains of southeastern California, has long been regarded to be the southern continuation of the Wheeler Pass thrust of the NW Spring Mountains, 50 km to the north, and the northern continuation of the Pachalka thrust, 20 km to the south in the Clark Mountains. This study uses $^{40}Ar/^{39}Ar$ geochronology on synkinematic muscovite to provide direct geochronologic constraints on mylonitic deformation for the Winters Pass, Powerline Road and Pachalka thrusts. Structural data paired with kinematic and microstructural data from petrographic and SEM observations, and data collected with electron backscatter diffraction on recrystallized quartz allows for temperatures of deformation, the geometry of the thrust complex and transport direction of the upper-plate(s) to be determined. This study provides deformation timing constraints of ~73 Ma for the Winters Pass thrust, ~81 Ma for the Powerline Road thrust, and looser constraints on the Pachalka thrust of ~70-85 Ma. Structural data shows an overall NE-E direction of transport for the upper plate. These data suggest that these faults record a Laramide thrust complex with a backwards-breaking thrust sequence and are not correlative to any thrusts of the southern Sevier fold-thrust-belt in the Spring Mountains. We discuss possible drivers of contractional strain in the Mojave during this time and suggest that subduction of the conjugate Shatsky Rise paired with the proximity of the paleo rift-margin played a critical role in the unique style and age of deformation that is reported herein for this portion of the eastern Mojave Desert.

ACKNOWLEDGMENTS

The past two and a half years here at UNLV have been arguably the most transformative years of my adult life to this point. The pursuit of this degree has given me the ability to challenge myself intellectually, has helped me to discover my full potential, and has allowed me to develop professional and personal skills that I will be able to use for the rest of my life. Through my years here I have been able to create friendships that will last a life-time, discover new passions, and has given me unparalleled knowledge in a field that I am very passionate about. I would like to thank Dr. Michael Wells for the knowledge, support, patience, and friendship that he has given me during my time here at UNLV. He was always happy to share his expertise and knowledge with me to help me tackle any challenges that came my way. His door was always open to answer any questions, no matter how trivial or senseless they may have been and was always someone that I was able to talk to. I could not have asked for a more humble, knowledgeable, and supportive advisor and am grateful for all he has done for me and the friendship that we have gained. I would also like to thank the rest of my committee members, including Dr. Kevin Konrad and Dr. Andrew Martin. Kevin and Andrew were always happy to share their knowledge with me and were always able to provide good conversation during the middle of a long day. It seems there is nothing about geochronology that Kevin doesn't know and am grateful for his patience and willingness to answer any questions I had.

Most importantly I would like to thank my family for supporting me through these last couple of years. Whilst being spread across the country, my parents and two sisters have given me so much support though out my entire time here. I am very grateful to have a family that cares so much and wants to see me succeed. I would not have been able to do it without any of you. My girlfriend Casey has been extremely supportive and patient with me, especially during

the chaos and seemingly non-stop work these last two semesters. I would not be where I am today without her love and support.

I also can't thank my friends enough for their support, those here in Las Vegas and those everywhere. Having people to call and chat with no matter the distance made such a huge difference and was a big stress reliever. The friends I have made here, many of which were prior grad students here at UNLV helped to make UNLV and Las Vegas feel like home. They were always happy to help support me in any way they could. Having a group of peers to talk to, ask for help, and to become friends with helped me to feel right at home within the first few days of moving to Las Vegas and I could not be more grateful for that. I will always consider Las Vegas home away from home.

TABLE OF CONTENTS

ABSTRACT……..iii

ACKNOWLEDGEMENTS…….....iv

LIST OF FIGURES……viii

INTRODUCTION…….…1

TECTONIC SETTING…….4

GEOLOGY OF THE MESQUITE MOUNTAINS……9

METHODS……...13

Structural Mapping…….....13

Petrography/Microstructures……..…...14

Electron Backscatter Diffraction……....16

$^{40}Ar/^{39}Ar$ Geochronology…….....20

RESULTS…….24

Structure and Field…….....24

Petrography and Microstructures……..27

Electron Backscatter Diffraction……....29

$^{40}Ar/^{39}Ar$ Geochronology…….....34

DISCUSSION……...36

Precambrian Rift Geometry……...36

Age Constraints on Mylonitic Deformation……..37

Miocene Extensional Overprint……..41

Tectonic Driver for Cretaceous Contraction in the Mojave ……..43

CONCLUSION……47

APPENDICES……..50

Appendix A: Figures……....50

Appendix B: Muscovite $^{40}Ar/^{39}Ar$ Geochronology Data Tables……82

Appendix C: EDS Elemental Spectra……....90

Appendix D: IPF-z Maps and Key for EBSD samples……98

Appendix E: Grain Size Distribution Histograms……..102

Appendix F: Sample Location.....105

REFERENCES……...106

CURRICULUM VITAE……....121

LIST OF FIGURES

Figure 1. Geo-tectonic map of North America.....58

Figure 2. Simplified geologic map of the Mojave with pre-Tertiary reconstruction.....59

Figure 3. Geologic map of the NW Mesquite Mountains.....60

Figure 4. Geologic cross-sections of the NW Mesquite Mountains.....61

Figure 5. Stereonet data for the NW Mesquite Mountains.....62

Figure 6. Slip systems in quartz and associated c-axis pole figures.....63

Figure 7. EBSD and geochronology locations for the NW Mesquite Mountains.....64

Figure 8. EBSD and geochronology locations for the Clark Mountains.....65

Figure 9. Final muscovite mineral separates used for $^{40}Ar/^{39}Ar$ geochronology.....66

Figure 10. Kinematic indicators in the field.....67

Figure 11. Kinematic indicators in thin section.....68

Figure 12. Photomicrographs of feldspar reaction rims and cores to produce mica.....69

Figure 13. Low mag EDS maps of feldspar reaction rims.....70

Figure 14. High mag EDS maps of feldspar reaction rims.....71

Figure 15. Misorientation to mean maps.....72

Figure 16. CVA plots for different deformation geometries.....73

Figure 17. Bulk quartz CVA data for all samples.....74

Figure 18. Quartz CVA data on grains with accumulated misorientations.....75

Figure 19. Pole figures for quartz in the vorticity reference frame.....76

Figure 20. Inverse pole figures for quartz in the vorticity reference frame.....77

Figure 21. $^{40}Ar/^{39}Ar$ age spectra with K/Ca ratios for all samples.....78

Figure 22. Bulk age spectra for all muscovite separates.....79

Figure 23. Out-of-sequence thrust system.....80

Figure 24. Normal sequence of a propagating thrust system.....81

INTRODUCTION

The Sevier and Laramide orogenies are well-studied and important tectonic events in shaping North American Cordilleran geology. Thrust faults in the southernmost part of the Sevier fold-thrust belt (SFTB) provide insight into the tectonic history and paleogeography of the eastern Mojave Desert (Figures 1 and 2). Thrust faults in the southern SFTB are typically thin-skinned thrusts producing decollements that parallel stratigraphy and ramps that cut through sedimentary strata. In some cases, these thrusts may locally cut into basement rocks near buttresses and reentrants in the Proterozoic rifted margin such as seen in the southern Nopah Range (Giallorenzo et al., 2018) and the Powerline road thrust and Winters Pass thrusts (Burchfiel and Davis, 1971, 1981, 1988; Walker et al., 1995) as well as where the thrusts cut into the craton to the south (Burchfiel and Davis, 1981). In the eastern Mojave, these thrust faults typically involve Late Paleozoic to Proterozoic strata which provide a window into the Precambrian history of North America. Deformation associated with the Sevier orogeny is dated to the Jurassic to mid Cretaceous in the southern Sevier belt and is a result of convergence between the North American plate and Farallon oceanic plate (DeCelles, 2004; Giallorenzo et al., 2018). Late Cretaceous to Paleogene deformation related to the Laramide orogeny has not been recognized in the Mojave sector of the fold-thrust belt, with the exception of NE-vergent folds and thrusts that deform older thrusts in the Nopah and Resting Spring ranges that Pavlis et al. (2014) interpreted as Laramide structures.

The Wheeler Pass thrust is the dominant thrust in the Spring Mountains (Burchfiel et al., 1974; Wernicke et al., 1988) that carries the thick Neoproterozoic to Devonian passive margin sequence, and its timing of motion has recently been resolved to be Late Jurassic using zircon (U-Th)/He thermochronology showing hanging-wall cooling from 160-140 Ma. (Giallorenzo et

al., 2018). Previous workers have suggested that the Wheeler Pass thrust fault is correlative with the Winters Pass and Pachalka thrusts to the south (Wernicke et al., 1988; Walker et al., 1995; Snow and Wernicke, 2000), but these correlations have been inferred but not proven (Wernicke et al., 1988; Snow and Wernicke, 2000). The evidence used to make these correlations includes the following observations: 1) mylonites in the hanging wall of the Winters Pass fault show a top-to-the-northeast shear fabric, sharing an eastward component to the top-SE kinematics inferred for the Wheeler Pass thrust and the top-east kinematics of the Pachalka thrust, and more importantly, 2) both the Wheeler Pass and Winters Pass thrusts are the easternmost thrusts to carry the thicker transitional to passive margin Neoproterozoic to Early Cambrian stratigraphic section. However, data is lacking to definitively constrain the timing of motion for the Winters Pass thrust in the Kingston Range and Mesquite Mountains, CA (Figure 2). With the timing of the Pachalka thrust interpreted to be Late Jurassic (Walker et al., 1995), and the timing of the Wheeler Pass thrust sheet recently resolved to also be Late Jurassic (Giallorenzo et al., 2018) providing new age constraints for the Winters Pass thrust will allow the testing of this hypothesized thrust correlation. This study aims to characterize and determine the deformation history of the Winters Pass thrust to test the hypothesis that it is a Late Jurassic thrust and correlates to the Wheelers Pass thrust to the north and Pachalka thrust to the south.

Zircon (U-Th)/He thermochronology recently applied to the Wheeler Pass thrust sheet clarifies the timing of motion and shows exhumation and cooling from 160 to 140 Ma in the Spring Mountains and Resting Spring Range (Giallorenzo et al., 2018). This current study uses geochronometric data from $^{40}Ar/^{39}Ar$ incremental step-heating of synkinematic muscovite to directly determine the age of deformation of the rocks along the Winters Pass and Powerline Road thrusts, with initial exploratory work on the Pachalka thrust. The geometries and

kinematics of the fault systems paired with the direct dating of synkinematic minerals in the fault rocks will allow for the speculated correlation with the Jurassic Wheelers Pass thrust to be verified or falsified. An additional interest is to better resolve the influence of the Proterozoic rift architecture on superimposed deformation kinematics of the SFTB.

One question that is addressed in this study is whether the mylonitic basement rocks in the Mesquite Mountains record Mesozoic thrust-sense kinematics or Miocene extensional kinematics. Burchfiel and Davis (1971) and Burchfiel et al. (1988) considered the mylonitic Proterozoic basement rocks to record top-to-the-NE shear related to emplacement of the Winters Pass thrust sheet, consistent with what would be expected during a Jurassic thrusting event. McMackin (1987), on the other hand, considered the rocks to record top-to-the-SW shear related to Miocene extension. New age constraints on deformation from $^{40}Ar/^{39}Ar$ experiments on synkinematic white mica point to a Late Cretaceous age of deformation. These new age constraints paired with structural analysis of the area point to a Late Cretaceous contractional deformation history in the eastern Mojave likely related to the subduction of the conjugate Shatsky Rise (CSR) and associated flat slab subduction during the Laramide orogeny.

TECTONIC SETTING

The southern Death Valley region preserves an exceptional record of tectonic history spanning the Precambrian to Holocene. Cratonal sedimentary rocks of the Neoproterozoic to Mesoproterozoic Pahrump Group are underlain by basement rocks of the Mojave Province dated to 1.7 Ga (Lanphere, 1964; Barth et al., 2000; Strickland et al., 2013). The Pahrump Group strata include the Crystal Springs Formation, Horse Thief Springs Formation, Beck Spring Dolomite and Kingston Peak Formation, whose depositional ages span from 1300 – 635 Ma (Mahon, 2014). The Pahrump Group was originally interpreted to have formed in the Armagosa aulacogen, a long west-northwest trending sedimentary basin (MacDonald, 2013; Mahon, 2014). However, it is now thought that the orientation of the basin is due to Cenozoic extension, and that the stratigraphy of the Pahrump Group was likely formed in intracratonic basins related to several distinct tectonic events including the formation and subsequent breakup of the supercontinent Rodinia (MacDonald et al., 2013; Mahon, 2014). The middle- and lower members of the Crystal Spring Formation suggest inboard deposition during the assembly of Rodinia in the Mesoproterozoic with a ca. 300 m.y. duration unconformity between the Crystal Spring Formation and Horse Thief Springs Formation. This unconformity suggests a period of tectonic quiescence followed by deposition of the Neoproterozoic Horsethief Springs Formation, Beck Spring Dolomite, and Kingston Peak Formation, indicating the onset of rifting along the western margin of Laurentia (Mahon, 2014).

Rifting of the supercontinent Rodinia has age constraints between 800-600 Ma (Mahon, 2014; Prave, 1999; Yonkee et al., 2014). Thick packages of sedimentary rocks deposited over top the Noonday Dolomite mark the formation of a passive margin and an associated sedimentary wedge that progressively thickens westward including an Ediacaran to Middle Cambrian clastic

wedge and a Middle Cambrian and younger carbonate succession, marking the transition from rift to drift tectonics (Prave, 1999; Wernicke et al., 1988). The Kingston Range and Mesquite Mountains have exposures of the Precambrian basement, Pahrump Group and Neoproterozoic to Middle Cambrian passive margin strata. Tectonic subsidence related to initial rifting was followed by protracted thermal subsidence (after the rift to drift transition) along the western margin of Laurentia, persisting throughout the Ediacaran and much of the Early Paleozoic and leading to development of a westward thickening clastic wedge followed by carbonate, producing a section >10km thick in the westernmost exposures (Stewart, 1970; Wright et al., 1976; McKenzie, 1978; Witkosky and Wernicke, 2018).

Passive margin sedimentation is first interrupted by the Late Paleozoic Antler orogeny, converting the passive margin into an episodic convergent margin including a period of strike-slip continental truncation during the Pennsylvanian-Permian ending with the Permo-Triassic Sonoman orogeny to the north and subduction initiation to the south (Stone and Stevens, 1988; Lawton et al., 2017; Levy et al., 2021). Following plate reorganization associated with the Jurassic Nevadan orogeny, the margin consolidated into an Andean-type convergent setting leading to the Sevier and Laramide orogenies (Burchfiel and Davis, 1972, 1975, 1992; DeCelles, 2004; Yonkee and Weil, 2015). Subduction of the Farallon plate during the Mesozoic caused development of a magmatic arc, and large-scale regional crustal thickening and metamorphism in the retroarc region including development of the Sevier fold-thrust belt in Neoproterozoic-Jurassic sedimentary rocks. In the area around the eastern Mojave, compressive stress during the Permian-Jurassic plastically and brittlely deforms sedimentary rocks and led to the development of four major E-vergent thrust sheets that displace the older passive margin sedimentary packages. Motion of these four thrust sheets progressively youngs eastward and include the

Marble Canyon sheet, Lemoigne sheet, Wheeler Pass sheet, and Keystone sheet respectively (Figure 2) (Snow and Wernicke, 2000; Giallorenzo et al., 2018). The thrust faults associated with these thrust sheets are thin-skinned, cutting through the sedimentary miogeoclinal wedge with ramp-flat geometries towards the north while to the south, western thrusts cut more steeply and locally involve crystalline basement (Burchfiel and Davis, 1975, 1981; Wernicke et al., 1988). Subduction associated with plate convergence during the Late Jurassic to Late Cretaceous led to the development of the Sierra Nevada Batholith and the Southern California batholith. Fluxes in magmatism within the Sierra Nevada and Southern California batholith are temporally associated with periods of shortening responsible for driving the retroarc hinterland and fold-thrust belt deformation that is associated with the Sevier orogeny (DeCelles et al., 2009). Changes in surface elevation alters the taper of the retroarc orogenic wedge. Increased hinterland elevation brings the orogenic wedge into supercritical taper which allows for the forward propagation of retroarc deformation along thrust faults, explaining the older to younger sequence of thrusting while moving west to east in the eastern Mojave. The Wheeler Pass thrust sheet is structurally the second highest thrust sheet in this system and is suggested to be correlative with the Winters Pass thrust and Pachalka thrust of the Mesquite and Clark Mountains block(s) (Burchfiel and Davis, 1971; Giallorenzo et al., 2018; Wernicke et al., 1988). Forward propagation of thrusts in the retroarc continued in the SFTB further north in Idaho-Utah-Wyoming into the Late Cretaceous to early Eocene during the transition to flat-slab subduction and the onset of the Laramide orogeny.

Suggested mechanisms to develop flat slab subduction include an increase in plate convergent velocity, an increase in the westward drift of the North American plate in a fixed mantle reference frame due to increased spreading rates along the Mid Atlantic Ridge,

hydrodynamic suction due to steps in lithospheric thickness in the overriding plate, an increase in buoyancy of the subducted slab; all of these factors have been suggested to have contributed to slab flattening during the Laramide (Engebretson et al., 1984; Liu and Currie, 2016; Saleeby, 2003; Jones et al., 2011; Yonkee and Weil, 2015). An increase in plate convergence rate would likely lead to a subduction rate that is faster than the slab sinking rate, thus lowering the slab angle. Another possible driver for slab flattening suggested by Jones et al. (2011) and Liu and Currie (2016) is a slab suction force due to a thick lithosphere beneath the Colorado Plateau. The increased thickness of the lithosphere beneath the Colorado Plateau would interrupt the mantle wedge flow that operates in a classic subduction system to produce a suction force that would lift the subducting slab into a flatter geometry and increase subsidence within the continental lithosphere. During the Late Cretaceous subduction of the Shatsky conjugate, an oceanic plateau, increased slab buoyancy may have contributed to the shallowing slab subduction angle from around 70-90 Ma which can be correlated to the oldest ages of Laramide-style deformation (Livaccari and Perry, 1993; Barth and Schneiderman, 1996; Saleeby, 2003). This timeframe coincides with forearc uplift and underplating of the Pelona–Orocopia–Rand schists as well as the shutoff of magmatism in the Sierra Nevada batholith suggesting that flat-slab subduction impeded the supply of asthenosphere needed to fuel the magmatic arc (Dumitru, 1991; Yonkee and Weil, 2015).

During the Cenozoic, plate reorganization transformed the convergent boundary of western North America into a transform boundary late in the history of rollback of the subducted low-angle Farallon slab. The combined effects of these geodynamic processes created isostatic instability and ultimately led to the gravitational collapse of now thickened continental lithosphere and large-scale regional extension; locally, this led to up to 200% extension

(Wernicke et al., 1988; Constenius, 1996; Christianson et al., 2007; Faulds et al., 2005). Much of the extension within the northern Basin and Range province likely can be attributed to the rollback of the Farallon plate which causes the southward migration of volcanism and lithospheric thinning accommodating most of the extension in Late Eocene to early Miocene time (Christianson et al., 2007). Extension in the central and southern Basin and Range is driven by both slab-rollback and the northward migration of the Mendocino triple junction (Furlong, 1984; Faulds et al., 2005). Around 12-10 Ma, strain partitioning into the Walker Lane fault system begins to accommodate a portion of the plate motion between the North American and Pacific plates along the western portion of the Basin and Range (Faulds et al., 2005). Around this time, it is likely that what were once two independent time-transgressive drivers of extension in different parts of the Basin and Range joined forces in the Central Basin and Range. The combined influence of slab rollback with the strain partitioning along the developing Walker Lane within middle to late Miocene is evidenced by the large-scale extension seen in the Las Vegas and Death Valley region where the crust is extended by up to 300% compared to a factor of only 200% in the Great Basin region (Wernickie et al., 1988). The transition to extensional tectonics displaced and disrupted the once continuous thrusts in the fold-thrust-belt across the Mojave into isolated mountain blocks. Discontinuous exposure of these Mesozoic structures has made thrust correlations difficult to resolve, but from these correlations allow for a pre-Tertiary reconstruction of the fold-thrust-belt to be determined (Figure 2) (Giallorenzo et al., 2018; Wernicke et al., 1988).

GEOLOGY OF THE MESQUITE MOUNTAINS

The Mesquite Mountains and Kingston Range of southeastern California are roughly 80 km southwest of Las Vegas, and 25 km northwest of Mountain Pass, California. This location is situated near the southernmost end of the SFTB, in the northwest part of the Clark Mountain thrust complex, where the contractile belt converges towards the south with the southern California Batholith portion of the Cordilleran magmatic arc and the East Sierran thrust system (Figure 1) (Walker et al., 1995; Giallorenzo et al. 2018). Structural geology around the northern Mesquite Mountains and southeastern Kingston Range is dominated by a long-lived fault system or boundary that is interpreted to have: (1) initiated as a basin-margin normal fault system during Late Precambrian continental rifting during the breakup of Rodinia, (2) localized a thrust fault (the Winters Pass thrust) during Mesozoic crustal shortening, and (3) was either reactivated by, or exhumed by the structurally higher, low-angle Kingston-Halloran detachment fault (KHDF) during Miocene extension (McMackin, 1987; Davis et al., 1993; Friedmann and Burbank, 1995).

Precambrian basement rocks surrounding the Winters Pass fault are classified as mylonitic L-S tectonics with well-developed foliation surfaces and NE-SW oriented stretching lineations. Previous work in the area by Hewett (1956), Burchfiel and Davis (1971) and McMackin (1987) have all recognized the presence of these mylonitic fabrics and have attributed their formation to a major low-angle fault system. Hewett (1956) recognized this fault as a low-angle thrust fault of Laramide age, due to intrusions of the Kingston Range monazite porphyry cutting other faults located within the “Winters Block” which he determined to have intruded during the Laramide orogeny. Burchfiel and Davis remapped the area and associated the low-angle basement mylonite zone as a Mesozoic thrust of Jurassic age, correlative to the Wheeler Pass thrust to the north and the Pachalka thrust to the south, but also noted the structurally higher

KHDF. McMakin (1987), embracing the concept of Cordilleran metamorphic core complexes after their recognition (Crittenden et al., 1980), remapped this area and reinterpreted the 'Winters Pass Thrust' of Burchfiel and Davis to be a low-angle detachment fault associated with Tertiary extension; thus, the mylonitic fabrics in the Precambrian basement associated with the Winters Pass fault have been alternatively interpreted to record Mesozoic contraction and Tertiary extension (Burchfiel and Davis, 1971; McMackin, 1987).

Compressive forces from subduction allowed for eastward transport of upper-plate rocks along west-dipping thrust faults, such as the Wheeler Pass and Pachalka thrusts and likely the Winters Pass thrust (Hamilton, 1969; Burchfiel and Davis, 1975; Dickinson, 1971; Burchfiel et al., 1992; DeCelles, 2004; Yonkee and Weil, 2015). It is thought that during this time, the Wheeler Pass thrust placed Neoproterozoic metamorphic rocks over Penn-Perm sedimentary rocks, while the Winters Pass thrust sheet places Paleoproterozoic metamorphic and Early Cambrian– Late Precambrian sedimentary rocks over Neoproterozoic-Middle Cambrian sedimentary rocks (Burchfiel and Davis, 1971; Giallorenzo et al., 2018). Combined heat, strain, fluids, grain size reduction, and production of micas within the deforming orthogneiss-protolith fault rock allowed for chemical, strain and fabric softening of the fault rocks and recrystallization of quartz, and the fracturing and chemical breakdown of feldspars to white micas and albite, which result in the formation of stretching lineations and pervasive foliations in the Precambrian basement in the area of Winters Pass.

The Winters Pass thrust is a decollement style thrust involving the Precambrian metamorphic bedrock and sedimentary rocks of the Pahrump Group and the passive margin sequence that are thrust over the Mesoproterozoic Crystal Springs Formation in its central exposures (Figures 3 and 4). In the NE exposures, where there is a lateral or oblique ramp, the

Winters Pass thrust places Neoproterozoic to Middle Cambrian sedimentary rocks over the Middle Cambrian Bonanza King Formation in an area characterized as a hanging-wall ramp juxtaposed over a footwall flat (Figures 3 and 4) (Burchfiel and Davis, 1971; Hewett, 1956; Mahon, 2014; McMakin, 1987). One mile west of the study area in the eastern Kingston Range, the Pahrump Group is exposed as a complete section including the Crystal Spring Formation, Horse Thief Springs Formation, Beck Spring Dolomite and the Kingston Peak Formation. Regionally, the Noonday Dolomite represents an Ediacaran cap carbonate overlap sequence that lies conformably on the Pahrump Group within the Pahrump Basin and unconformably on the Precambrian basement at the rift margins (Miller, 1987; Petterson et al., 2011).

In the Mesquite Mountains, Pahrump Group rocks are mainly exposed in the western and southern portion of the field area with the Kingston Peak Formation – the unit directly linked to the Precambrian rifting of Rodinia – only present in the northwesterly portions of the field area (Calzia et al., 2000; MacDonald et al., 2013; Mahon, 2014). With the exception of the thin exposures of the Kingstone Peak Formation in the NW portion of the Mesquite Mountains, the upper plate of the Winters Pass thrust contains the Paleoproterozoic basement and Neoproterozoic to early Cambrian sedimentary rocks that are placed over the Crystal Springs Formation of the Pahrump Group. Stratigraphic thinning and eventual pinchout of the Kingston Peak Formation and Pahrump Group towards the east suggest that the Mesquite Mountains lay in close proximity to the edge of the North American Craton during Precambrian rifting. South of the Mesquite Mountains in the Clark Mountains, the Pachalka and Powerline thrusts lacks any involvement of the Pahrump Group in its hanging-wall and footwall rocks, only including members of the Precambrian to -Late Cambrian transitional passive margin sedimentary wedge suggesting these two faults formed inboard of the paleo-cratonal boundary. These observations

allow for a more accurate representation of the Proterozoic rift architecture prior to crustal shortening during the Mesozoic. The unique style of Mesozoic deformation observed in the southern end of the Sevier orogenic belt likely was influenced by this architecture. The results from this study will help better define the tectonic history and paleogeography of the south Mojave, will help resolve the influence of Proterozoic rift architecture on the lower portion of the SFTB and will better define the timing of separate deformation events related to the formation of the Winters Pass thrust sheet.

METHODS

The mapping by Burchfiel and Davis, published in Calzia et al. (2000), provided a guide to produce a structural map of the field area to better display the distribution of mylonitic deformation within the Proterozoic basement and its relationship to the Winters Pass thrust as defined by Burchfiel and Davis (1971) and the KHDF (Davis et al., 1993; Calzia et al., 2000) Microstructural analysis of thin sections from oriented samples collected from the field were used to study deformation kinematics and deformation mechanisms in the Winters Pass mylonites. Ten samples were collected for $^{40}Ar/^{39}Ar$ geochronology to constrain the timing of deformation. Lastly, Electron backscatter diffraction (EBSD) is used to determine the crystallographic preferred orientation (CPO) of dynamically recrystallized quartz grains on eight samples, to provide more information about deformation temperatures and kinematics.

Structural Mapping

Structural mapping of the area around the Winters Pass thrust in the northern Mesquite Mountains was conducted to obtain information about the geometry of the thrust sheet, geometry of subsequent detachment faults, and both of their kinematics. The detailed geologic map published by Calzia et al. (2000) served as a basemap to guide the selection of locations for sampling fault rocks related to both the thrust and detachment faults throughout the field area and to build geologic cross sections (Figures 3 and 4). Lineation and foliation measurements from mylonitic orthogneiss and quartzite were plotted on the basemap and analyzed in stereographic projections to provide a visual and statistical representation of the overall orientations of the lineations, and any spatial variations in orientation (Figure 5). Observations collected in the field and in petrographic thin section, in conjunction with the mapped geology,

determined the locations where samples for geochronology and microstructural analysis were collected and analyzed. Structural mapping, microstructural study of thin sections, and EBSD data provide information about the kinematics of the system. Structures observed in the field and in thin-section allow the sense of shear to be determined to give the direction of motion for different parts of the thrust sheet. This information is used to characterize the thrust kinematics in the southern end of the SFTB and to compare to the proposed correlative thrust faults.

Petrography/Microstructures

Forty-one oriented samples were collected from the Mesquite and Clark mountains for petrographic and microstructural observations. Only samples that exhibited well-developed mylonitic fabrics and that were in close proximity to the mapped thrust or detachment fault were collected. Samples were oriented with marked foliation and lineation orientations measured by Brunton compass and GPS coordinates recorded. Oriented samples were cut in the standard kinematic reference frame in the XZ plane of finite strain, parallel to lineation and perpendicular to foliation, and billets were used to create thin sections with a thickness of 30μm for petrographic observation to determine the deformation kinematics, deformation mechanisms for dynamically recrystallized minerals like quartz and feldspar, and to identify the primary and secondary mineral phases that can be used for geochronological and thermochronological data sets. Grain size measurements were made on the petrographic microscope as well as the SEM. Grain-size distributions and dominant deformation mechanisms allows for an estimate of deformation temperatures to be determined.

When temperatures are high enough, stress on mineral grains allows the grains to undergo crystal-plastic deformation and dynamic recrystallization (Urai et al., 1986; Stünitz and Gerald, 1993; Stipp et al., 2002). Using microstructures, the mechanism of dynamic recrystallization of minerals like quartz and feldspar can be determined, from which temperature conditions can be estimated. Temperature has been shown to control the size of dynamically recrystallized grains based on the dominant dynamic recrystallization mechanism (Stipp et al., 2002). Bulge recrystallization (BLG) is the lowest temperature dynamic recrystallization mechanism where deformation is accomplished from local grain boundary migration producing the smallest sized grains (Urai et al., 1986; Stipp et al., 2002; Passchier and Trouw, 2005). Subgrain rotation recrystallization (SGR) is the next highest temperature recrystallization mechanism, where dislocation glide-and-climb accommodates the movement of dislocations (Urai et al., 1986; Stipp et al., 2002; Passchier and Trouw, 2005). In SGR, dislocations accumulate along nascent subgrain boundaries creating an increasingly higher angle of lattice misorientation to the original grain until a new grain is produced with a high-angle grain boundary. These grain boundaries are defined by misorientations angles >10º between grains (White and White, 1981; Neumann, 2000; Lagoeiro and Barbosa, 2010; Goddard et al., 2020). Grain boundary migration (GBM) is the highest temperature dynamic recrystallization mechanism where the movement of dislocations is accompanied by grain boundary migration via recrystallization-accommodated dislocation creep, producing the largest grain size (Urai et al., 1986; Stipp et al., 2002; Passchier and Trouw, 2005).

During ductile deformation of quartzo-feldspathic rocks, several microstructural textures that can be used to infer kinematics and transport direction (White et al., 1980; Gapais and White, 1982; Simpson and Schmid, 1983; Lister and Snoke, 1984; Passchier and Simpson, 1986;

Behrmann, 1987; Ten Grotenhius et al., 2003). Porphyroclasts of feldspar may contain recrystallized tails that form in the incremental extension quadrants of simple shear or are drawn out along shear (C) planes (Passchier and Simpson, 1986). S-C fabrics developed within the rock can produce shear bands and mica fish caused by localized zones of high shear strain that reflect the overall shear sense of the rock (Gapais and White, 1982; Lister and Snoke, 1984). At lower temperature deformation (<450º C) minerals like feldspar may deform brittlely and fracture, forming synthetic and antithetically rotated bookshelf structures that can be used to infer the overall shear sense (Stünitz and FitzGerald, 1993; Simpson and Schmid, 1983). The orientation of S-C fabrics, asymmetry of porphyroclasts, and rotated feldspar clasts can all be used in conjunction to determine the overall sense of shear of ductile fault rocks.

Electron Backscatter Diffraction

Deformation mechanisms of grains in deformed rocks can be studied through identification of microstructures in thin-section and by determining crystallographic preferred orientations (CPO). Using EBSD, the preferred orientation of a variety of lattice planes and axes can be determined for the areas mapped in thin section and for different grain types. The CPO from EBSD allows both the kinematics to be determined as well as the different slip systems responsible for the CPO (Figure 6.) (Stipp et al., 2002). Different mineral phases, and different slip systems within individual minerals, require different temperatures to undergo crystal-plastic deformation (Stünitz and Gerald, 1993). Identification of the mechanism of dynamic recrystallization, together with the CPO, assuming average geological strain rates, provides an estimate of the temperature of deformation. According to Schmid and Casey (1986), at moderate to low temperatures (< ~500ºC), dynamically recrystallizing quartz will primarily slip in the <a>

direction along three planes: (1) basal plane (0001), (2) the positive and negative rhomb planes (*r*) $\{10\bar{1}1\}$, (*z*) $\{01\bar{1}0\}$, and the (3) prism plane (*m*) $\{10\bar{1}0\}$. At higher temperatures (~500-600ºC) the mixed <a> slip associated with lower temperatures gives way to a regime dominated by prism <a> slip, and at even higher temperatures, exceeding 600ºC, prism <c> slip is activated (Hirth and Tullis, 1992; Barth et al., 2010; Zuo et al., 2021)

Electron backscatter diffraction (EBSD) data was collected for samples HK22CM-9, HK21MM-6, HK22MM-13, HK22MM-16, HK22MM-19, HK22MM-22, HK22MM-28, and HK22MM-29 (Figure 7 and 8). The data was collected on a JEOL JSM-7100F Field Emission Scanning Electron Microscope at the University of Nevada Reno under the following conditions: Working distance (25mm), accelerating voltage (25kV), and emission current (88.6μA). This data was processed using MTEX 5.9.0 running on MATLAB R2023a. Several datasets were produced which are discussed in detail below. The step size used for each sample is determined by the grain size within each sample, which was determined by petrographic observation. During data collection the samples were mapped in a grid. The spacing between each data collection point is determined by the spot size selected during initial setup of the scanning electron microscope (SEM). Deformation mechanisms and the appropriate spot size can be interpreted from petrography; smaller grains need to be mapped with a smaller spot size (≤5μm) while larger grains can be mapped with a larger spot size (≥5um).

The raw EBSD was imported into MTEX for post-processing using a function to calculate mineral phases from the electron backscatter diffraction patterns off of the crystal lattice. Primary and accessory phases are identified from petrography and are matched in the Aztec software using reference phase spectra. The MTEX script uses crystal symmetry to determine which mineral phase the diffraction patterns correlate to. All the samples in this

analysis come from quartzofeldspathic orthogneiss with the exception of HK22-MM28, which comes from a mylonitic quartzite. The mapped phases for all samples mainly include orthoclase, bytownite, quartz, and in some samples, chromite. The Aztec software used to collect the EBSD data does not differentiate between most cubic oxides, therefore any cubic oxide was indexed as chromite but is likely ilmenite. In this study a degree of misorientation in the crystal lattice of $\geq 10^{o}$ was used to define a grain boundary. Following data collection, a phase map of the mapped section can be produced in MATLAB with a color scheme to show different mineral phases. An inverse pole figure map of quartz grains is produced to show the orientations of quartz grain crystallographic directions relative to the Z strain direction. Unlike pole figures, which plot the orientations of the crystallographic directions against a fixed fabric reference frame, an inverse pole figure plots the crystallographic orientation against a fixed crystallographic reference frame. When processing in MTEX this crystallographic reference frame must be translated using the spatial reference frame for the SEM stage used to collect the data. The SEM used to collect this data makes the y-direction on the SEM stage parallel the foliation normal, or the Z strain direction. Crystallographic orientations are color coded with a key in MTEX to show the crystallographic direction that is parallel to the foliation normal. Grains that appear red in the map indicate that the c-axis of the lattice is oriented parallel to the foliation normal while cyan colored grains represent quartz grains that have their a-axis parallel to the foliation normal.

Quartz-quartz grain boundaries are then added to the IPF map using the same misorientation criteria used in the phase map of 10°. A misorientation to mean orientation map of quartz was produced to show the amount of internal crystal plastic deformation within the quartz grains of each sample. As grains undergo crystal plastic deformation in the shear zone, dislocations migrate into subgrain walls forming an increasing misorientation until a new grain

boundary is formed with the newly recrystallized grain being relatively free of dislocations. The misorientation to mean map and the kernel average misorientation (KAM) maps can be used to determine relative dislocation densities within the individual grains. Colors that appear warmer represent much higher degrees of accumulated dislocations while cooler colors represent grains that are relatively free of dislocation such as newly recrystallized grains. The misorientation to mean map does not show the spatial distribution of dislocations within the crystal lattice for each individual grain but rather shows average degrees of misorientations within grains and assigns a color to the entire grain. The kernel average misorientation (KAM) map is produced to show exactly where the dislocations specifically reside within each grain of quartz. Higher dislocation density within an individual grain is illustrated by the presence of lighter colored lines running throughout the grain. The shapes and orientations of these line segments that represent accumulated misorientation can indicate the dominant recrystallization mechanism. Straight line segments would indicate that climb-accommodated dislocation creep is the dominant mechanism as in SGR.

Pole figures (PF) and inverse pole figures (IPF) of the crystallographic preferred orientation (CPO) of quartz can be used to determine deformation temperatures within the rocks by determining the dominant slip system that is activated within the quartz crystal lattice (Figure 6). Pole figures plot the preferred orientation of the crystallographic axes in quartz against a fixed specimen reference frame, typically perpendicular to foliation and lineation. Inverse pole figures plot the preferred orientation of the quartz c-axis against a fixed crystallographic reference frame. The quartz crystal lattice is known to have four temperature dependent slip systems (Passchier and Trouw, 2005). Each of these slip systems produces a distinct signature on the c-axis pole figures and can be used as a fingerprint of the slip-system. A schematic from

Passchier and Trouw (2005) (Figure 6) shows how these different slip systems would manifest in both pole figure and inverse pole figure space. Obliquity relative to the foliation plane (inclination of the shear plane) within the contoured pole figure plots allow for kinematics to be determined for each sample.

$^{40}Ar/^{39}Ar$ Geochronology

The age of mylonitic deformation can be determined with the incremental heating $^{40}Ar/^{39}Ar$ method on muscovite. Mylonitic orthogneiss has dominant mineral phases of quartz, K-feldspar and plagioclase with secondary muscovite and albite. Due to the lack of primary muscovite in the protolith, secondary muscovite is likely synkinematic from the chemical breakdown of feldspar within the shear zone, creating the opportunity to directly date deformation. The growth of neocrystalline white micas occurs in most of the mylonites observed from the Winters Pass, Powerline Road and Pachalka thrust(s), producing thin mica seams along the foliation surfaces. The age of these white micas will record neocrystallization if mica growth occurred at a temperature below the closure temperature of the argon system for muscovite (around 425° C, Harrison et al., 2009, although grain size and cooling rate dependent) and alternatively will record cooling if the mica growth occurred at a temperature exceeding the closure temperature of the argon system (e.g., Dunlap, 1997).

Because the estimated deformation temperatures within the rocks are very close to the closure temperature it is important to correctly interpret whether the argon released from the muscovite grains records crystallization or cooling, or even a thermal overprint. Ideally, a background cooling curve produced with several thermochronometers would verify that the ages

are recording the age of crystallization and in this case, also deformation rather than either cooling or a thermal overprint. This method was attempted for this research; however, the rocks lack the necessary K-bearing and U-bearing minerals required to produce a cooling curve. A partial thermal history produced with K-feldspar using multi-diffusion-domain experiments could also be used, but petrographic analysis of the mylonites show that orthoclase has been sufficiently altered from fluid flow associated with deformation to not be suitable for $^{40}Ar/^{39}Ar$ multi-diffusion domain experiments. Imaging of the distribution of mineral phases relative to the rock microstructural fabric on the SEM, together with energy dispersive X-ray spectroscopy (EDS) analysis, was applied to the dated samples to both identify the mineralogy in fine-grained textural bands and to verify that muscovite grains within the rocks crystallized during deformation from the breakdown of primary feldspar in the orthogneiss.

Six samples from the Mesquite Mountains and three samples from the Clark Mountains were collected for geochronology. The Mesquite Mountain samples include HK21MM-3, HK21MM-4, HK22MM-10, HK22MM-12, HK22MM-29 and HK23MM-36. Samples from the Clark Mountains include HK22CM-4, HK22CM-5 and HK22CM-11 (Figure 5). Sample locations for geochronology in the Mesquite Mountains were selected in a variety of locations throughout the field area to best represent the ages for mylonitic deformation. Samples that exhibited the largest grain size (albeit micas in general were very fine grained, ~10 -50μm) and well-developed white micas were selected for age determinations.

Samples were processed in the mineral preparation and mineral separation labs in the Geoscience Department at University of Nevada Las Vegas (UNLV). Samples for muscovite geochronology were crushed and sieved to a range of grain diameters ranging from 350 μm to 63 μm. Different size fractions were observed under the microscope to determine the best size

fraction for muscovite geochronology. Muscovite within the mylonitic samples are polycrystalline crenulated aggregates that lack the perfect unidirectional cleavage common to micas, requiring heavy liquids to be used to separate muscovite as “paper shake” methods were unsuccessful. All samples were initially run through the Franz magnetic separator at 0.2A to reduce sample volume. The non-magnetic portion of the sample was placed into a separation funnel with full strength bromoform with a specific gravity (S.G.) of 2.85 g/cm^3 to separate heavy minerals such as zircon and metallic oxide minerals. A solution of bromoform and acetone with a S.G. of 2.7 g/cm^3 was created to separate muscovite from quartz and feldspar. This S.G. was determined by placing pure mineral specimens of muscovite (S.G. 2.77 - 2.88 g/cm^3), albite (S.G. 2.6 - 2.65 g/cm^3) and anorthite (S.G. 2.72–2.75 g/cm^3) in a beaker and progressively diluting the bromoform with acetone until a solution was produced that sank muscovite and floated anorthite, quartz and orthoclase. The remainder of the sample was then placed in a separation funnel with this solution of bromoform and acetone with a density of ca. 2.76 g/cm^3. The portion of the sample that sank was collected and washed three times in ultrasonic baths with acetone, ethanol, and water and then placed in a furnace at 67° C to dry. The dried muscovite separates were again run through a Franz magnetic separator at variable side tilts and amperage in order to remove contaminant grains. Samples were run through the Franz at 20° side tilt at 0.2A to remove any remaining magnetic grains. Samples were run through numerous times with successively increased amperage to further remove undesirable minerals. Upon final pass through in the Franz and great volume reduction, remaining materials were then handpicked under a binocular microscope to remove any impurities until a clean and uniform sample of muscovite was obtained for each sample. Final mineral separates for each sample are shown in (Figure 9).

Mineral separates were submitted to the Nevada Isotope Geochronology Laboratory (NIGL) at UNLV and processed following the methods described in Balbas et al. (2023). Each sample was irradiated for 6 hours at the Oregon State University TRIGA reactor, converting the stable ^{39}K to radiogenic ^{39}Ar. Samples were then loaded into a stainless-steel extraction line attached to a NGX noble gas mass-spectrometer where they were analyzed using the incremental heating method. The incremental heating method uses a double vacuum resistance furnace to slowly release the argon isotopes from different sites within the crystal lattice with increasing temperature. The gas released is scrubbed free of impurities and the 40, 39, 38 and 37 m/Z were measured using faraday cups attached to ATONA amplifiers while the 36 m/Z were measured using an ion counter. The Fish Canyon Tuff sanidine, with an age of 28.201 Ma (Kuiper et al., 2008) was used as the fluence monitor in calculating ages for the samples. For this study, samples underwent 19 – 31 heating steps starting at 550ºC until fusion at 1400ºC. Errors presented throughout represent internal uncertainties at the 2σ level.

RESULTS

Structure and Field

Mylonitic fabrics within the Precambrian basement are developed adjacent to the Winters Pass fault and contain a well-developed stretching lineation and pervasive foliation. Lineation measurements collected throughout the field area show a dominant NE-SW trending orientation which paired with the NW trend of fold axes in the hanging wall, suggest a NE transport direction that is markedly different from the transport directions observed elsewhere in the SFTB. The lineation direction stays consistent southward into the northern end of the Clark Mountains, near the Powerline Road thrust and is east trending in the shear zone adjacent to the Pachalka thrust further south in the western Clark Mountains. The mylonitic fabrics are concentrated near the fault delineating a shear zone varying in thickness from 5-100m. The map in Figure 3 shows the distribution of mylonitic fabrics throughout the basement in the field area of the Mesquite Mountains. Mylonitic development in the Precambrian basement is most pronounced in the west and southwest portions of the traces of the Winters Pass thrust in the Mesquite Mountains. Due to the high-strain nature of the mylonites, kinematics are commonly difficult to resolve in the field as the fabrics are dominantly symmetrical. However, limited exposures within the mylonitic basement, especially where relict augen are preserved, do exhibit asymmetric porphyroclasts and S-C fabrics that indicate a tectonic transport direction towards the NE, consistent with a contractional origin for the mylonites (Figure 10).

Precambrian basement in the hanging wall forms a relatively flat to low angle faulted contact with the Late Precambrian and Early Paleozoic sedimentary rocks of the footwall in both the Mesquite and northern Clark mountains. This faulted contact is usually associated with extensive mylonitic fabric around the periphery of the fault trace. Unfaulted contacts between the

basement and Precambrian sedimentary rocks are observed in the NW Mesquite Mountains where the Noonday Dolomite unconformably overlies the Paleoproterozoic basement, lacking any mylonitic fabrics. No apparent penetrative deformation related to shearing along the fault is observed within the sedimentary rocks of the thrust footwall, with the exception of few isolated outcrops of mylonitic quartzite along one ridge in the NW. In the NW Clark Mountains, strain has only accumulated within the Precambrian orthogneiss and in the immediately underlying quartzite. The shear zone associated with the Pachalka thrust on the western flank of the Clark Mountains deforms a Jurassic pluton in the hanging wall and the Wood Canyon Formation in the footwall.

The Pachalka thrust in the western Clark Mountains places Jurassic granite over Cambrian rocks including the Wood Canyon Formation, Zabriskie Quartzite and Carrara Formation. Clear kinematic indicators manifest in the hanging wall as asymmetric prophyroclasts within the mylonitized Jurassic granite and as overturned folds in the footwall within the Cambrian Zabriskie Quartzite and Carrara Formation demonstrate top-east kinematics. Moving along strike towards the north, the hanging wall of the Powerline Road thrust includes the older Precambrian basement which is thrust over the Johnnie Formation and Stirling Quartzite with stretching lineations trending NE. The Powerline Road thrust shares similarities to the hypothesized correlative Winters Pass and Pachalka thrusts. The Powerline Road thrust, like the Winters Pass thrust, involves Precambrian basement in the hanging wall and the Precambrian sedimentary strata in the footwall with NE trending lineations. The trace of the Powerline Road thrust lies along strike with the Pachalka thrust.

In the Mesquite Mountains, the hanging-wall geology consists of Precambrian orthogneiss and Neoproterozoic to Cambrian sedimentary rocks that are increasingly mylonitic

near the western fault traces. This mylonitic fabric is characterized by generally shallowly plunging, NE-SW trending stretching lineations with limited kinematic indicators and two dominant foliation directions measuring 170, 8W and 051, 26SE (Figure 5). The footwall geology consists of Mesoproterozoic to Early Cambrian sedimentary rocks that are relatively undeformed in the western portions of the field area. Deformation in the Neoproterozoic and Early Cambrian section is more evident in the NE portion of the field area just north of Winters Pass where a large NE-vergent, NW-plunging anticline with a fold axis of 319, 48 is developed in the hanging-wall, adjacent to the hanging-wall ramp of the Winters Pass thrust. Within this large fold, parasitic folds within the Zabriskie Quartzite mirror the NW trend of the larger fold with an average trend of 336. The overall vergence of these folds matches the trend of lineation measurements suggesting the two are related to the same deformation event. East of Winters Pass, in the footwall of the thrust, is a heavily folded section of the Cambrian Bonanza King Formation with fold axes trending N-S (Figures 3 and 4). West of these folds, the hanging-wall geology consists of thin slabs of mylonitic Precambrian orthogneiss.

In the center of the Mesquite Mountains study area lies remnants (klippe) of a once continuous upper plate of the KHDF - a clear detachment fault that juxtaposes Cambrian strata against strongly mylonitized Precambrian basement. Higher angle normal faults that sole into (or are cut by) the detachment are inferred, leading to repeated sections of the Bonanza King Formation. The detachment fault traces in the center of the field area are consistent with a synclinal-shaped fault plane. Foliation measurements taken in the basement along the perimeter of this fault trace are oppositely dipping on both sides of the synclinal structure towards the faulted sedimentary rocks. Foliation measurements average 098, 3 on the NW side of the detachment and average 187, 2 on the SE side of the detachment. The attitudes of the foliation

surface are near horizontal around the detachment compared to the ~30-15º and sometimes greater dips elsewhere in the mylonitic basement, with foliation surfaces striking nearly parallel to the fault trace. Along the western margin of the field area lies faulted contacts of basement and sedimentary rock that exhibit brittle deformation in the footwall marked by zones of cataclasite likely associated with Miocene detachment faulting.

Petrography and Microstructures

Forty-one thin sections were prepared from samples collected from the mylonitic basement near both the thrust and detachment faults as mapped by Burchfiel and Davis. All of these samples contain well-developed, relatively flat-lying foliations and NE-SW trending stretching lineations. Many of the samples exhibit high-strain magnitudes, a significant amount of grain-size reduction, and dominantly symmetric fabrics making kinematics in both hand sample and thin section difficult to resolve. Several coarser grained mylonitic samples exhibit bookshelf structures in brittlely deformed feldspar, sigma-type and delta-type porphyroclasts of quartz and feldspar and S-C fabrics developed within synkinematic white mica that show a top-NE sense of shear, consistent with Mesozoic thrusting deformation (Figure 11).

In all samples, crystal plastic deformation is only apparent in quartz, and feldspars deformed brittlely. In the coarser grained bands quartz grains are polygonal in shape, with finer grained bands containing more irregular to rounded shaped grains. Samples collected from the Mesquite Mountains and from the northern Clark Mountains show dynamic recrystallization of quartz that is dominated by both SGR and BLG, suggesting deformation temperatures around 350-450º C (Stipp et al., 2002); should fluids have been present to cause hydrolytic weakening,

these temperature estimates would be lower. Recrystallized quartz grains can be seen as strung-out quartz ribbons with core and mantle structures exhibiting polygonal recrystallized grains with finer grained domains supporting bulge nucleation around grain boundaries. Some of the recrystallized grains exhibit sweeping undulatory extinction. Grain sizes for recrystallized quartz have a bimodal range from 1-25 µm and 25-60 µm. The grainsize for naturally deforming rocks is largely controlled by the deformation mechanism driving recrystallization (Stipp et al., 2002, 2010). The range of grain sizes for recrystallized quartz in the fine-grained portions is around 1-10 µm and is the estimated grain size for grains undergoing BLG recrystallization (Stipp et al., 2010). Coarser grained domains of recrystallized quartz forming ribbons of polygonal grains with grain sizes ranging from 30-50 µm correlate to recrystallization by subgrain rotation (Stipp et al., 2010). The range of grain size indicates BLG-SGR conditions, suggesting a temperature range of 375-425° C (Hirth and Tullis, 1992; Stipp et al., 2002, 2010). These temperature estimates assume a normal strain rate and do not take into account effects of hydrolytic weakening as described by Law (2014), which may lower the activation temperature of different slip-systems.

Most samples exhibit fine-grained polycrystalline white mica seams along foliation surfaces and in strain shadows adjacent to feldspar which are interpreted have grown during deformation by the breakdown of feldspars. Reaction rims around feldspars and corroded grain margins can be seen in most thin-sections (Figure 12), suggesting that fluid-flow associated with faulting facilitated the breakdown of K-feldspar and plagioclase into muscovite, albite and quartz. The quartz precipitating from the breakdown of feldspars is recrystallized in strain shadow and dilatant sites in feldspar pull-aparts, and perhaps is the genesis for the finest grained component of quartz in the matrix, implying that the breakdown of feldspar occurred during

shearing rather than occurring during a later fluid-flow or alteration event. Evidence of fluid-flow through the fault rocks can also be seen by presence of oxide mineralization within the fault rocks. Energy dispersive X-ray spectroscopy (EDS) analysis applied to several samples, shows that primary orthoclase and primary albite are being reworked into muscovite and quartz following the reactions from Wibberley (1999) as well as secondary albite found in fine grained domains in the matrix as well as in dilatant sites (Figures 13 and 14). The reactions defined by Wibberley are as follows:

1) $3NaAlSi_3O_8 + K^+ + 2H^+ \rightarrow KAl_3Si_3O_{10}(OH)_2 + 6SiO_2 + 3Na^+$

   albite → muscovite + quartz + sodium

2) $3KAlSi_3O_8 + 2H^+ \rightarrow KAl_3Si_6O_{10}(OH)_2 + 6SiO_2 + 2K^+$

   orthoclase → muscovite + quartz + potassium

The first is a direct single reaction from albite to produce muscovite and quartz, while the second is a direct single reaction from orthoclase to produce muscovite and quartz. The isolated patches of both orthoclase and plagioclase throughout fine-grained domains suggest that fluid-assisted diffusion creep played a critical role in chemically altering and breaking down these feldspars and producing secondary phases during deformation. Syndeformational fluid flowing through the fault rocks likely lowered the activation temperatures of deformation mechanisms for the recrystallized quartz in a process called hydrolytic weakening (Law, 2014), placing deformation temperatures closer to 375-400°C – around the boundary transition between BLG and SGR (Stipp et al., 2002).

Electron Backscatter Diffraction

Raw EBSD data were imported to MTEX to reconstruct grains boundaries and interpret crystallographic data. For this study, the MTEX script uses the indexed minerals from the AZTEC software determined during data collection. Grain boundaries for individual mineral grains are defined as a misorientation of more than 10° (White and White, 1981; Neumann, 2000; Lagoeiro and Barbosa, 2010; Goddard et al., 2020). MTEX uses the phase ID from the Aztec file combined with the newly defined grain boundaries to construct phase maps of the mapped areas. Using this framework of grains in MTEX allows for crystallographic orientations of the individual grains to be determined which can then be plotted to show the distribution of misorientations within individual grains via misorientation to mean maps (Figure 15).

The eight samples analyzed for this study all exhibit an extremely fine-grained quartz domain. Data was collected for each sample at two spot sizes, 1 and 4µm or 1 and 2 µm. For all samples analyzed, maps of misorientation within individual quartz grains were measured, defining misorientations of 2-10º. From the CPO patterns of quartz grains, plotted as pole figures (PF) and inverse pole figures (IPF), the active slip-systems, shear sense, and deformation temperatures were obtained. The PFs and IPFs can be compared to each other to verify the accuracy of the results. If the slip systems inferences between the two match, it can be concluded that the data has been processed correctly.

To interpret kinematics and dominant slip systems from EBSD data collected from quartz, the orientation of the crystallographic vorticity axis (CVA) must be known such that the data can be projected in the plane perpendicular to the CVA. Additionally, in rocks with either incomplete dynamic recrystallization and or strain overprints on an earlier strain fabric, newer dynamically recrystallized grains must be separated from older relict grains for analysis. This reference frame is determined by the vorticity axis derived from the internal lattice distortion

within grains. The vorticity axis is a rotational axis about which the internal strain is accommodated during deformation (Michels et al., 2015; Piette-Lauzière et al., 2020). The orientation of the vorticity axis changes depending on the flow geometry during deformation i.e., simple shear, pure shear, transpression, or transtension. The classic assumption is that the 'kinematic plane' is seen looking perpendicular to the lineation direction parallel to the foliation plane, down the vorticity axis. The eight samples cut for EBSD analysis were cut in this orientation.

Almost all research using CPO data to interpret slip systems within dynamically recrystallized grains and their kinematics observes the data within the specimen reference frame; a perspective that shows the crystallographic orientation on top of a fixed reference frame defined by the fabric in the rock. Recent research has considered looking at the data along the vorticity reference frame (Michel et al., 2015; Kruckenberg et al., 2019; Miranda et al., 2023), in recognition of alternate strain geometries such as transpression and transtension. The crystallographic vorticity axis (CVA) of each sample is calculated from each of the indexed grains in the MTEX software. CVAs can be calculated for the bulk mineral constituents of the sample or calculated for individual mineral phases. For this study, quartz grains were selected for CVA analysis as they are the only grains to have undergone crystal-plastic strain. The CVA is plotted on a stereogram and depending on where the CVA plots, the type of flow geometry can be interpreted as follows: 1) Pure shear dominated monoclinic transpression - the vorticity axis will be oriented along apparent west and eastern edges of the pole figure along the foliation plane. 2) Simple shear and monoclinic transpression – the vorticity axis will be in the center of the pole figure. 3) Transtension - the vorticity axis is at the tops and bottoms of the pole figure indicating the vorticity axis is oriented perpendicular to the foliation plane. 4) Triclinic

transpression the vorticity axis sits at an oblique angle to either foliation parallel or foliation normal. Figure 16 shows the predicted CVA orientations for different flow geometries. Initial processing of the EBSD data for the seven Mesquite Mountain samples suggested flow geometries that correspond to transtensional strain (Figure 17). When the EBSD data was rotated into the vorticity axis reference frame, the rotated PF and IPFs were not compatible with each other and suggested slip-systems that were very inconsistent with petrographic results indicating that the data was not being processed correctly.

Due to the limited number of grains that preserved internal lattice distortion, likely due to complete dynamic recrystallization into new grains, a grain orientation threshold for which grains are selected for CPO analysis was applied. Misorientations of 2-10° in a crystal lattice designates the formation of a new subgrain boundary (White and White, 1981; Neumann, 2000; Lagoeiro and Barbosa, 2010; Goddard et al., 2020). However small misorientations of less than 2° can be detected with EBSD. When looking at the misorientation to mean maps (Figure 15), it can be seen that for all samples only a handful of grains have accumulated internal strain, likely making the results from a bulk analysis of all grains unrepresentative. Because of this, a grain orientation threshold ranging from 0.5-3° was applied to all the samples in order to only select dynamically recrystallized grains. The selected grains can be checked in MTEX by plotting the selected grains on the phase map, outlined in red, and comparing to the misorientation to mean maps (Figure 15) to verify that only grains with accumulated strain are being selected for analysis. The CVA plots produced with the applied grain orientation threshold (Figure 18) generated results that indicate monoclinic and, in some cases, triclinic transpression. These results match the interpretations made from petrographic and field analysis as well. The CVA plots produced were rotated, similar to how data would be rotated on a stereonet, to show the

data in the vorticity reference frame. The pole figure and inverse pole figures produced with this grain orientation threshold showed low temperature slip systems associated with mixed <a> slip including basal <a> rhomb <a> and prism <a> slip, slip indicating deformation temperatures less than ~425ºC, consistent with petrographic observations (Figures 19 and 20). Each sample's pole figure and correlative inverse pole figure showed consistent results for active slip-systems. Lineation measurements for each sample show that the inclination of the shear plane in each of the pole figures is recording top-NE sense of shear.

When using the bulk CVA plots produced using a grain orientation spread of zero (Figure 17), the results suggest that rotating the data to be looking nearly perpendicular to the foliation places the samples in the vorticity reference frame. These initial results suggest that the flow geometry of the rocks indicates transtensional motion, supporting the idea proposed by McMakin (1987) that deformation is related to extension. However, the corresponding pole figures produced from this rotation do not support the observations made petrographically nor do they match the inverse pole figure. It is only when the grain orientation spread is applied to the samples, selecting only the recrystallized grains for CVA analysis, that the corresponding pole figures match the interpretations made from petrographic observations. The CVA plots suggest monoclinic and, in some cases, triclinic transpression, which, along with the shear sense from the CPO figures, match the interpretations made by Burchfiel and Davis (1971) that deformation is related to thrusting (Figure 18, and 19). CVA analysis may be more sensitive to minor strain overprints than CPOs. It is possible that the CVAs produced when considering very minor lattice distortions record a low intensity strain overprint related to Miocene detachment faulting, whereas the CVA analysis using a higher GOS value records the older, thrust-sense kinematics.

$^{40}Ar/^{39}Ar$ Geochronology

Nine muscovite samples were analyzed by furnace step heating for $^{40}Ar/^{39}Ar$ geochronology. Petrographic analysis of the Winters Pass mylonites suggest lower greenschist facies metamorphic conditions during deformation with deformation microstructures supporting temperatures ≤425ºC, below the assumed closure temperature of 425ºC for muscovite (Harrison et al., 2009). Due to the fine-grained nature of individual muscovite grains creating the polycrystalline aggregates, it is likely that closure temperatures are less than 425ºC. Using the diffusion parameters described by Harrison (2009), closure temperatures for the respective average grainsize (~30µm) have been calculated to be ~398º - 408ºC, assuming a cooling rate of 10-20 degrees per million years. Of the nine samples analyzed in this study, only two produced concordant plateaus or isochrons: samples HK22-MM10, and HK22-MM12. All samples show a similar degassing pattern, with the initial gas (~0-25%) defining an age gradient from ~40 Ma to ~70 Ma for the Mesquite Mountain samples and to ~80 Ma for the Clark Mountain samples (Figures 21 and 22). All age spectra for the samples, with the exception of HK22-CM11, flatten out for the next ~50% of argon gas released. Ages from the Mesquite Mountains all generally fall between 65-74 Ma with the two Clark Mountain samples flattening closer to 80 Ma (Figures 21 and 22). Overall, the sample ages show age gradients with ages increasing with temperature, and the results suggest a Late Cretaceous age for the muscovite.

Samples HK21-MM4, HK21-MM5 and HK22-MM10 share nearly identical results with the lower temperature heating steps climbing from ~41 to 70 Ma constituting ~22% of the cumulative argon gas released. The higher temperature steps release ~63% of the total argon and present a flat age plateau ~73 Ma. The last 15% of argon is released during the highest temperature steps, producing ages that gradually climb upwards. Argon release from the Clark

Mountains samples all show a progressively increasing age degassing pattern with flattish segments which were used to calculate weighted mean preferred ages. HK22-CM4 and HK22-CM5 exhibit a fairly stable degassing pattern for the first 50% of argon gas released and both progressively increase in age for the remaining 50%. Argon release for HK21-CM11 exhibits a steady stair stepping pattern throughout the entire experiment. However, the total fusion age and weighted mean age is nearly identical to that of HK22-CM5 and similar to HK22-CM4.

The experiments carried out on muscovite from the Mesquite Mountains samples, while only producing two concordant results, show fairly consistent degassing patterns with preferred ages being consistent between samples. The mean age produced by all samples from the Mesquite Mountains, excluding HK23-MM36, is Late Cretaceous at 72.54 Ma. Clark Mountain muscovite produce slightly older ages with a mean of 86.35 Ma, also Late Cretaceous. Although only some of the experiments produced concordant age spectra, the calculated total fusion, plateau and inverse isochron ages suggest a Late Cretaceous age of deformation for these mylonitic rocks. Discordance within many of the samples can be attributed to either protracted muscovite growth or to impurities in the mineral separates. Polycrystalline growth of muscovite and precipitation of albite due to mobility of K^+ and Na^+ during fluid-assisted diffusion creep paired with the extremely fine grain size of these muscovite grains likely resulted in impurities of albite and orthoclase in the muscovite separates; these impurities may have influenced the degassing behavior, prohibiting concordant results. This can be seen by observing the K/Ca ratios of most samples (Figure 21). The variability of K/Ca in these experiments likely is due to these feldspar contaminations.

DISCUSSION

Precambrian Rift Geometry

The Mesquite Mountains and adjacent Kingston Peak Range region expose variations in Paleozoic to Precambrian metasedimentary rocks that suggests a geographic location near the eastern boundary of the Precambrian passive margin. The basement in the eastern part of the Mesquite Range is unconformably overlain by the Noonday Dolomite whereas the Kingston Range locally exposes ca. 2.5 km of the Kingston Peak Formation, a unit that regionally has been interpreted to record syn-rifting deposition (Prave, 1999; MacDonald et al., 2013). The NW Mesquite Mountains includes thin exposures of the Kingston Peak Formation and lacks other members of the Pahrump Group suggesting that this area marks the paleo rift boundary separating the basin by a basement promontory (Wernickie et al., 1988; Lobianco, 2022). This promontory of basement is interpreted to have had a major influence on the geometry and perhaps on the transport direction of the Clark Mountain thrust complex. The Mesquite Mountains contains a sedimentary sequence of conglomerate, sandstone, and carbonate rocks intruded by diabase in the footwall of the Winters Pass thrust that has been interpreted alternatively as the Stirling Quartzite, Johnnie Formation and Noonday Formation, (Burchfiel and Davis, 1971) and as the Crystal Springs Formation (McMakin, 1987). Detrital zircon U-Pb dating reported in Lobianco (2022) supports the interpretation of McMakin (1987) that these rocks are part of the Crystal Springs Formation. Detrital zircon age populations lack the Grenville grains (1.2-1.0 Ga) that are common in the Johnnie Formation and Stirling Quartzite and include Mesoproterozoic (ca. 1.4 Ga) and Paleoproterozoic (1.8-1.7 Ga) grains common in the Crystal Springs Formation (Mahon et al., 2014). In the eastern Mesquite Mountains and western Clark Mountains, Noonday Formation lies unconformably over the gneissic basement

which is overlain by the dominantly siliciclastic Johnnie Formation through Zabriskie Quartzite and does not include any members of the Pahrump Group. In the southern Mesquite Mountains, large exposures of the Crystal Springs Formation are seen in fault contact below the Precambrian basement. The presence of this large accumulation of the Crystal Springs Formation suggests an isolated basin formed by Precambrian tectonics to accommodate a separate depositional basin of the Crystal Springs as it is absent from the rest of the field area.

Age Constraints on Mylonitic Deformation

Previous work in the Mesquite Mountains has suggested that the low-angle mylonitic fabrics in the basement rocks are likely to be either Jurassic, Cretaceous or Miocene in age (Hewitt, 1956; Burchfiel and Davis, 1971; McMakin, 1987). The results of $^{40}Ar/^{39}Ar$ age determination experiments on synkinematic muscovite within the mylonitic basement rocks yield a preferred age (weighted mean of flattish segment of age spectra) of ~73 Ma, which suggests that motion on the Winters Pass fault is of Laramide age. Most prior research has suggested that the Winters Pass thrust correlates to both the Pachalka and Wheeler Pass thrusts and formed in the Jurassic during early stages of the Sevier orogeny (Burchfiel and Davis 1971; Giallorenzo et al., 2018; Wernicke and Snow 2000). Walker et al. (1995), through dating of two Late Jurassic plutons, suggested that the Pachalka thrust was of Late Jurassic age, and by correlation, that the Winters Pass thrust was also active at this time. The new ages presented herein overturn this prior interpretation and demonstrate that this fault was active during the Laramide orogeny.

It could be argued that the Winters Pass thrust mylonites underwent two contractional deformation events, one in the Jurassic and the other in the Late Cretaceous. If the mylonitic

rocks experienced two contractional deformation events, only the most recent would be recorded by $^{40}Ar/^{39}Ar$ muscovite age determinations. Reactivation of the shear zone during Cretaceous time could potentially release the radiogenic argon trapped within the muscovite if reheated above the closure temperature of ~400ºC, or if fluid-rock interaction reset the age to the most recent deformation. Quartz will begin to recrystallize at around 300º C (Stipp et al., 2002, 2010). If the shear zones were reactivated at sufficiently high enough temperatures (i.e. >400º C) in the Late Cretaceous to thermally reset the synkinematic muscovite, temperatures would also be sufficient to recrystallize quartz within the mylonitic rocks; thus, the Late Cretaceous ages should be associated with the dynamic recrystallization and CPO observed in quartz. This suggests that the thrust was, at the very least, active during the Laramide in the Late Cretaceous. If an overprint occurred, the folding of sedimentary rocks may be attributed to the initial deformation of the Sevier and possibly explains changes in fold axis orientations during a second folding event in the Late Cretaceous. Rather than two deformation events, we interpret the difference in fold axis orientations to be due to the development of a lateral ramp in the thrust, creating the northeastward step in the southern exposure of the Winters Pass thrust. Due to the extremely fine grain size of the muscovite, the most parsimonious interpretation is that the Late Cretaceous muscovite ages record thrusting during the Sevier orogeny.

The Mojave Desert is known to have experienced widespread extension around 75-65 Ma during the Laramide orogeny, interpreted as resulting from delamination of mantle lithosphere prior to slab flattening (Barba, 2020; Wells et al., 2005; Wells and Hoisch, 2008) or alternatively due to the passage of theCSR and return flow of the Pelona–Orocopia–Rand schists (Saleeby, 2003; Chapman et al., 2010). In the eastern Mojave Desert, examples include the western Old Woman Mountains shear zone (Carl et al., 1991), the Iron Mountains shear zone (Wells and

Hoisch, 2008), the Pinto shear zone in the New York Mountains (Wells et al., 2005), and the extensional shear zones in the Granite Mountains and northern Bristol Mountains (Hess and Wells, 2016; Hess, 2017). Although the new ages for the Winters Pass mylonites –interpreted as contractional– overlap in timing with the recognized ages for Late Cretaceous extension in the Mojave, we see no evidence or reasonable interpretation to suggest that the Late Cretaceous ages for these mylonites could be linked to top-west extensional shear. Could the top-NE kinematics be related to extension? Considering what is known about the geometry and kinematics of the east-vergent southern SFTB, and the presence of east-vergent contractional folds associated with the Winters Pass thrust, the dominant top-southwest kinematics on Late Cretaceous extensional structures in the nearest known extensional structures including the Pinto shear zone in the New York Mountains (Wells et al., 2005) and extensional shear zones in the Granite (after restoration) and Bristol Mountains (Hess and Wells, 2016; Hess, 2017), it is unlikely that the top-NE kinematics record extension. Thus, we are left with the observation that Laramide contraction in the northern Clark Mountain thrust complex was coeval with Laramide extension in other regions of the Mojave Desert located to the south and southwest.

Alternatively, could extensional shear have thermally reset the muscovite in the Mesquite Mountains with little to no recrystallization of quartz? The Mesquite Mountains and neighboring Kingston Range have clear evidence for extensional tectonics, expressed mainly as the top-west KHDF (Davis et al., 1993, Friedmann and Burbank, 1995). This detachment fault is interpreted as Miocene, not Laramide, in age as it locally involves Tertiary rocks (Davis et al., 1993; Friedmann and Burbank, 1995; McMackin 1987). This argument is more difficult to support when looking at the Clark Mountains. The mylonites associated with the Pachalka and Powerline Road thrusts are notably clearly of contractional origin as they are associated with development

of large-scale east- and northeast-vergent overturned folds. The ages for the muscovite from the Powerline thrust, although slightly older at ~81 Ma, likely also record early thrusting associated with this protracted episode of Laramide shortening. The ages for the Powerline Road and Pachalka thrust in the Clark Mountains and the exposures of mylonitic basement rock interpreted to represent the Winters Pass thrust in the Mesquite Mountains are sufficiently distinct that they are interpreted to represent two events, although a record of protracted shortening is also permissive. The stair-stepping pattern of argon ages seen throughout almost all samples may be recording the duration of active shearing during this event. Kirschner (1996), in a $^{40}Ar/^{39}Ar$ study of a low-temperature carbonate mylonite from the Alps, suggested that stairstep age spectra in synkinematic muscovites may record the duration of shearing. Accordingly, it is permissive that strain associated with Winters Pass thrust occurred from ~74-66 Ma, and strain associated with the Powerline Road and Pachalka thrusts occurred from ~86-73 Ma.

The thrust faults along the western margin of the Clark Mountain thrust complex (CMTC), including the Winters Pass thrust and the Powerline thrust, are interpreted to be out-of-sequence thrusts, related to backward-breaking imbrication (Figure 23). The easternmost thrust, the Keaney-Mollusk Mine thrust, is constrained to have moved between 100 Ma and 93 Ma (Fleck et al., 1994; Walker et al., 1995), which correlates to ages further north from the Contact, Wilson Cliffs, and Red Springs thrusts (Fleck and Carr, 1990; Giallorenzo et al., 2018). The sequence of thrusting evident from this study is that following slip on the Keaney-Mullusk Mine thrust, there was slip on the Powerline Road/Pachalka and finally, the Winters Pass thrusts. This would place the Winters Pass thrust as the structural highest, and youngest thrust in the complex, followed by the Pachalka/Powerline Road, Mesquite, and Keaney-Mullusk Mine thrust.

Miocene Extensional Overprint

The Miocene detachment fault system – the KHDF – bounds the western side of the Mesquite Mountains and produced the Shadow Valley basin as a supradetachment basin (Davis et al., 1993; Friedmann and Burbank, 1995). Several isolated detachment klippe of Cambrian rocks, dominantly Bonanza King Dolomite, are faulted over Precambrian basement throughout the Mesquite Mountains, in some cases containing brittle cataclasite along the fault surface. At one locality along its western (down-dip) trace, the mylonitic fabrics in the basement become progressively more deformed and grain size reduced as one approaches the detachment, suggesting that at least locally, ductile deformation accompanied detachment faulting. Although no detailed work was done on the KHDF, the klippe in the center of the field area are interpreted to have originated from the upright section seen in the northeasternmost exposures of the Mesquite Mountains (Figure 3).

McMackin (1987) interpreted the mylonitic fabrics in the basement rocks of the Mesquite Mountains to have formed from deformation associated with the KHDF whereas Burchfiel and Davis (1971) interpreted them as thrust-sense mylonites. Our muscovite age determinations and kinematic analysis of the mylonites supports the interpretation of Burchfiel and Davis (1971), but with the important modification that the mylonites are of late Cretaceous age and formed in a backward-breaking thrust sequence. However, the doming of the basement as driven by isostatic uplift of the lower plate during Miocene detachment faulting to form east-dipping outcrops of mylonite is supported by our observations. SW-directed transport and thinning of the hanging wall containing thick Cambrian carbonate and siliciclastic sequences removed a large lithostatic load on the lower plate, promoting isostatic uplift in the footwall of the KHDF creating flexure in the basement (Wernicke and Axen, 1988; Buck, 1988).

In the western portion of the Mesquite Mountains the thrust is located at a deeper structural level than what is seen toward the east along Winters Pass Road. Mylonitic fabrics likely were translated from their deeper structural level of formation to their current positions along the thrust, explaining the lack of mylonitic fabrics in the footwall. This deeper portion of the thrust hanging wall likely was under higher temperature and depth conditions allowing for greenschist facies metamorphism and low-temperature crystal plasticity and dynamic recrystallization of quartz, as well as dissolution creep of feldspar and production of secondary muscovite, albite and quartz, responsible for the mylonitic fabric developed within the basement. After Miocene exhumation due to detachment slip and isostatic rebound, flexure and subsequent rotation, the structurally lower west-dipping Winters Pass thrust was brought to the surface, exposing the mylonitic fabrics and locally back-rotating the thrust to an east-dipping orientation in the western Mesquite Mountains. The thrust mylonite contains fabric reflecting NE transport of the upper plate during Laramide time. Overturned NE-vergent folds within the upper and lower plates (near Winters Pass Road) of the Winters Pass thrust complex help to validate the overall NE-E vergent motion of the thrust sheet evident from the mylonites.

The KHDF has been constrained to Miocene time (Davis et al., 1993, Fridedmann and Burbank, 1995). The field and quantitative data collected for this project does not support the metamorphic core complex model for the mylonitic fabrics in the Mesquite Mountains. The activation temperature for the crystal-plastic deformation of quartz is constrained to ~300° C (Stipp et al., 2002). Petrographic observation and EBSD data on microstructural fabrics within the mylonitic rocks constrain deformation temperatures to ~350^{-}425° C. If these deformation fabrics were related to Miocene extension, deformation temperatures would be sufficiently hot to cause at least partial argon loss within the muscovite that is seen along the foliation planes.

EBSD data collected on the mylonitic rocks, while recording a NE-transport direction, may also record a Miocene extensional overprint related to the KHDF (see discussion below). Under the lower temperature conditions associated with the KHDF detachment, quartz grains may have begun to accumulate small amounts of strain to reflect this event.

Crystallographic vorticity analysis suggests that the mylonites locally may record an overprint related to Miocene detachment faulting. CVA plots that are limited to grains that have accumulated misorientations greater than 0.5º record NE transport under simple shear. In contrast, CVA plots for grains that have accumulated misorientations of less than 0.5º record a transtensional signature (Figures 17 and 18). The transtensional signature for "bulk" quartz is interpreted to represent small-scale lattice distortion of quartz during the development of the KHDF. Quartz begins to deform plastically at temperatures around ~300º C, and possibly lower with effects of hydrolytic weakening (Law, 2014; Stipp et al., 2002). We suggest that during the initial slip associated with the KHDF system, the shear zone was likely at shallow depths with temperatures no greater than 275-300ºC. Reactivation of the Cretaceous shear zone during Miocene extensional shear may have accumulated misorientations within quartz on the order of fractions to a single degree. Sufficient temperatures were not reached to sufficiently cause crystal-plastic deformation of quartz to overprint the CPO, but CVA analysis using new analytical techniques with EBSD (Michels, 2015) can record small-scale lattice bending to produce a new CVA associated with this event.

Tectonic Driver for Cretaceous Contraction in the Mojave

Deformation associated with the Sevier-Laramide orogeny experienced a transition as the Farallon slab progressively flattened, driving deformation eastward during the Laramide orogeny, creating the commonly recognized Laramide block uplifts further into the continental interior in present day Colorado and Wyoming (Axen et al., 2018; Saleeby, 2003; Yonkee and Weil, 2015). The Keaney-Mollusk Mine thrust, the easternmost thrust in the CMTC, has long been considered to be the youngest thrust in the southernmost Sevier belt in the Mojave. However, this study shows that (1) the western thrusts are younger and formed in Laramide time, and (2) that they formed in a backward-breaking sequence. Thus, this new data demonstrates that the Clark Mountain thrust complex and possibly other unrecognized areas in the Mojave, experienced continued contractional deformation into the Late Cretaceous, during the transition from normal subduction to flat-slab subduction marking the Sevier-Laramide transition.

The subduction angle of the Farallon plate is thought to decrease between 90 and 80 Ma. (Liu and Currie, 2016; Axen et al., 2018). The cause of this decrease in subduction angle is attributed to several variables, most notably the subduction of the more buoyant CSR, an increase in westward drift of the North American plate in a fixed mantle reference frame, and an increase in plate convergence rates between the North American and the Farallon plates. The shutdown of the magmatic arc related to the flattening slab is thought to be due to either removal or restriction of the convecting asthenospheric wedge. The shallowing of the subduction angle after 80 Ma is coeval with regional extension in the Mojave around 65-75 Ma (Wells and Hoisch, 2008). Hinterland extension following the shut-down of the arc, is thought bring the wedge into sub-critical taper, which promotes internal shortening of the orogenic wedge in order to bring the wedge back to critical taper (Dahlen, 1990; DeCelles and Mitra, 1995; DeCelles, 2009; Graveleau et al., 2012). Plate reconstructions and inverse mantle flow modeling (Liu et al.,

2016) suggest that around the same time, the CSR was traveling NE under this portion of the eastern Mojave. The NE-directed shortening direction on the Winters Pass and Powerline thrusts likely reflects the direct influence of the subducted, positively buoyant CSR because the direction of Farallon-North America plate convergence during the Late Cretaceous, which controls the direction of subterranean passage of the CSR (Saleeby, 2003), nearly mirrors the lineation measurements seen in the mylonitic fabrics. The shallowing subduction angle follows the removal of the eclogitic root beneath the volcanic arc which creates an interaction with the underthrusting retroarc continental lithosphere. This would produce a situation of "overcrowding" between the two plates (DeCelles, 2009). The heterogenous nature of the CSR, which had significant differences in thickness of buoyant basaltic crust, could cause isolated areas in the overlying continental lithosphere to exhibit variations in drag and buoyancy that could promote complex variability in upper plate responses of shortening and extension (Humphreys et al., 2015). The proximity of the basement buttresses at this location due to the irregular rift margin, helps to explain the involvement of Precambrian basement in the Winters Pass and Powerline Road thrusts.

Unlike the typical forward-imbrication of thrusts seen in the northern exposures of the Sevier fold-thrust-belt, we see a backward imbrication of thrusts decreasing in age towards the west, from the Keaney-Mollusk Mine thrust to the Mesquite thrust, Powerline Road/Pachalka thrust, followed by the Winters Pass thrust (Figures 23 and 24). The backward-imbrication pattern seen in this area may have been influenced by the synconvergent extension occurring just to the west and southwest of the area. This would suggest that, unlike other areas of the Mojave, where extensional forces overcame the compressional forces, the area around the Clark and Mesquite Mountains had compressive forces that were greater than the extensional forces,

creating a retrograde thrust sequence. A possible explanation to why the contractional strain in this area would be greater than the extensional strain may be due to the local NW-SE orientation of a transform zone along the rift boundary. The SW-oriented rift hinge-line is hypothesized to contain transform faults oriented ~330º (Lund, 2008; Tikoff et al., 2023). This orientation, together with the NE transport of the CSR, would exhibit its greatest compressive stress nearly orthogonal to the orientation of a transform segment of the rifted margin, rather than at an oblique angle, causing this area to exhibit stronger forces of contractional deformation relative to the overall extensional strain. Lineation measurements obtained from the fault rocks mirror the proposed transport direction of the CSR, suggesting that this was a major contributing factor to the different transport direction seen in these fault rocks compared to those elsewhere in the SFTB.

CONCLUSION

The stratigraphy and structure of the Mesquite and Clark Mountains record the development of the Late Precambrian rift along the western margin of Laurentia, the shaping of the North American Cordillera during the Sevier-Laramide orogens, and the effects of crustal thinning during Miocene extension. Flat slab subduction during the onset of the Laramide orogeny has long been thought to have ended contractional tectonics in the northeastern Mojave Desert as, unlike continued younger thrusting in the SFTB further north in Utah and Wyoming, the youngest documented shortening in the Clark Mountain thrust complex is bracketed between deposition of the Delfonte volcanic rocks (100-98 Ma) and intrusion of the Teutonia adamellite and Mid Hills adamellite (92 Ma) (Fleck et al., 1994; Walker et al., 1995; Wells, 2016). The results of this study show that the cessation of contractional tectonics and associated deformation in the Clark Mountain thrust complex are much younger than currently recognized and record the transition from Sevier to Laramide style orogenesis. The unique style of Laramide backward-imbrication and basement involved thrusting and unique kinematics of top-NW contraction, is markedly different from segments of the Sevier-Laramide orogen further north (Figures 23 and 24). The irregular geometry and kinematics of the thrust complex is influenced by several key factors. The eastward pinch out of the Pahrump Group rocks in the region demonstrate that the paleo rift margin is located in this area. The rift margin and its geometry likely influenced the involvement of basement within the thrust complex as well as the transport direction of the upper plate. The NE orientation of shortening is similar to the azimuth of plate convergence between the Farallon and North America plates during the Laramide (Saleeby, 2003), and similar to average shortening directions determine for the Laramide foreland province (Yonkee and Weil,

2015). While the Clark Mountain thrust complex contains a unique thrust geometry and stratigraphy that is attributed to its spatial relationship to the paleo-rift margin and influence of the CSR, it is likely that structures elsewhere in the Mojave record this transition to flat slab-subduction.

Age determinations on synkinematic white micas located within the mylonitic fault rocks of the western thrusts of the CMTC produce Late Cretaceous ages. The Winters Pass muscovite gives an average age of 73 Ma with the Mesquite and Pachalka fault rocks giving older ages of 81 Ma. Mylonitic rocks associated with the Powerline Road and Winters Pass thrusts show a top-NE transport direction of the upper plate, with stretching lineations mirroring the azimuth of plate convergence vectors for the Late Cretaceous (Saleeby, 2003). The change of Farallon plate's subduction angle during the Late Cretaceous is known to temporally overlap ages for local hinterland extension. Hinterland extension may drive the orogenic wedge into a sub-critical taper, triggering thrusts to propagate in a retrograde manner, explaining the regression of ages when looking at structurally higher thrusts in the complex. Around the same time, the CSR was being subducted underneath the retroarc. The shallowing of the slab associated with CSR subduction produces compressive stresses that are localized along a possible truncated zone along the paleo-rift margin, driving the NE directed transport of the upper-plate.

The rollback of the shallowly subducting Farallon slab combined with the transition from a convergent margin to a transform margin and development of the northward migrating Mendocino triple junction (and trailing slab window) during the Miocene conspired to produce large scale regional extension, dismembering many thrust sheets in the central Basin and Range. The Winters Pass thrust had been considered to be the southern correlative of the present-day Wheeler Pass thrust in the Spring Mountains. The results of this study demonstrate that the

Winters Pass, Pachalka and Powerline thrusts are in fact not correlative to the Wheeler Pass thrust as previously thought; rather they are an isolated set of thrusts imbricated in retrograde fashion off of the Keaney thrust and represent the last stages of contractional deformation in the Mojave. Petrographic and microstructural analysis of recrystallized minerals combined with ages from argon geochronology of synkinematic muscovite show that the upper-plate was not at sufficient depth or temperature during Miocene extension to completely overprint the mylonitic fabrics or the ages of synkinematic mica. The KHDF, developed during the Miocene, did play a role in exhuming the exposures of the basement-involved thrust. Cretaceous thrust-related mylonitic fabrics were brought to the surface due to the isostatic rebound of the lower-plate during the removal of rocks in the upper-plate of the KHDF. This explains the east dipping portion of the thrust in the westernmost parts of the field area and why mylonitic fabrics are restricted to the western portions of the fault trace in the Mesquite Mountains.

APPENDICES

Appendix A: Figures

Figure 1. Simplified tectonic map of the North American Cordilleran system illustrating locations of retroarc contractional belts (after Giallorenzo et al., 2018). Approximate locations of passive-margin hinge zone and interpreted late Paleozoic (Pz) transform fault system that truncated the plate margin (Dickinson, 2008) are indicated. Box shows location of Figure 2.

Figure 2. Simplified geologic map of the Mojave with pre-Tertiary reconstruction. (A) Simplified geologic map of the study region showing present-day fault geometry and names of major ranges. NV—Nevada; UT—Utah; AZ—Arizona; CA—California; fz—fault zone; sz—shear zone. Dashed box represents the study area including the NW Clark Mountains (CM), Kingston Range (KR) and Mesquite Mountains (MM) of southeastern California. (B) Pre-Tertiary reconstruction of thrust sheet correlations based on Snow and Wernicke (2000). Colored circles are geographic register points to correlate restoration.

Figure 3. Geologic map of the NW Mesquite Mountains after Calzia et al., 2000. Important relationships to note include trace of Winters Pass thrust placing Paleoproterozoic basement over Crystal Spring Formation in southwest and over folded Neoproterozoic to Cambrian strata in the northwest; trace of Kingston-Halloran detachment placing tilted panels of Cambrian strata over Paleoproterozoic basement, and unconformity between Ediacaran Noonday Dolomite and Paleoproterozoic basement. Cross section lines A-A', B-B', C-C', D-D' are indicated.

Figure 4. Geologic cross-sections of the NW Mesquite Mountains**.** Note the close proximity of the KHDF to the WPT in some sections. The WPT exhibits an eastward dip towards the western portions of the field area which transitions to a westward dip when moving to the east. Hanging wall and footwall folds are seen in the Neoproterozoic-Cambrian sedimentary strata. Sections indicated include A-A', B-B', C-C' and D-D'.

Figure 5. Stereonet data for the NW Mesquite Mountains: Stereograms of (A) mylonitic foliation and (B) stretching lineation from shear zone in Proterozoic basement. Foliation data shows two dominant foliation directions outlined in red and blue. Lineation measurements show a consistent NE-SW orientation. (C) stereogram of folded Ediacaran to Cambrian strata in NW Mesquite Mountains, in the hanging wall of the Winters Pass thrust showing a NW trending axis suggesting NE vergence.

Figure 6. Slip systems in quartz and associated c-axis pole figures. (A) A schematic of the four possible slip-systems in quartz and the associated c-axis pole figures for sinistral shear, modified from Fossen (2016). Slip systems are temperature and strain rate dependent, with temperature increasing to the right. (B) Predicted CPO patterns for c-axes and a-axes in quartz shown for different temperature-dependent deformation mechanisms and their associated slip systems displayed for dextral simple shear. BLG - bulge recrystallization, SGR - subgrain rotation, GBM - grain boundary migration. From Passchier and Trouw (2005).

Figure 7. Simplified geologic map of the NW Mesquite Mountains showing sample locations for EBSD and geochronology. Lithology is differentiated by rock type and age: brown - Precambrian metamorphic rocks, green – Precambrian sedimentary rocks, blue – Cambrian sedimentary rocks. Detachment and thrust fault traces are indicated. Pink stars indicate EBSD sample locations, yellow stars indicate sample locations for muscovite geochronology.

Figure 8. Simplified geologic map of the NW Clark Mountains showing locations of EBSD and geochronology samples. Lithology is differentiated by rock type and age: Red – Precambrian metamorphic rocks, green – Precambrian sedimentary rocks, blue – Cambrian sedimentary rocks, yellow – Jurassic igneous rocks. Thrust fault trace, foliation measurements, and fold axes are indicated. Pink stars indicate EBSD sample locations, yellow stars indicate sample locations for muscovite geochronology.

Figure 9. Photomicrographs of muscovite mineral separates used for $^{40}Ar/^{39}Ar$ age determination experiments. (A) HK21-MM4. (B) HK21-MM5. (C) HK22-MM10. (D) HK22-MM12. (E) HK22-MM29. (F) HK23-MM36. (G) HK22-CM4. (H) HK22-CM5. (I) HK22-CM11

Figure 10. Field photos showing kinematic indicators within mylonitic orthogneiss throughout the Mesquite Mountains. (A) S-C fabric developed within ultramylonite, top-NE shear. (B) Asymmetric feldspar porphyroclasts in sinistral rotation, top-NE. (C) Asymmetric pegmatitic

dike within ultramylonite zone showing sinistral rotation, top-NE. D. Asymmetric feldspar porphyroclasts in sinistral rotation, top-NE.

Figure 11. Kinematic indicators in thin section: (A) Sinistral σ-type porphyroclast of feldspar in HK21-MM1. (B) Bookshelf structure in brittlely deformed feldspar and C' shear bands showing dextral shear in HK21-MM6. (C) sinistral δ-type porphyroclast of feldspar in HK21-MM10. (D) sinistral δ-type porphyroclast of feldspar in HK21-MM10. (E) Bookshelf structure in brittlely deformed feldspar showing sinistral shear in HK22-MM29. (F) Sinistral σ-type porphyroclast of feldspar in HK22-MM29. Mineral key: Dyn qz – dynamically recrystallized quartz; Pl – plagioclase; Ms – muscovite

Figure 12. Photomicrographs illustrating the chemical breakdown of plagioclase and K-feldspar to muscovite, quartz, and albite. Note the growth of synkinematic white mica within the cores and around the rims of feldspar grains. Quartz, albite and muscovite can be seen growing in dilatant sites (strain fringes and along fractures) suggesting breakdown occurred during shearing. Mineral key: Kfs - K-feldspar, Dyn qz - dynamically recrystallized quartz, Ms - muscovite, Ab – albite

Figure 13. SEM EDS maps of mylonitic orthogneiss showing development of synkinematic secondary phases. Potassium (green) from orthoclase can be seen producing major contributions to the growth of muscovite with quartz and albite produced as byproducts, infilling dilatant sites. Minerals include muscovite (teal), quartz (red), orthoclase (green) and albite (brown/purple).

Elemental key: Green – potassium; red – silica; blue – aluminum; yellow – sodium; white – electron image. Mineral key: Qz – quartz; Ms – muscovite; Kfs – K-feldspar; Ab – albite. Foliation is defined by pulled apart K-feldspar porphyroclasts, quartz ribbons, and bands of fine-grained albite and muscovite, suggestive of diffusive mass transfer processes to produce albite, muscovite and some quartz, and dislocation creep in quartz. (A.) HK21-MM6 (B.) HK21-MM6 (C.) HK22-MM19 (D.) HK22-MM19 (E.) HK22-MM29 (F.) HK22-MM29

Figure 14**.** High magnification SEM EDS maps of mylonitic orthogneiss showing development of synkinematic secondary phases. Orthoclase (green) can be seen mixed with plagioclase (purple) along with quartz (red) and muscovite (blue) within extremely fine-grained bands, further suggesting fluid-assisted diffusion creep of feldspars played a big role in deformation in this rock and lead to the formation of secondary muscovite, feldspar and quartz. Elemental key: Green – potassium; red – silica; blue – aluminum; yellow – sodium; white – electron image. Mineral key: Qz – quartz; Ms – muscovite; Kfs – K-feldspar; Ab – albite. (A.) HK22-MM19 (B.) HK22-MM29 (C.) HK22-MM19 (D.) HK22-MM19 (E.) HK22-MM29 (F.) HK22-MM19

Figure 15. Misorientation to mean maps**:** Misorientation to Mean orientation maps of quartz for four samples. Key on right of image represents degrees of misorientation. Dark blue colored grains indicate recovered grains with little to no misorientation within the crystal lattice. Hotter colors represent progressively more degrees of misorientation within the lattice. Note the small abundance of grains with accumulated misorientation (warm) vs. the vast number of recovered grains (cold). (a.) HK21-MM6 (b.) HK22-MM19 (c.) HK22-MM22 (d.) HK22-CM9

Figure 16. (A) Diagram showing the relationship between crystallographic vorticity axes and foliation and lineation in rock samples for different deformation strain paths. (B) Vorticity axis pole figure pattern predictions for each deformation strain path seen in (A). Areas highlighted in orange represent the area where the predicted vorticity axis can lie relative to the foliation surface in each geometry. From Brown (2022) after Michels et al. (2015) and Giorgis et al. (2016).

Figure 17. Bulk quartz CVA data for all samples: Quartz vorticity axes for all samples using a Grain orientation spread (GOS) value of 0. All samples indicate a transtensional deformation geometry with the exception of HK22-CM9, which indicates simple shear.

Figure 18. Contoured quartz CVA data for all samples on grains with accumulated misorientations >0.5 (GOS values range from 0.5-3). The CVA patterns for samples HK22-MM16, HK22-MM22, HK22-MM28, HK22-MM29 and HK22-CM9 suggest simple shear with samples HK21-MM6, HK22-MM13 and HK22-MM19 suggesting triclinic transpression.

Figure 19. EBSD-derived pole figures (PF) of dynamically recrystallized quartz for all samples rotated into the vorticity-normal reference frame determined from the CVA plots in Figure 17. Lineation azimuth for each sample provided in upper right with half arrow. Inclination of the shear plane in all samples indicates top to the NE sense of shear. (0001) - c-axis; $[\overline{1}\overline{1}20]$ - a-axis

upper and lower hemisphere projections. Active slip systems include basal <a> and rhomb <a> indicating low-temperature deformation of around ~350-425° C. X direction represents lineation and Y direction represents foliation normal.

Figure 20. Inverse pole figures (IPF) of dynamically recrystallized quartz for all samples rotated into the vorticity reference frame determined from the CVA plots in Figure 17. 'X' represents the direction of lineation. 'Y' represents foliation normal. $[\bar{1}\bar{1}00]$ - m direction; [0001] - c direction; $[01\bar{1}0]$ - m direction. Active slip systems include basal <a> and rhomb <a> with minor contributions of prism <a> (Figure 6). IPF slip systems match the slip systems interpreted from PF in Figure 18, indicating PF plots are being observed in the correct reference frame. Slip systems inferred from IPF plots also indicate deformation temperatures of around ~350-425° C.

Figure 21. $^{40}Ar/^{39}Ar$ age spectra (red) and respective K/Ca ratios (blue) for synkinematic muscovite collected from the Mesquite Mountains and Clark Mountain mylonitic orthogneiss. All samples show a similar degassing pattern with 'mini' plateaus forming at ~73 Ma for the Mesquite Mountains (MM) samples and ~81Ma for the Clark Mountain (CM) samples.

Figure 22. Composite of all muscovite $^{40}Ar/^{39}Ar$ age spectra for the Mesquite and NW Clark Mountains. Note the similarity in age spectra for the two samples from the Powerline thrust shear zone (CM4 and CM5), and the similarity between three samples from the Winters Pass mylonite (MM4, MM5, and MM10). Gray bars indicate hypothesized range of ages for

deformation if it were to be Late Jurassic or Miocene. All samples share a similar degassing pattern. Sample HK23-MM36 is excluded from this figure.

Figure 23. Schematic diagram showing out-of-sequence thrusting. Different time steps illustrate thrusts breaking backwards toward the left from the frontal thrust. Numbers represent the order of thrust fault development overtime. Based on this model, the third thrust (leftmost thrust) would represent the Winters Pass thrust with 2 representing the Mezquite thrust and 1 representing the Keaney-Mollusk Mine thrust. From Boyer, S. E., & Elliott, D. (1982)

Figure 24. Normal sequence of a propagating thrust system. Schematic diagram showing the forward propagation of thrusts as is seen with thrust systems in the Sevier fold and thrust belt. Thrusts get progressively younger moving towards the right. From Boyer, S. E., & Elliott, D. (1982)

Figure 1. Geo-tectonic map of North America

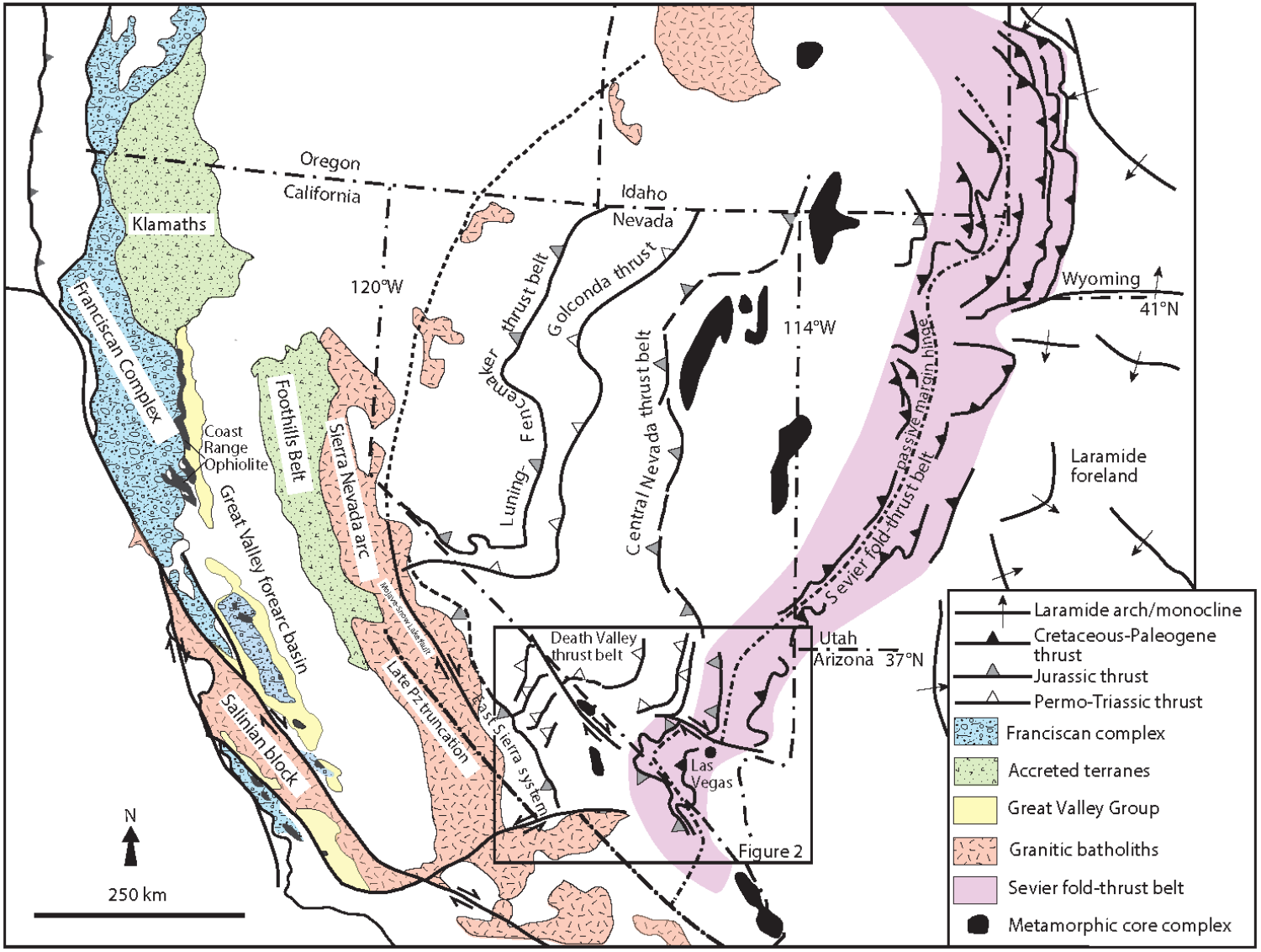

Figure 2. Simplified geologic map of the Mojave with pre-Tertiary reconstruction.

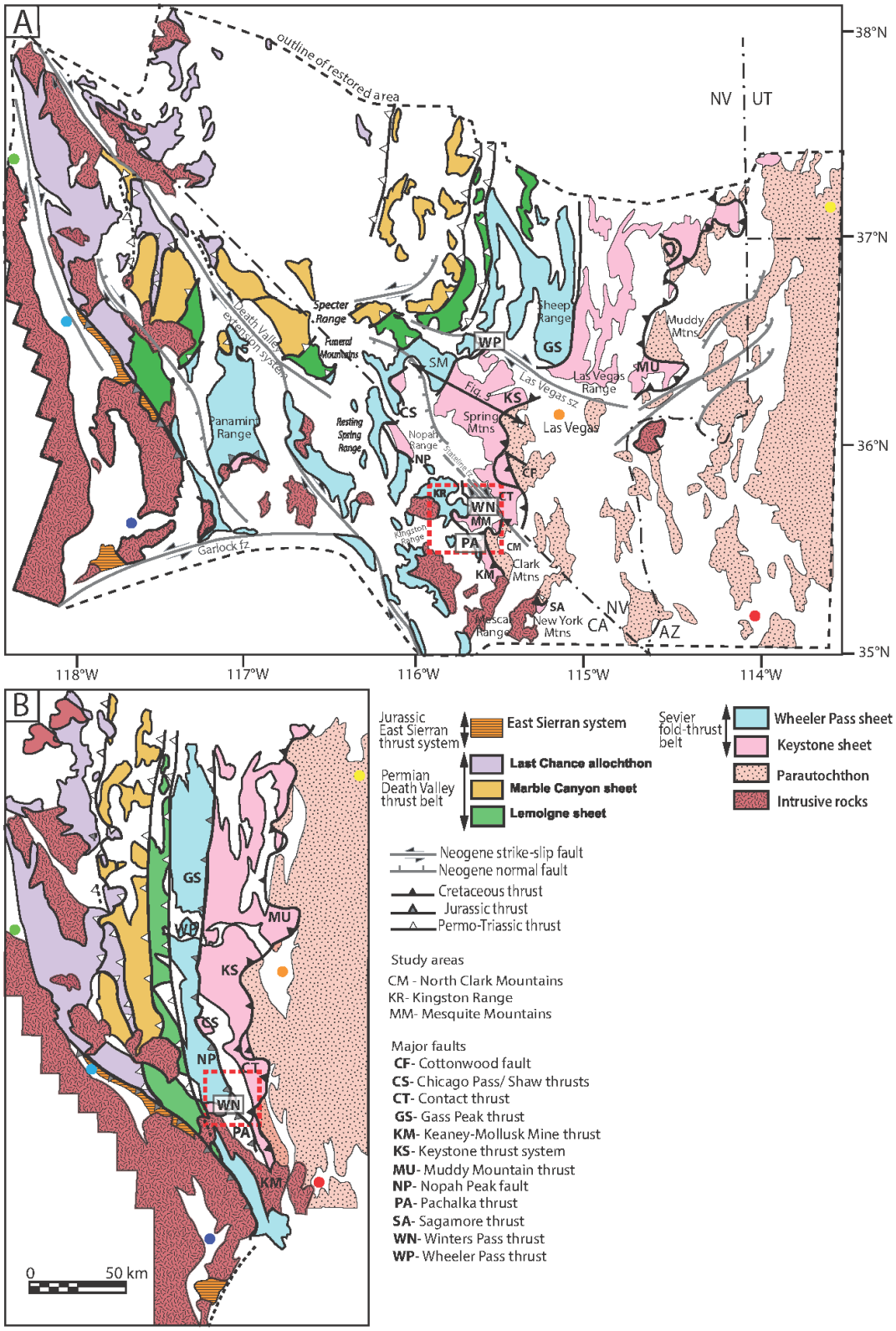

Figure 3. Geologic map of the NW Mesquite Mountains

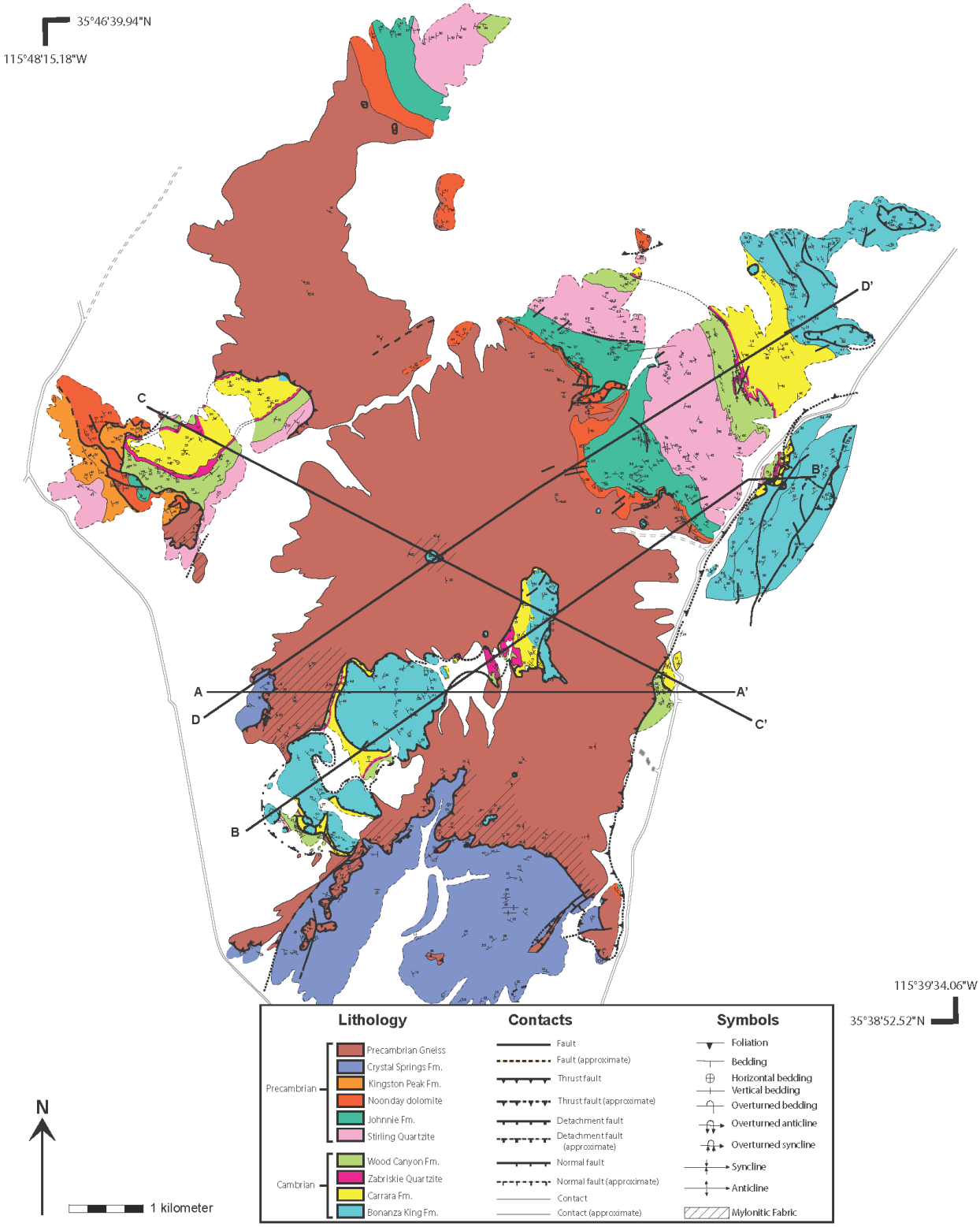

Figure 4. Geologic cross-sections of the NW Mesquite Mountains

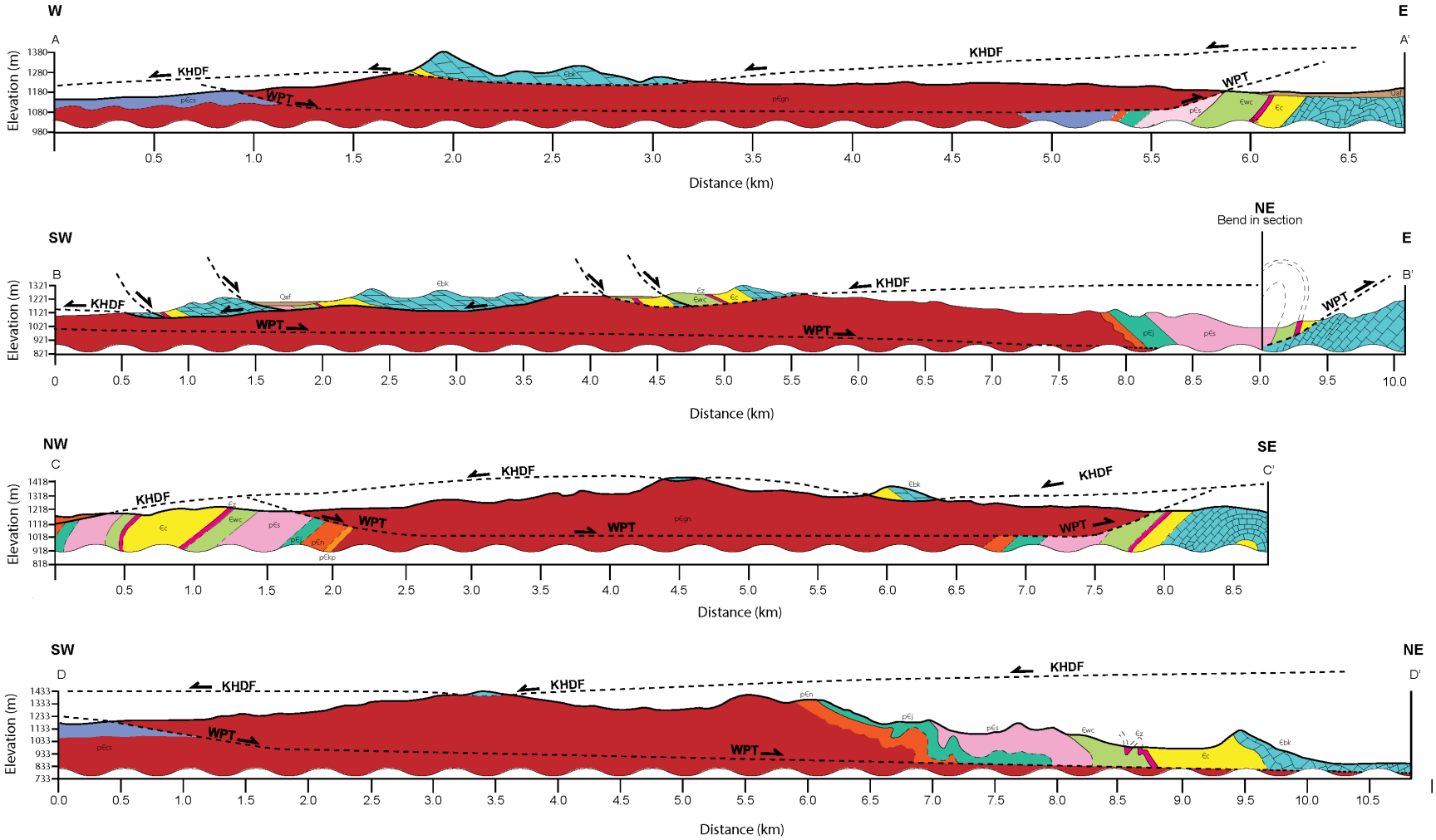

Figure 5. Stereonet data for the NW Mesquite Mountains

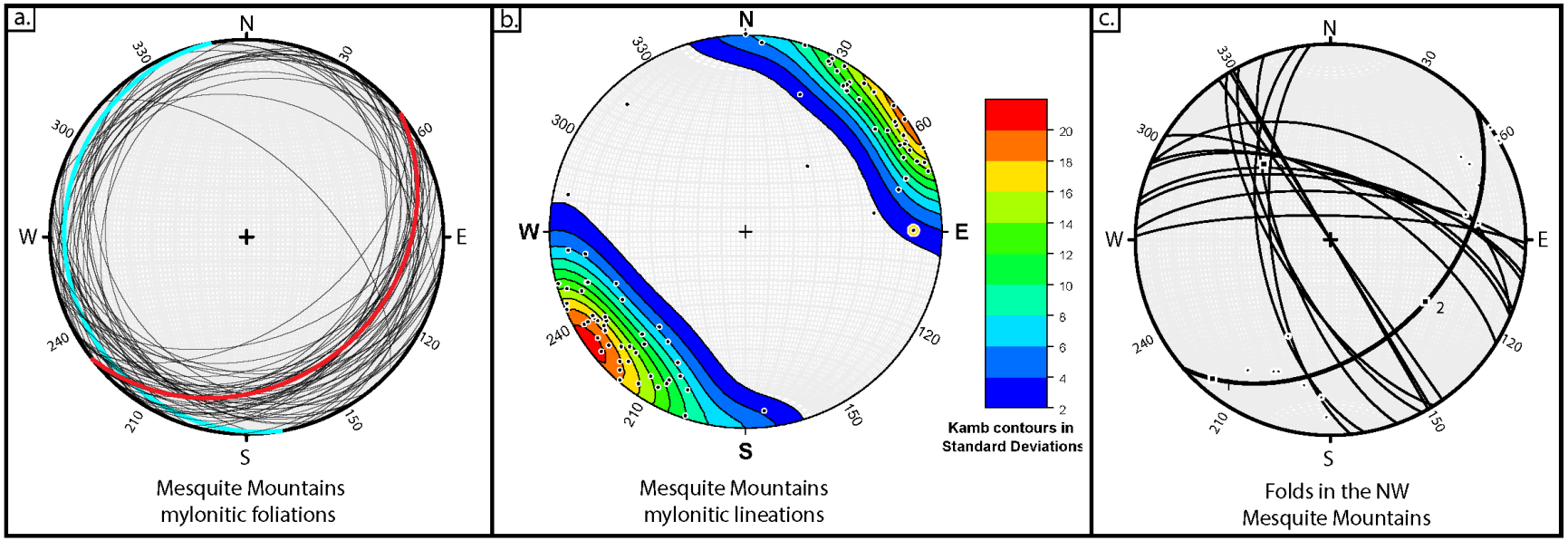

Figure 6. Slip systems in quartz and associated c-axis pole figures

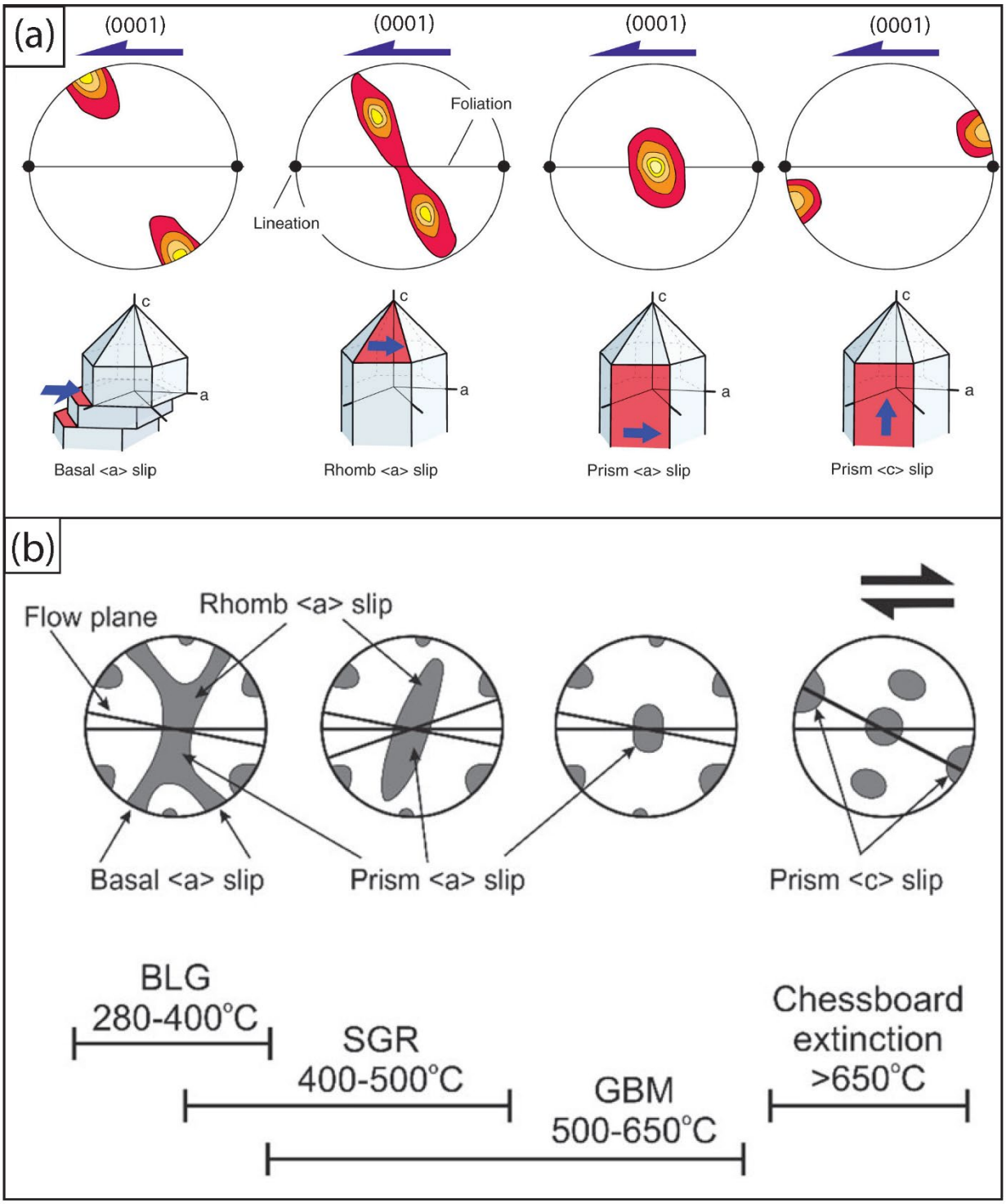

Figure 7. EBSD and geochronology sample locations for the NW Mesquite Mountains

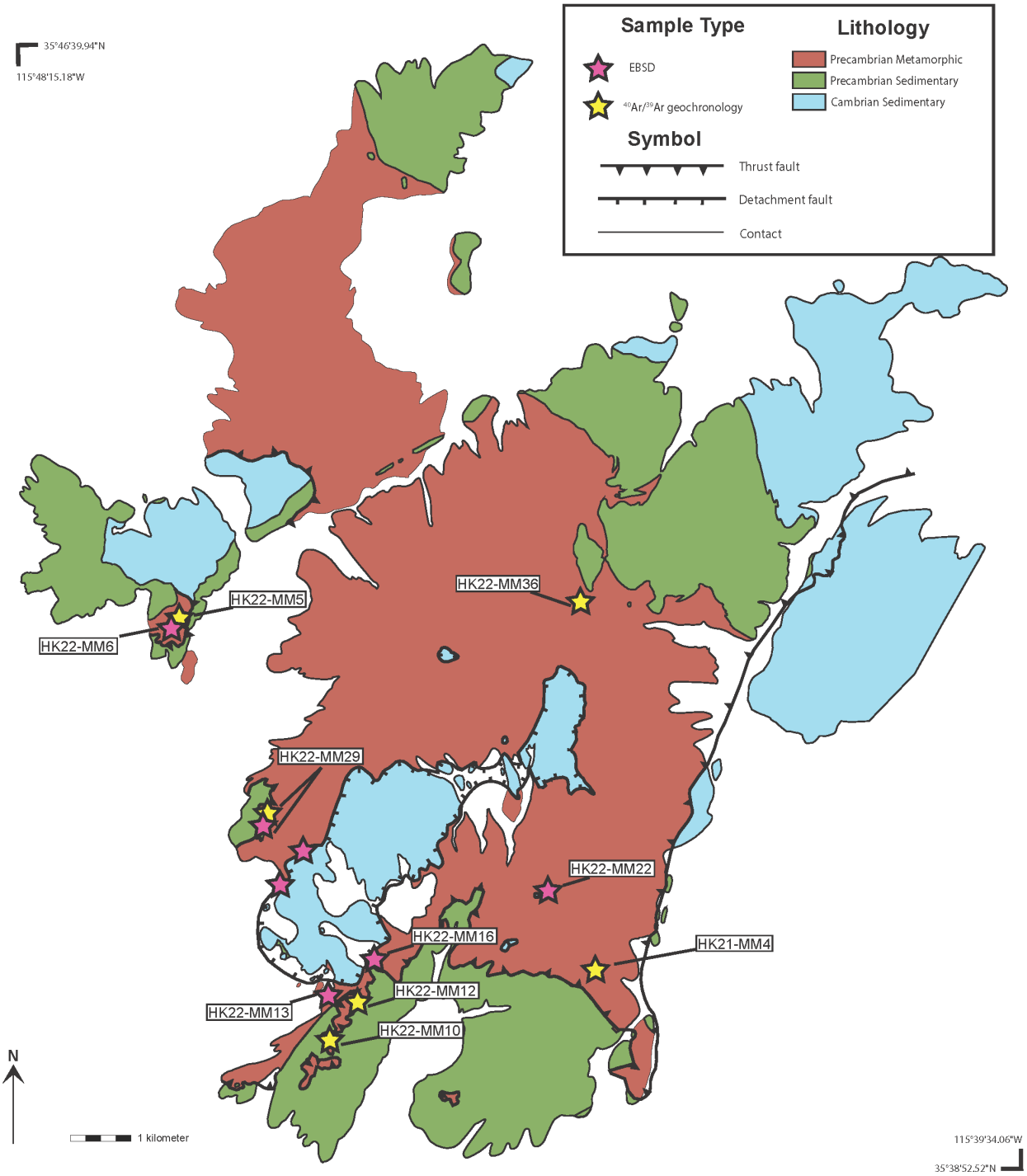

Figure 8. EBSD and geochronology sample locations for the Clark Mountains

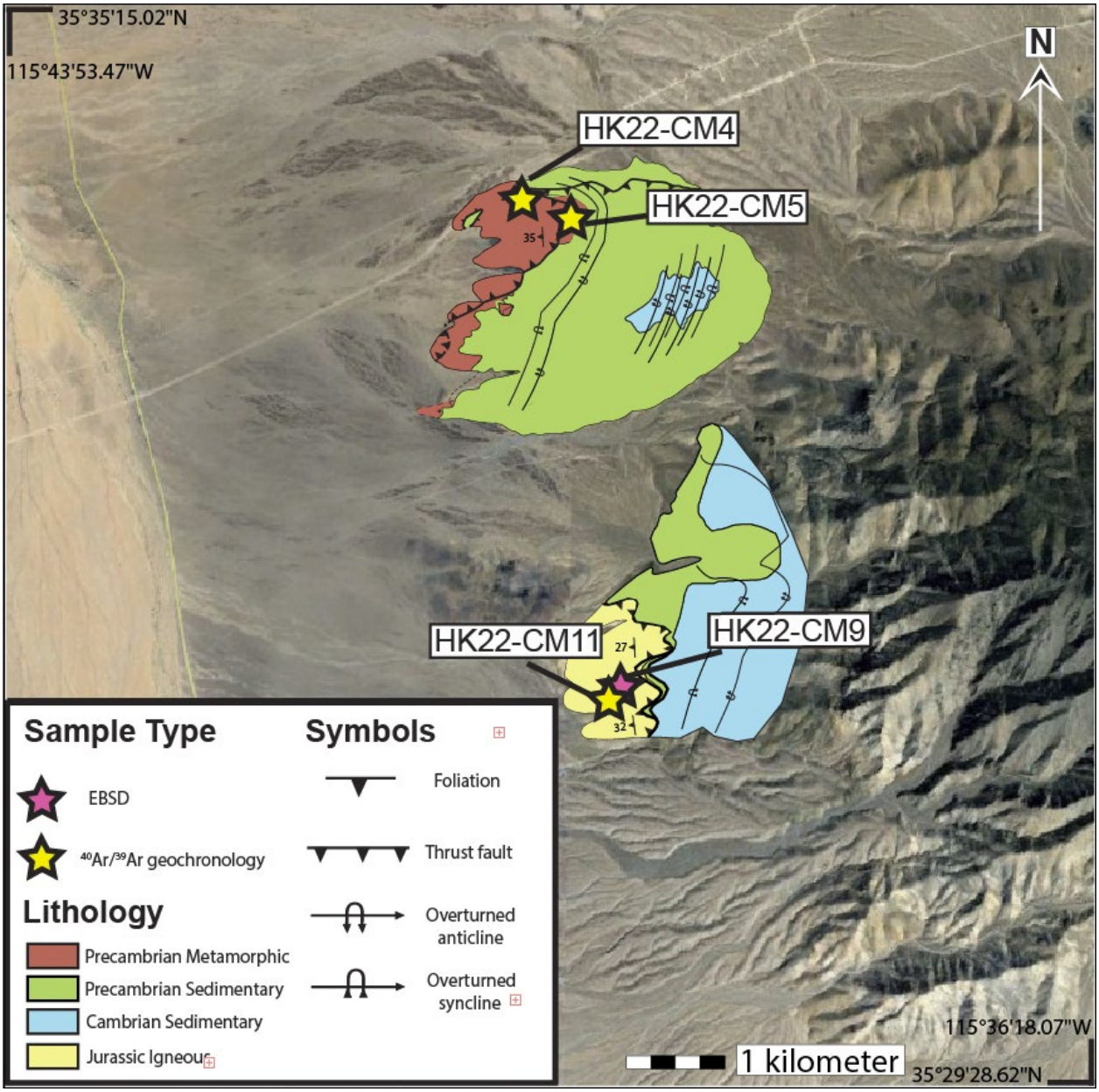

Figure 9. Final muscovite mineral separates used for $^{40}Ar/^{39}Ar$ geochronology

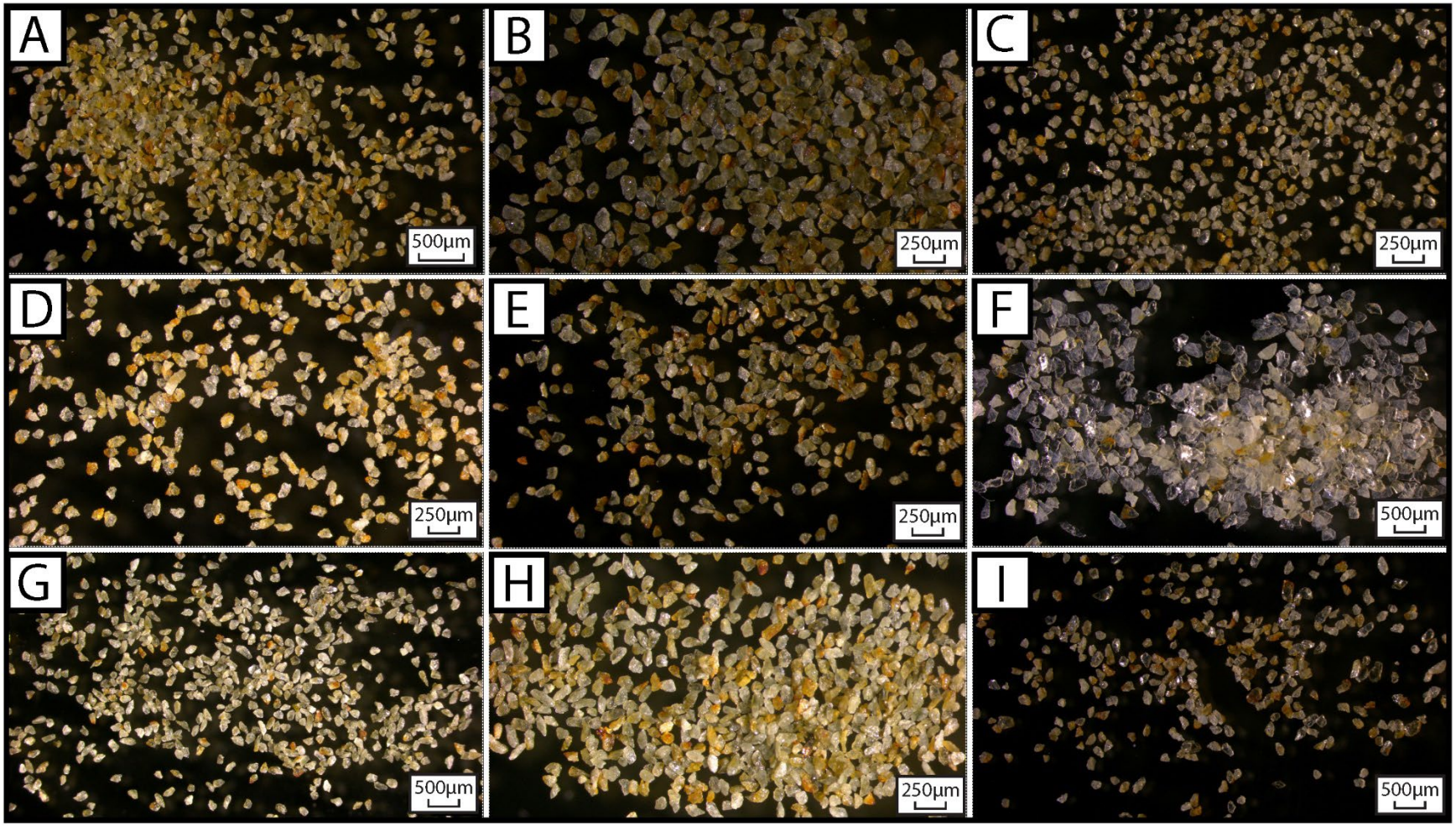

Figure 10. Kinematic indicators in the field

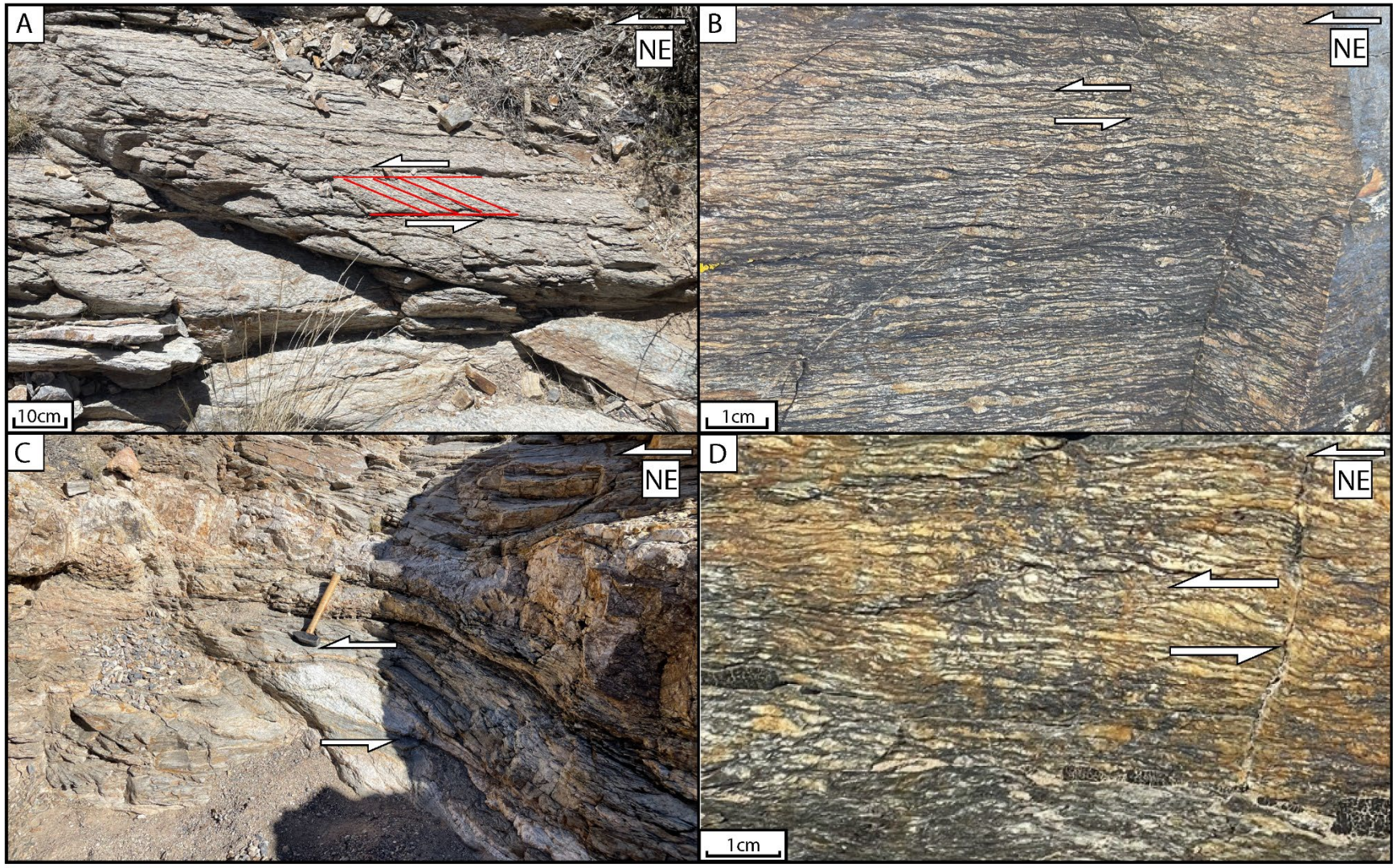

Figure 11. Kinematic indicators in thin section

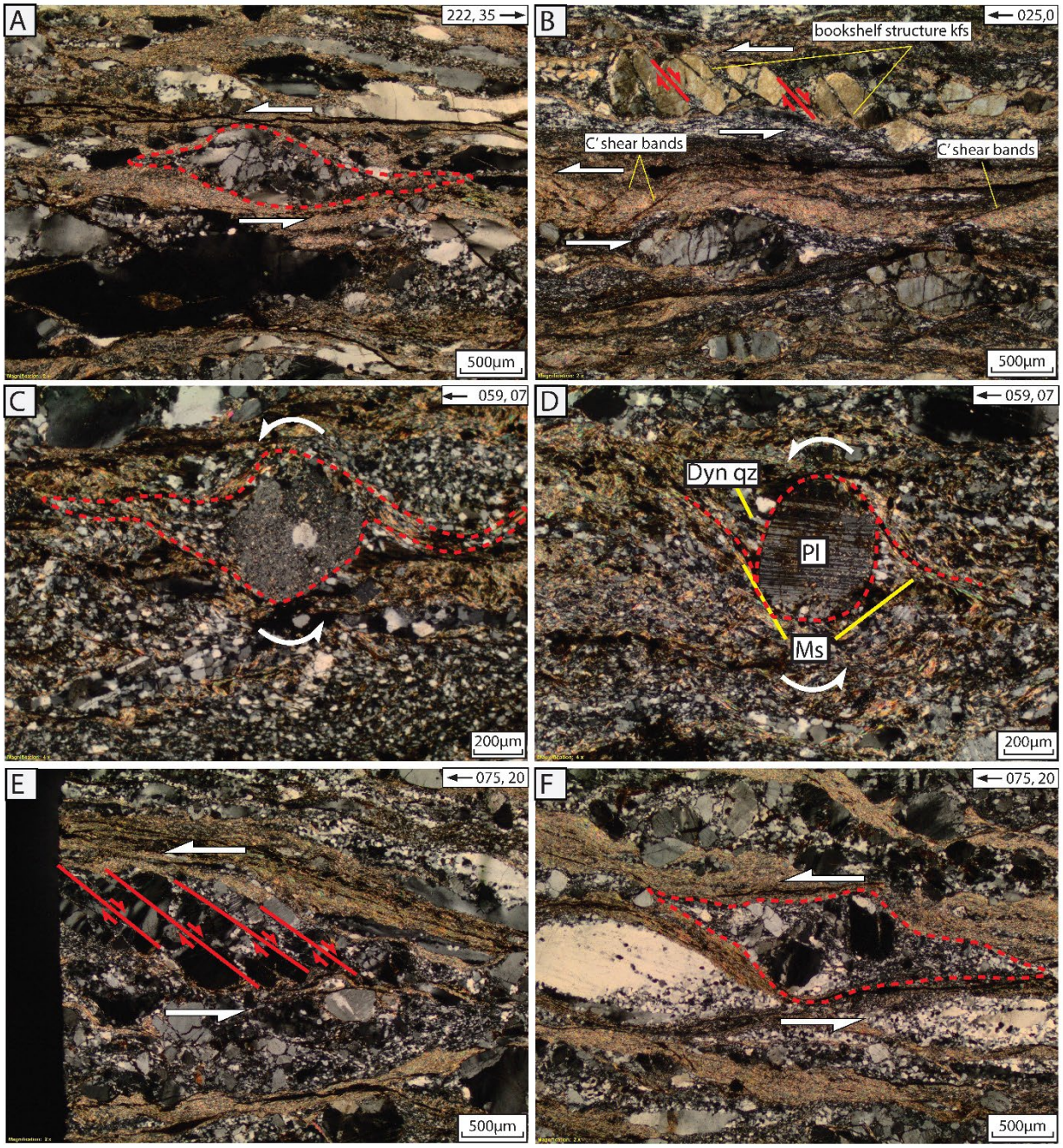

Figure 12. Feldspar breaking down to produce muscovite.

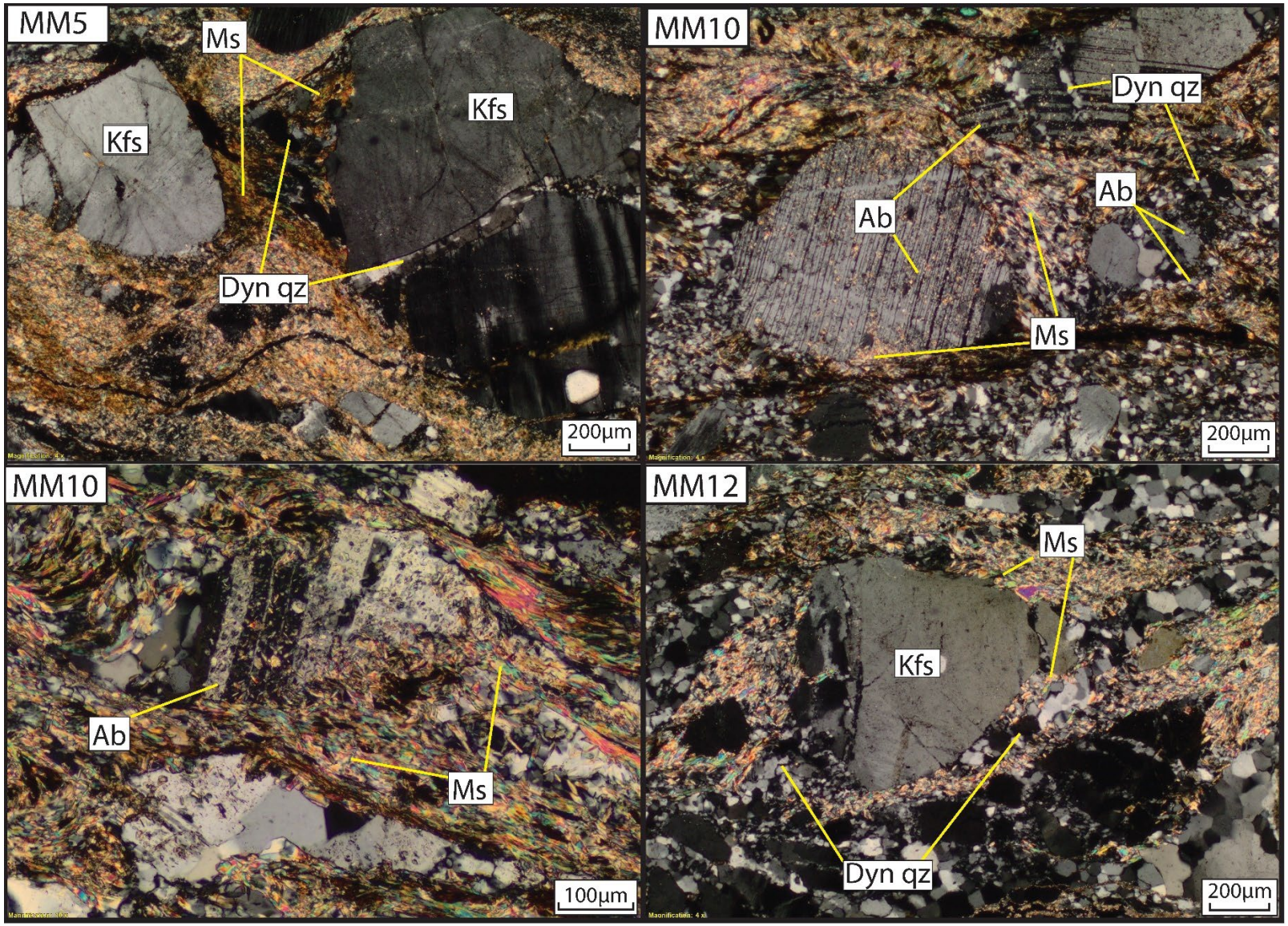

Figure 13. EDS maps of feldspar reaction rims

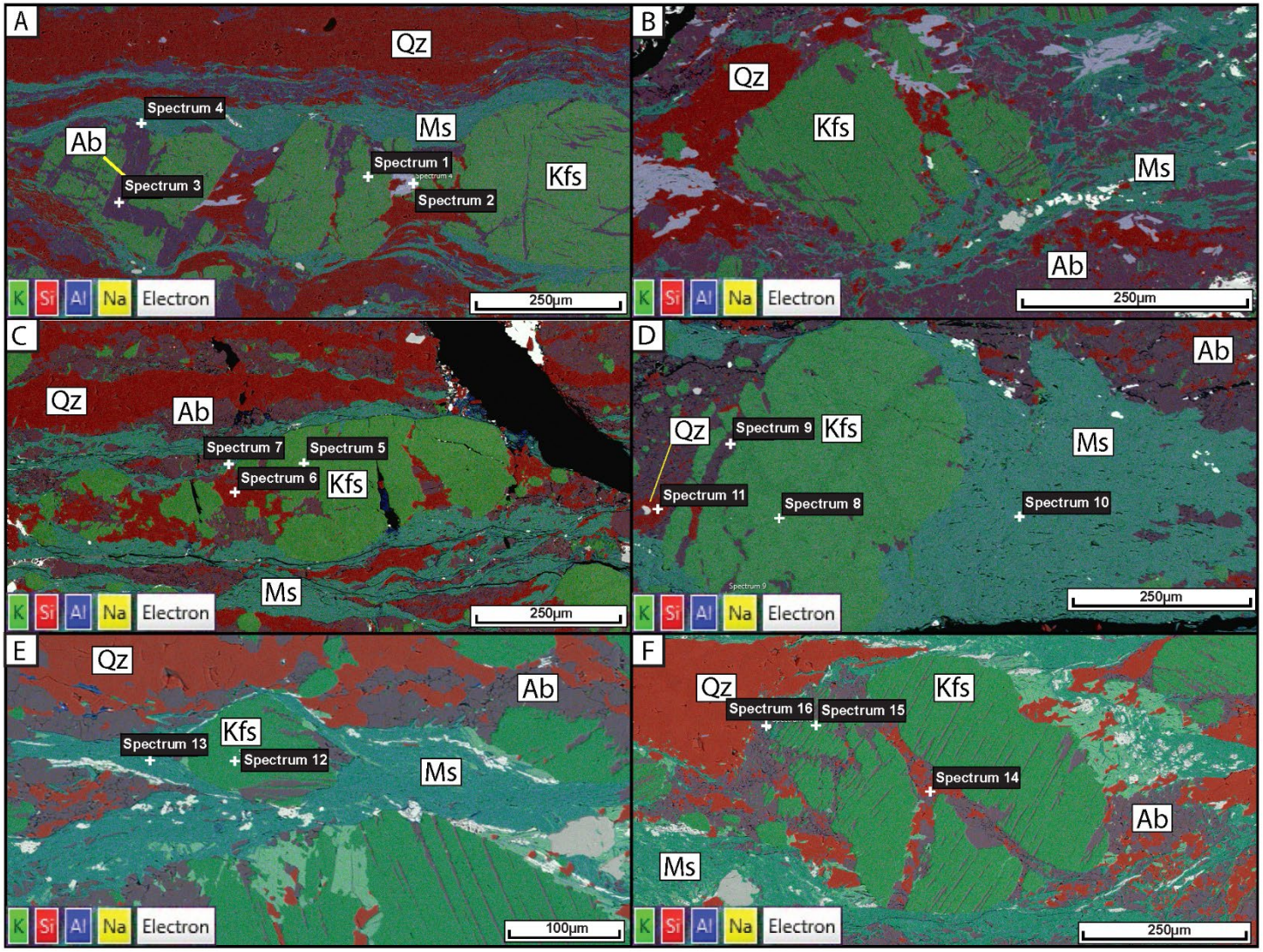

Figure 14. High magnification EDS maps

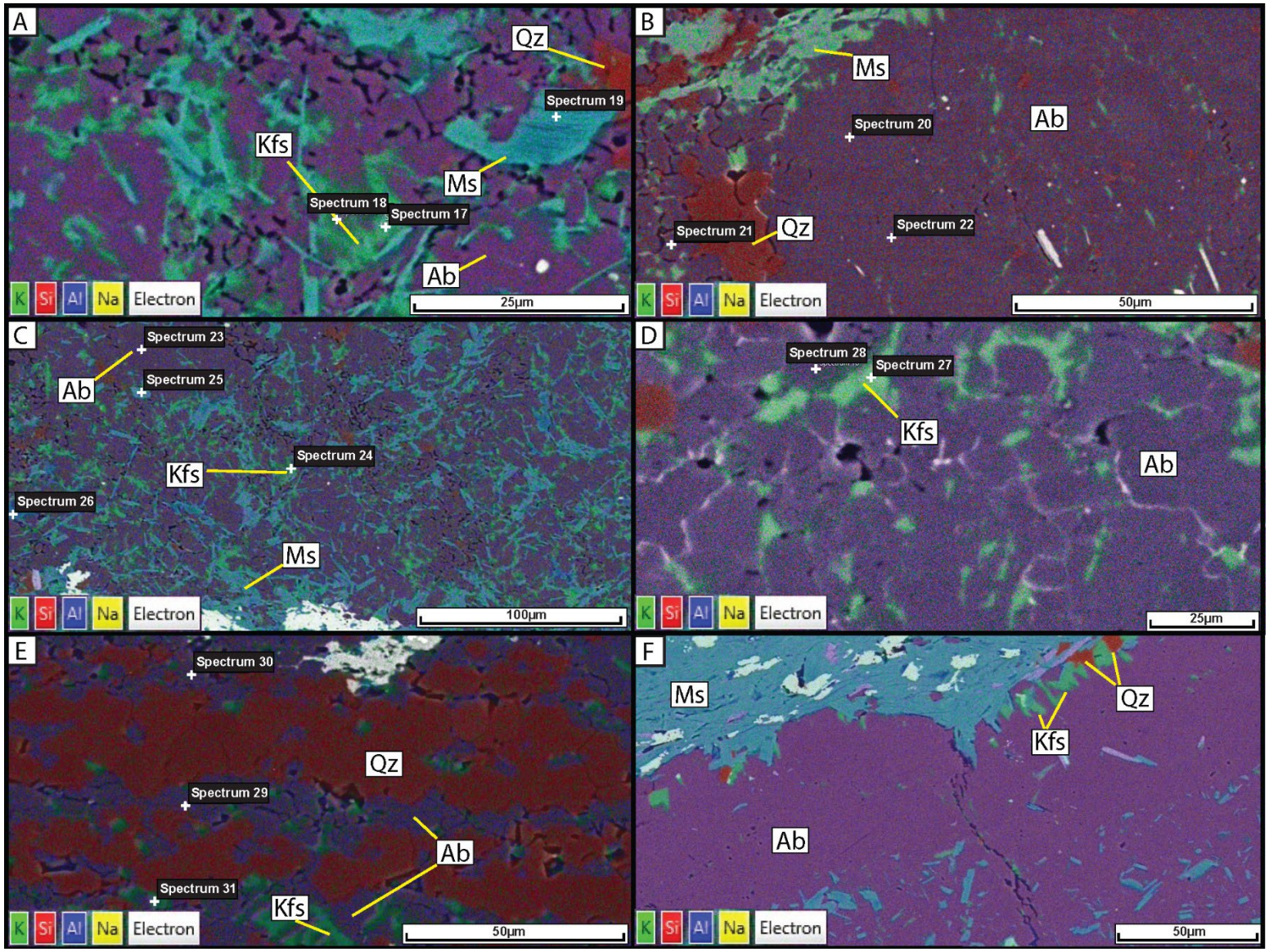

Figure 15. Misorientation to mean maps

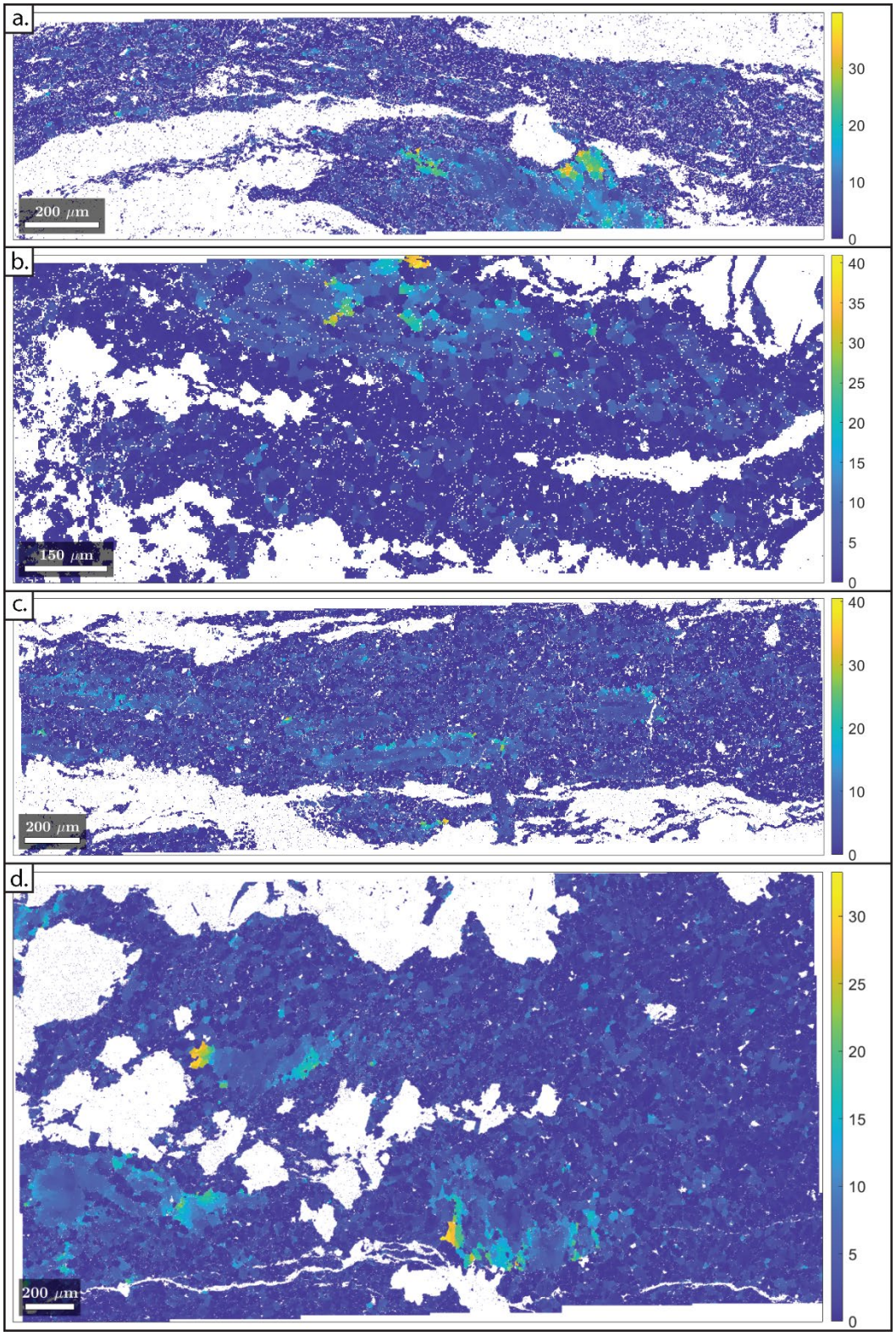

Figure 16. CVA plots for different deformation geometries

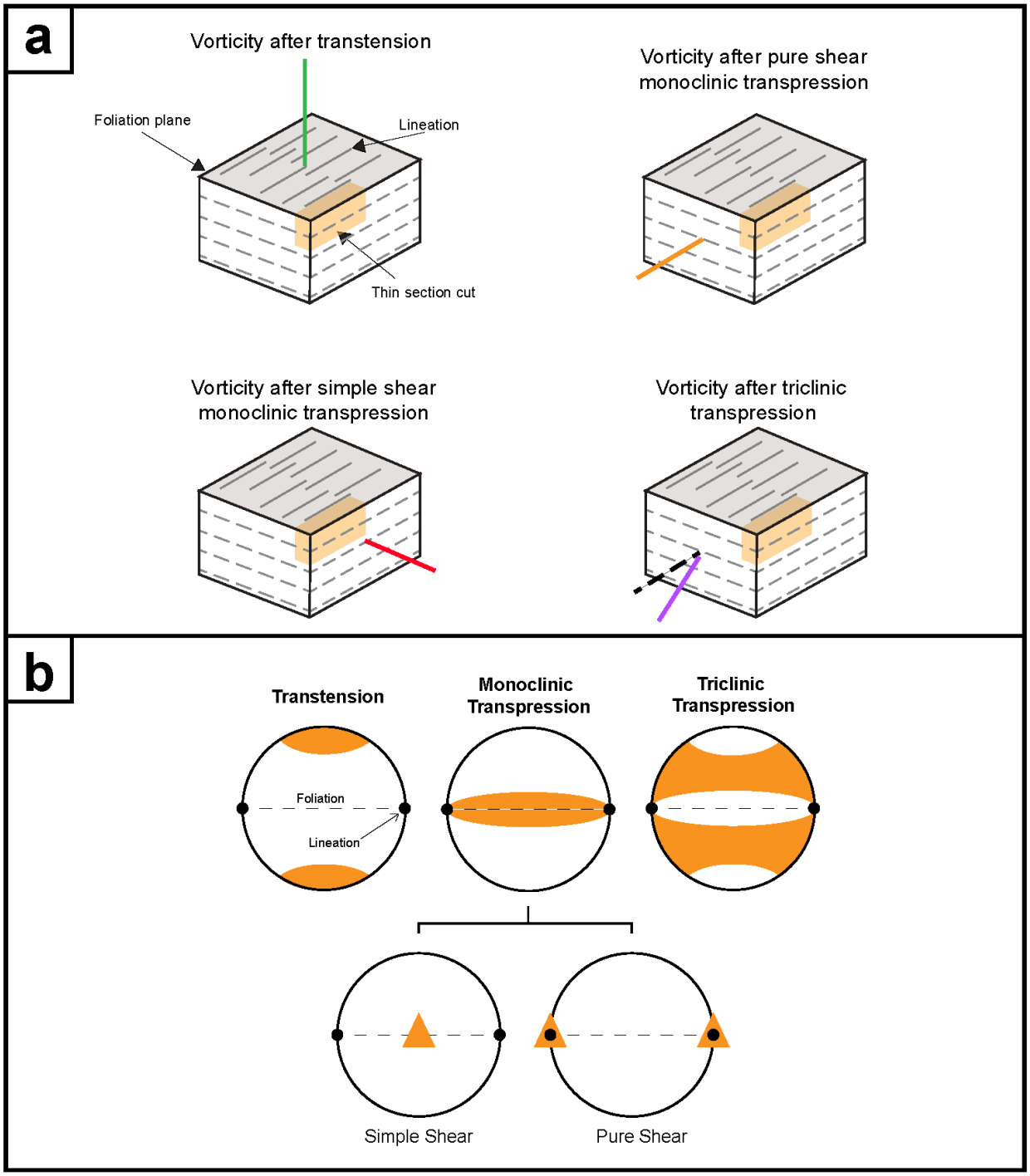

Figure 17. Bulk quartz CVA data for all samples

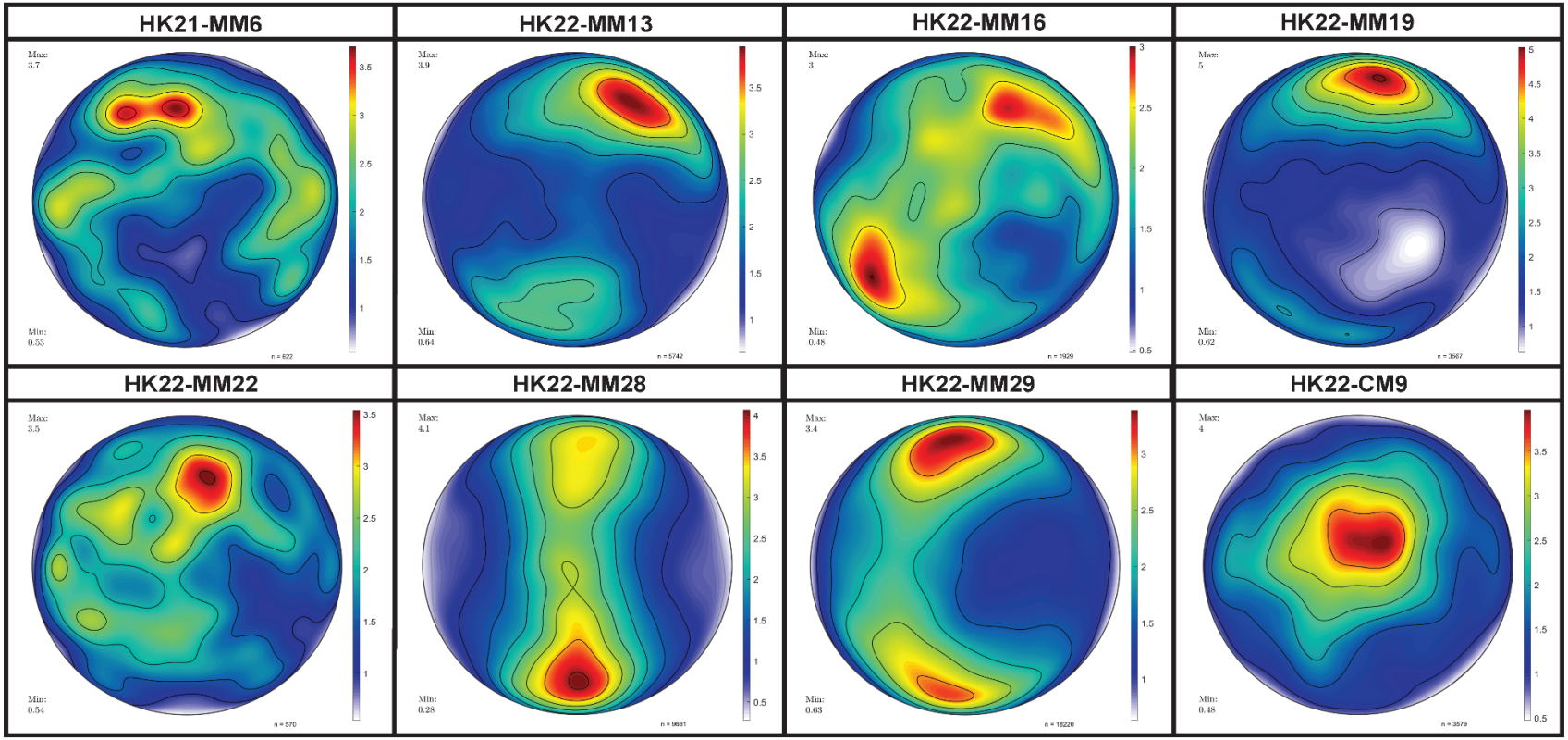

Figure 18. Quartz CVA data on grains with accumulated misorientations

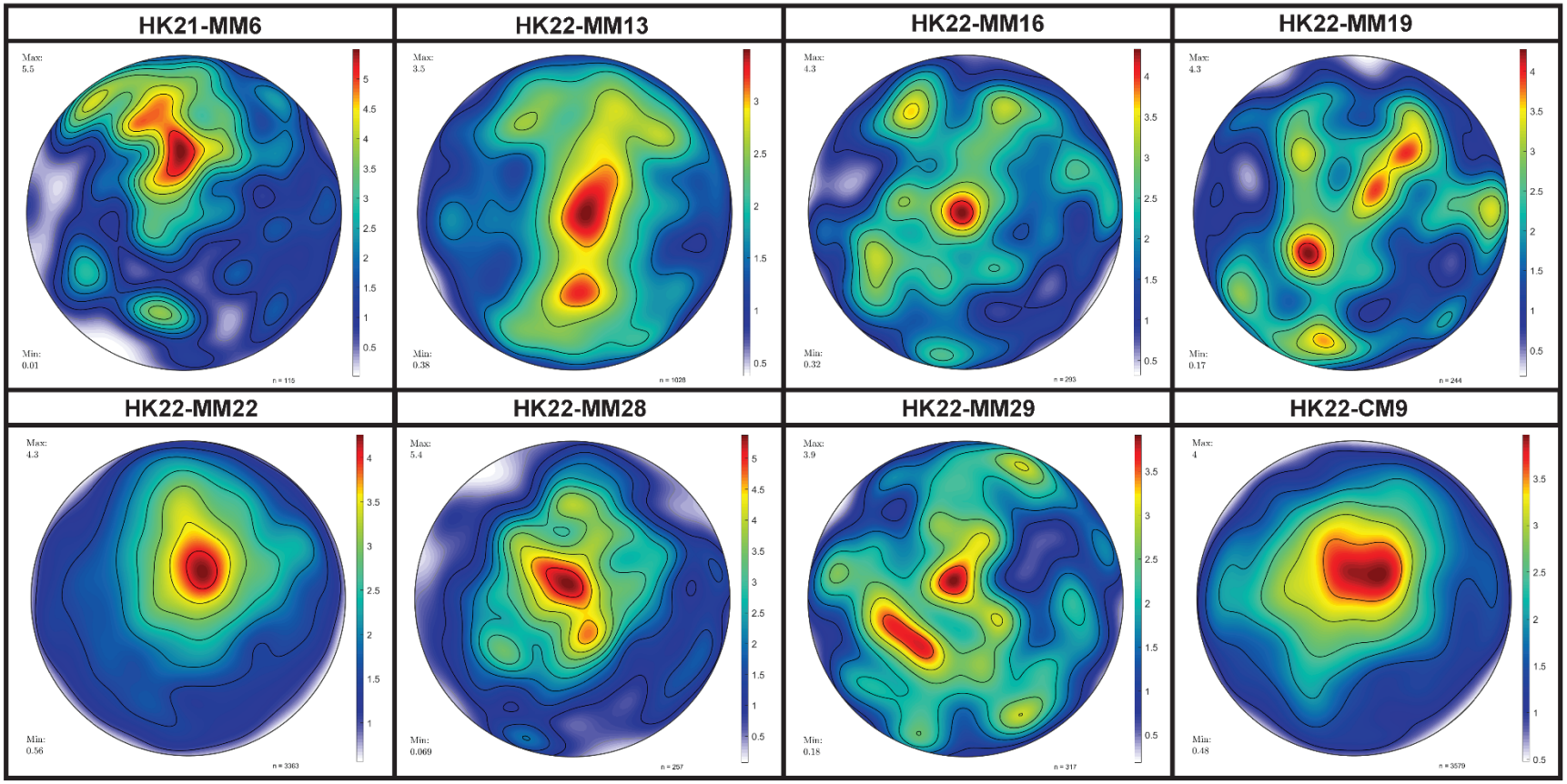

Figure 19. Pole figures for quartz in the vorticity reference frame

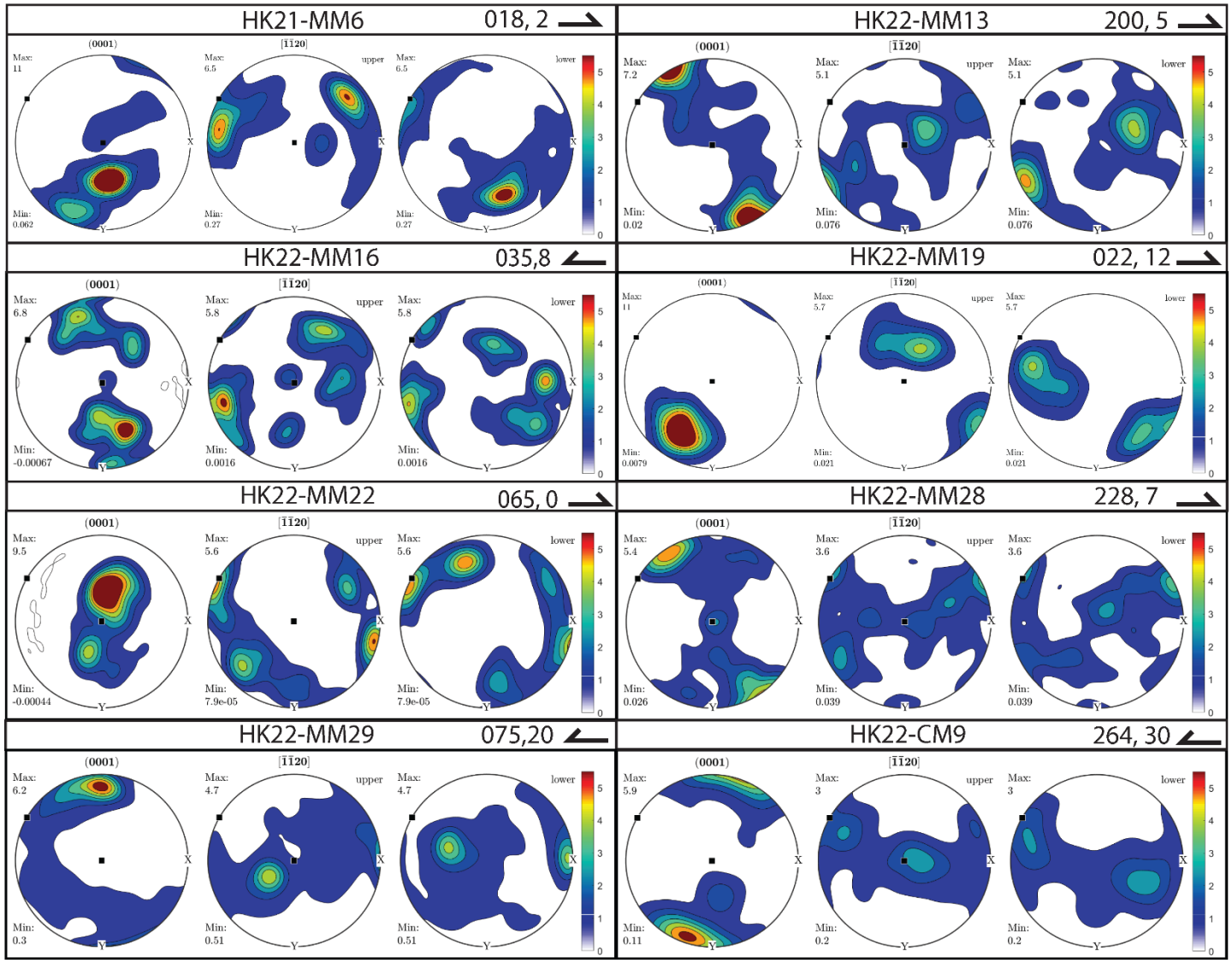

Figure 20. Inverse pole figures for quartz in the vorticity reference frame

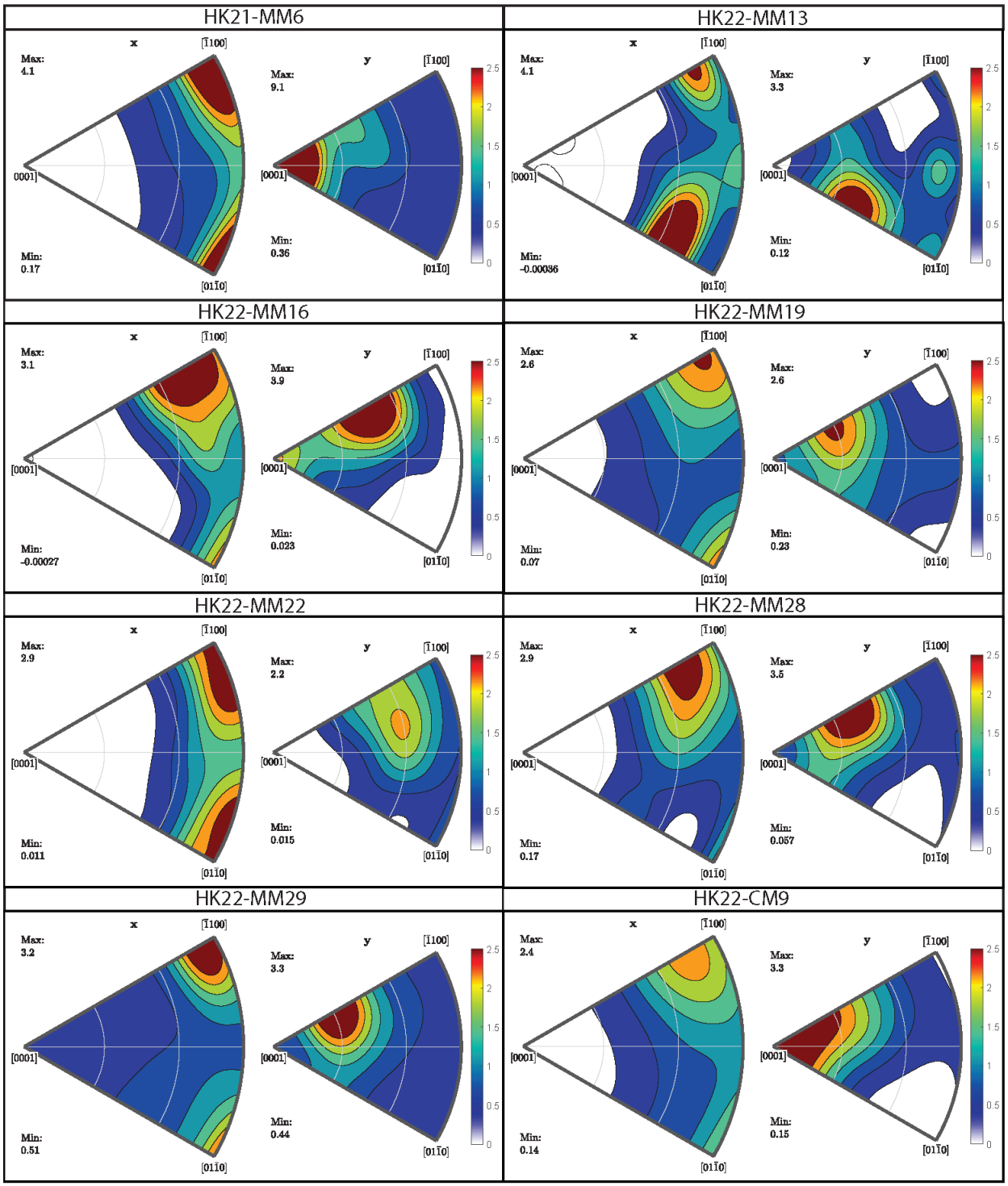

Figure 21. $^{40}Ar/^{39}Ar$ age spectra with K/Ca ratios for all samples

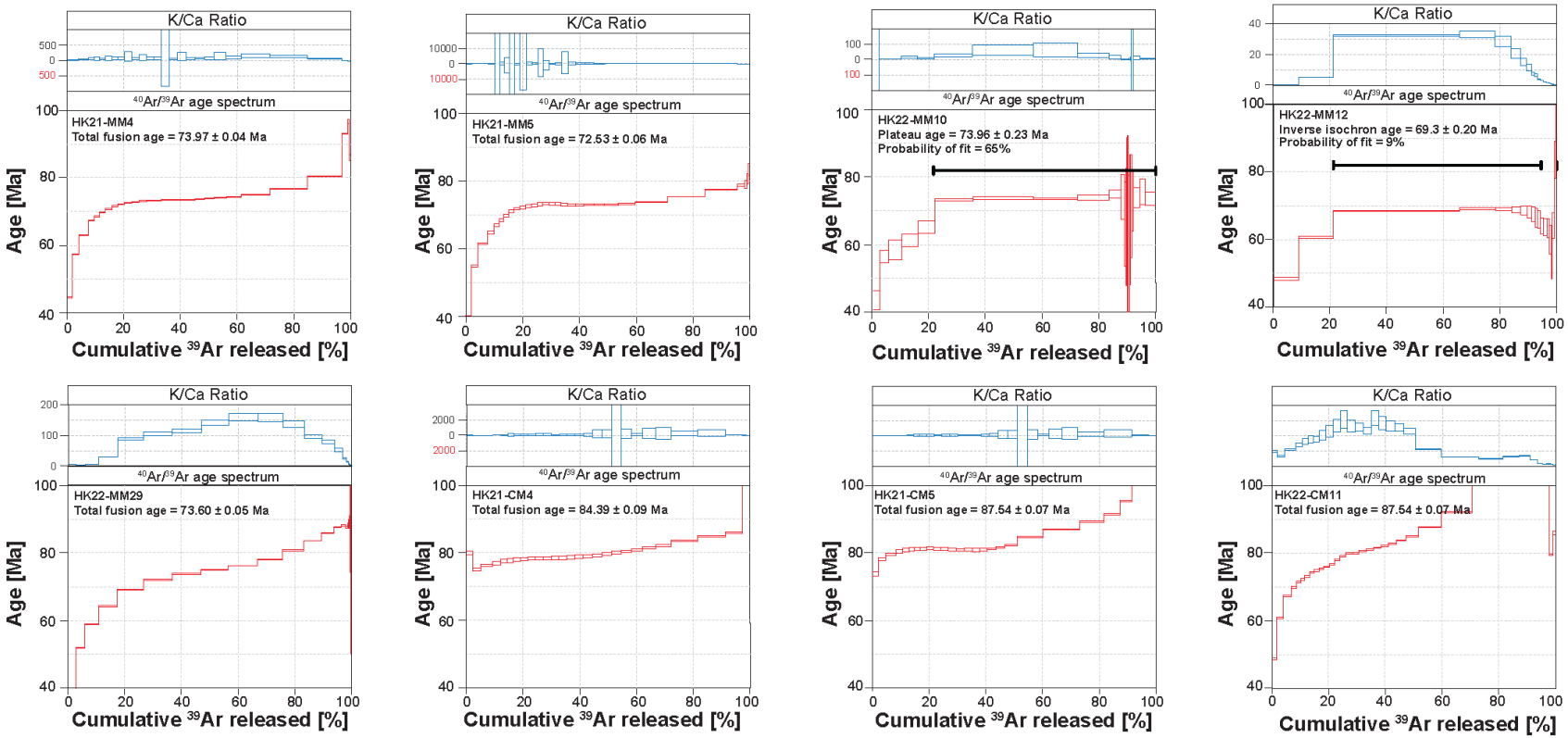

Figure 22. Age spectra for all muscovite separates

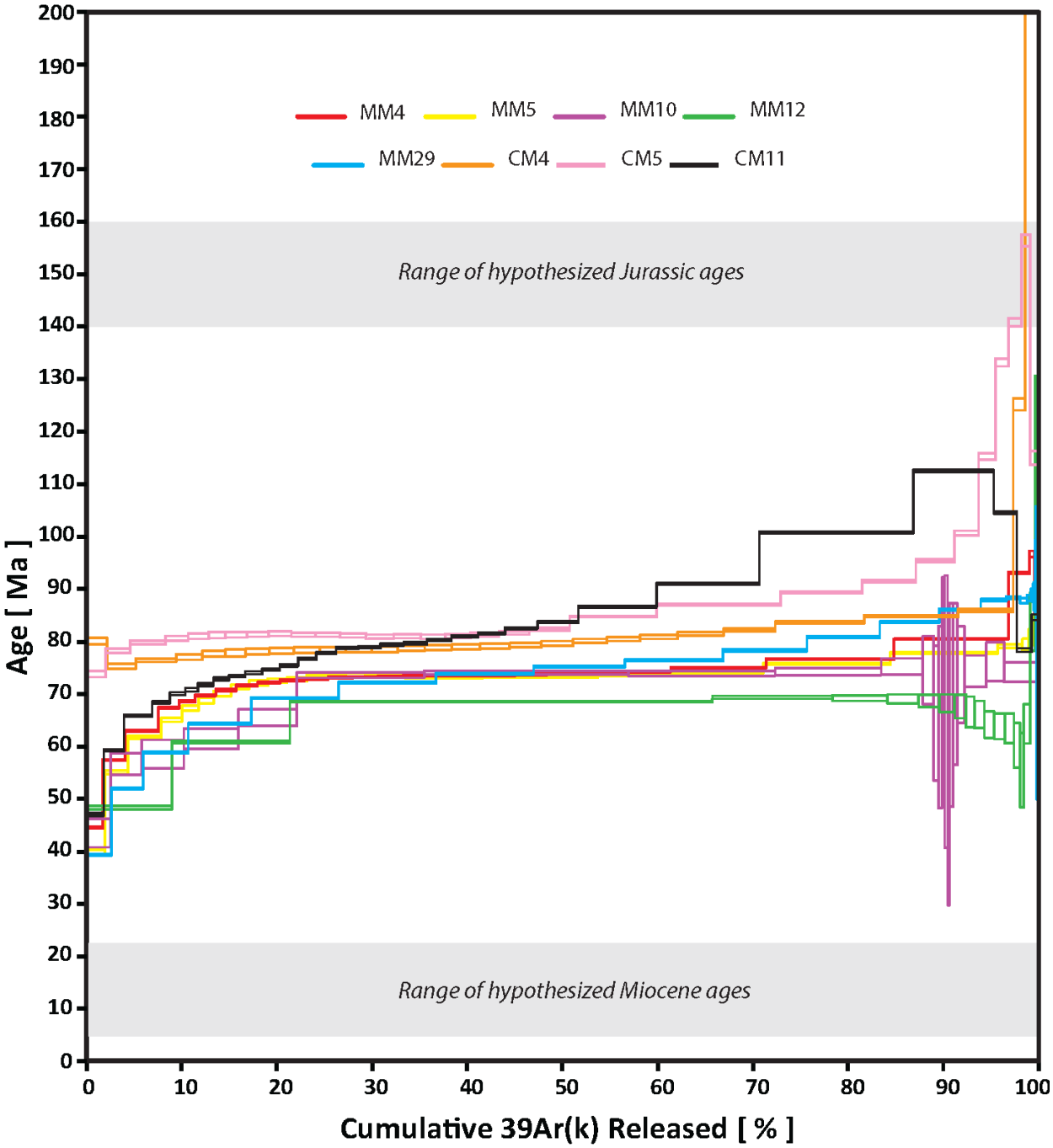

Figure 23. Out-of-sequence thrust system

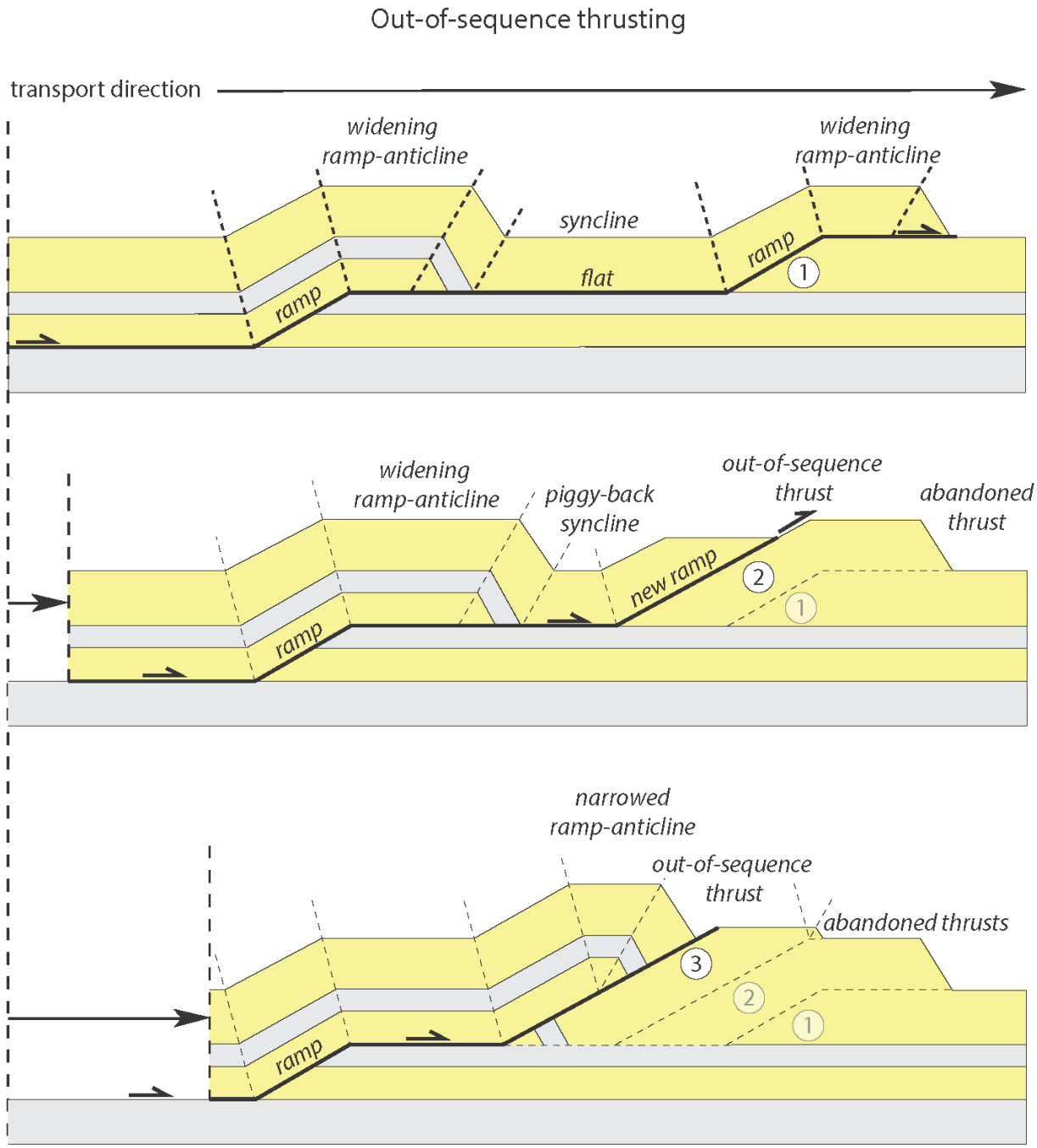

Figure 24. Normal sequence of a propagating thrust system

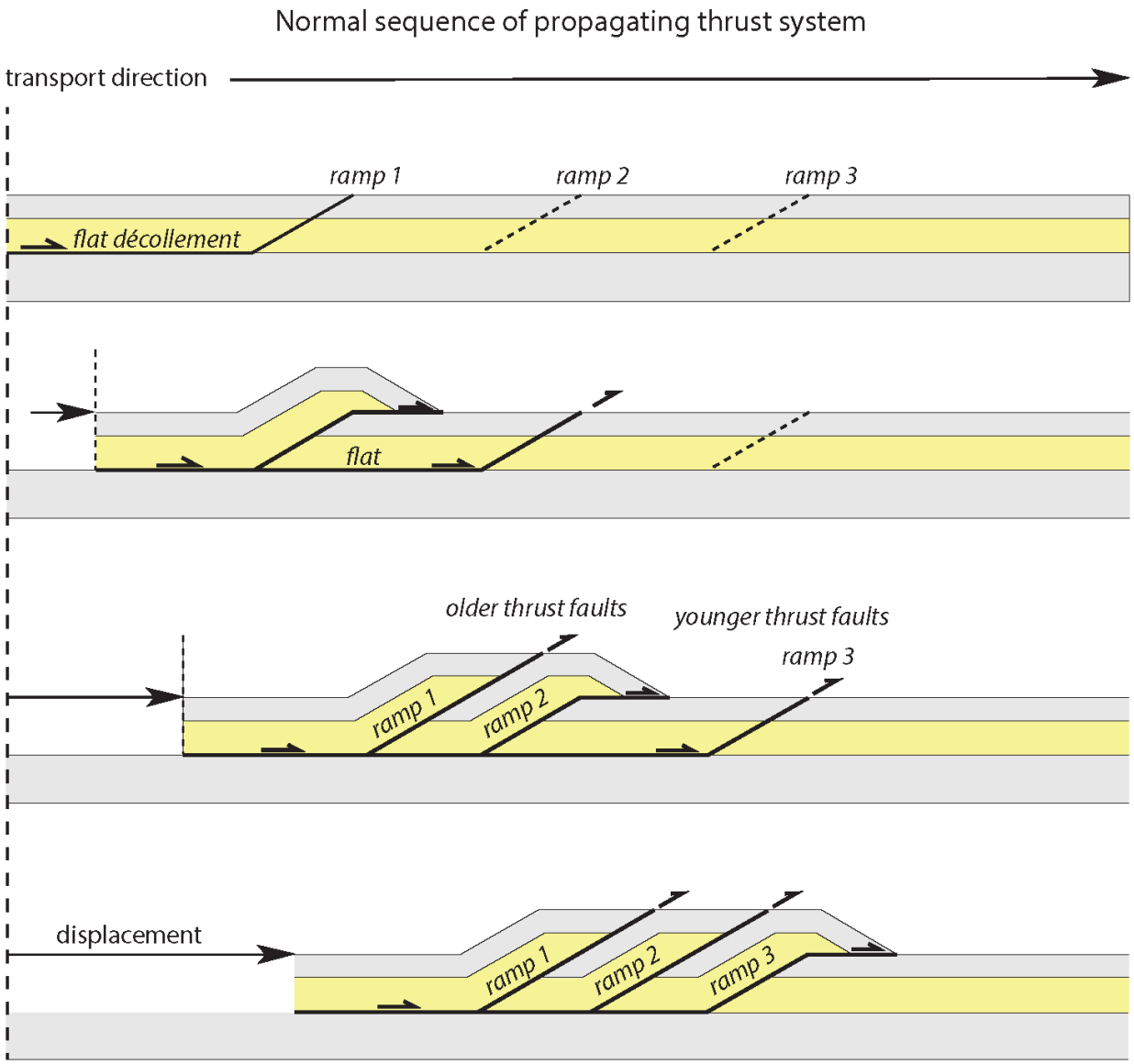

Appendix B: Muscovite $^{40}Ar/^{39}Ar$ Geochronology Data Tables

ID HK21-MM5	Temp (°C)	36Ar (mV)	37Ar (mV)	38Ar (mV)	39Ar (mV)	40Ar (mV)	40/39	Age (Ma)	± 2σ (Ma)	40Ar (%)	39Ar (%)	K/Ca
1	550	0.11	0.03	0.09	5.68	107.22	12.92	39.77	0.45	68.45	1.90	84.99
2	600	0.04	0.09	0.10	7.27	143.13	17.95	55.01	0.35	91.12	2.43	33.59
3	640	0.04	0.08	0.14	10.37	219.56	20.17	61.71	0.25	95.23	3.47	58.53
4	650	0.02	0.02	0.08	6.48	142.39	21.28	65.05	0.39	96.86	2.17	138.61
5	660	0.01	0.00	0.07	5.45	122.93	22.00	67.22	0.46	97.58	1.82	-2022.63
6	670	0.00	0.01	0.06	4.58	104.23	22.49	68.69	0.54	98.84	1.53	290.30
7	680	0.01	0.00	0.07	5.50	128.06	22.95	70.05	0.45	98.50	1.84	-717.95
8	690	0.01	0.00	0.07	5.65	133.74	23.36	71.30	0.44	98.66	1.89	3028.78
9	700	0.01	-0.02	0.07	5.82	139.06	23.62	72.06	0.43	98.81	1.95	-137.20
10	710	0.01	0.00	0.08	6.08	146.32	23.77	72.52	0.41	98.83	2.03	1463.96
11	720	0.01	0.01	0.08	6.28	151.60	23.86	72.79	0.40	98.92	2.10	335.30
12	730	0.00	0.01	0.07	6.11	147.88	23.97	73.12	0.41	99.05	2.04	201.30
13	740	0.00	0.00	0.07	5.98	145.25	24.05	73.35	0.42	99.02	2.00	1037.02
14	750	0.00	0.00	0.08	6.30	153.33	24.12	73.57	0.40	99.12	2.11	-585.64
15	760	0.00	0.01	0.08	6.10	148.14	24.06	73.38	0.41	99.09	2.04	190.22
16	770	0.00	0.01	0.08	6.59	160.19	24.08	73.43	0.38	99.10	2.21	261.95
17	780	0.01	0.00	0.09	7.00	169.89	24.02	73.27	0.36	99.04	2.34	962.13
18	790	0.01	0.01	0.09	7.95	192.71	24.00	73.21	0.32	99.08	2.66	426.56
19	800	0.01	0.01	0.11	9.03	218.84	24.00	73.19	0.29	99.07	3.02	308.79
20	810	0.01	0.02	0.13	10.35	250.94	24.02	73.26	0.25	99.10	3.46	255.11
21	820	0.01	0.02	0.14	11.47	277.69	24.00	73.22	0.23	99.12	3.84	239.79
22	830	0.01	0.04	0.18	14.46	349.78	24.00	73.20	0.20	99.21	4.84	149.09
23	850	0.01	0.05	0.22	18.03	437.90	24.10	73.50	0.17	99.24	6.03	145.21
24	890	0.02	0.11	0.42	33.95	830.73	24.32	74.15	0.12	99.38	11.36	130.96
25	930	0.02	0.15	0.49	39.95	998.10	24.83	75.69	0.11	99.40	13.36	113.83
26	1000	0.02	0.33	0.42	33.68	866.08	25.54	77.80	0.12	99.31	11.26	43.34
27	1070	0.01	0.35	0.10	7.72	203.00	25.98	79.12	0.33	98.78	2.58	9.36
28	1140	0.00	0.31	0.03	2.15	57.10	26.07	79.38	1.14	98.08	0.72	2.95
29	1230	0.00	0.42	0.02	1.60	43.16	26.57	80.86	1.53	98.22	0.53	1.65
30	1400	0.00	0.42	0.02	1.38	38.92	27.54	83.75	1.78	97.56	0.46	1.41

ID HK21-MM4	Temp (°C)	36Ar (mV)	37Ar (mV)	38Ar (mV)	39Ar (mV)	40Ar (mV)	40/39	Age (Ma)	± 2σ (Ma)	40Ar (%)	39Ar (%)	K/Ca
1	550	0.07	0.04	0.06	3.40	70.58	14.44	44.57	0.19	69.58	1.68	33.77
2	600	0.03	0.09	0.07	4.78	97.74	18.64	57.34	0.13	91.21	2.37	23.67

3	640	0.02	0.06	0.09	6.97	150.20	20.50	62.95	0.12	95.11	3.45	52.71
4	660	0.01	0.03	0.05	4.39	99.00	21.95	67.34	0.15	97.43	2.17	74.16
5	670	0.00	0.02	0.04	3.55	80.13	22.37	68.61	0.19	98.98	1.75	71.64
6	680	0.01	0.04	0.05	4.22	97.53	22.75	69.73	0.16	98.33	2.09	51.34
7	690	0.01	0.02	0.05	4.39	102.82	23.07	70.70	0.17	98.54	2.17	86.07
8	700	0.00	0.02	0.06	4.58	108.40	23.36	71.56	0.15	98.75	2.27	84.03
9	710	0.00	0.03	0.06	4.81	114.53	23.54	72.13	0.14	98.86	2.38	78.47
10	720	0.01	0.02	0.06	4.99	119.75	23.69	72.56	0.15	98.62	2.47	140.39
11	730	0.01	0.03	0.06	5.17	124.46	23.76	72.77	0.14	98.78	2.56	70.06
12	740	0.01	0.02	0.06	5.21	126.09	23.87	73.10	0.14	98.69	2.58	113.74
13	750	0.00	0.03	0.07	5.36	129.43	23.90	73.20	0.14	98.90	2.65	86.28
14	760	0.00	0.03	0.07	5.35	129.46	23.93	73.30	0.15	98.85	2.64	85.13
15	770	0.01	0.01	0.07	5.63	136.34	23.97	73.40	0.14	98.89	2.78	414.97
16	780	0.01	0.04	0.07	5.77	139.80	23.98	73.45	0.14	98.91	2.85	65.77
17	790	0.01	0.02	0.07	6.05	146.53	23.97	73.40	0.13	98.91	2.99	138.78
18	800	0.01	0.04	0.08	6.39	155.07	24.00	73.50	0.12	98.91	3.16	72.75
19	810	0.01	0.04	0.09	6.80	165.71	24.08	73.72	0.12	98.86	3.37	82.06
20	820	0.01	0.04	0.09	7.05	171.79	24.11	73.83	0.12	99.00	3.49	86.21
21	830	0.01	0.02	0.11	8.61	210.11	24.18	74.03	0.12	99.08	4.26	163.18
22	850	0.01	0.04	0.13	10.51	257.32	24.24	74.23	0.11	99.02	5.20	108.64
23	890	0.01	0.05	0.25	20.37	502.94	24.49	74.98	0.10	99.18	10.07	171.64
24	930	0.02	0.08	0.34	27.14	686.24	25.05	76.64	0.10	99.07	13.43	143.72
25	1000	0.02	0.15	0.30	24.27	644.18	26.31	80.41	0.11	99.13	12.01	71.40
26	1070	0.01	0.18	0.06	4.50	139.58	30.54	93.03	0.18	98.48	2.23	10.49
27	1140	0.00	0.24	0.01	0.99	32.06	31.75	96.61	0.62	97.53	0.49	1.77
28	1230	0.00	0.41	0.01	0.63	18.31	28.17	85.97	0.86	96.48	0.31	0.66
29	1400	0.00	0.57	0.00	0.30	9.84	31.54	95.99	1.91	96.49	0.15	0.23

ID HK22-MM10	**Temp** (°C)	**36Ar** (mV)	**37Ar** (mV)	**38Ar** (mV)	**39Ar** (mV)	**40Ar** (mV)	**40/39**	**Age** (Ma)	**± 2σ** (Ma)	**40Ar** (%)	**39Ar** (%)	**K/Ca**
1	550	0.01	0.00	0.01	0.31	7.21	14.06	43.42	2.70	60.39	2.50	321.41
2	600	0.02	0.05	0.01	0.40	14.02	18.39	56.59	2.10	52.69	3.24	3.57
3	640	0.25	0.05	0.06	0.56	84.69	19.03	58.51	2.71	12.52	4.49	5.22
4	680	0.21	0.02	0.05	0.71	75.74	19.99	61.43	1.95	18.66	5.70	17.22
5	720	0.15	0.03	0.04	0.76	62.31	21.32	65.45	1.65	26.16	6.16	10.96
6	760	0.01	0.02	0.02	1.66	43.06	24.01	73.53	0.52	92.36	13.35	28.63
7	790	0.01	0.02	0.04	2.66	67.92	24.18	74.03	0.36	94.81	21.47	64.98
8	810	0.01	0.01	0.02	1.92	48.64	24.14	73.91	0.45	95.05	15.44	65.28
9	830	0.01	0.02	0.02	1.38	35.53	24.24	74.23	0.62	94.46	11.16	30.46
10	850	0.01	0.01	0.01	0.54	16.38	24.57	75.22	1.56	81.23	4.36	16.77
11	870	0.01	0.02	0.00	0.13	4.86	24.34	74.52	6.48	66.26	1.07	3.72
12	890	0.01	0.02	0.01	0.06	3.68	21.61	66.32	12.89	38.05	0.52	1.65

13	910	0.01	0.01	0.00	0.05	3.99	21.34	65.50	17.33	26.31	0.40	2.00
14	930	0.01	0.01	0.00	0.04	2.68	22.96	70.38	21.77	33.00	0.31	1.60
15	950	0.00	0.01	0.00	0.03	1.86	21.70	66.59	25.96	37.62	0.26	1.50
16	970	0.00	0.01	0.00	0.03	1.69	18.00	55.38	25.64	34.55	0.26	1.06
17	1000	0.00	0.01	0.00	0.04	2.41	22.11	67.81	19.42	40.74	0.36	3.53
18	1030	0.00	0.00	0.00	0.05	2.59	23.45	71.85	15.37	49.44	0.44	6.27
19	1060	0.00	0.00	0.00	0.09	3.58	24.05	73.64	9.21	61.85	0.74	56.02
20	1160	0.01	0.01	0.01	0.28	10.36	24.26	74.29	3.01	66.49	2.29	13.08
21	1230	0.01	0.02	0.01	0.23	8.13	24.88	76.13	3.71	70.14	1.85	6.54
22	1400	0.01	0.02	0.01	0.45	14.48	24.19	74.07	1.86	75.73	3.65	8.60

ID HK22-MM12	Temp (°C)	36Ar (mV)	37Ar (mV)	38Ar (mV)	39Ar (mV)	40Ar (mV)	40/39	Age (Ma)	± 2σ (Ma)	40Ar (%)	39Ar (%)	K/Ca
1.00	660.00	0.16	10.56	0.12	7.02	157.44	15.70	48.25	0.38	69.90	8.94	0.29
2.00	740.00	0.11	0.84	0.14	9.72	225.85	19.86	60.80	0.28	85.45	12.39	4.99
3.00	810.00	0.06	0.46	0.44	34.80	797.94	22.41	68.48	0.16	97.73	44.37	32.65
4.00	820.00	0.02	0.13	0.12	9.93	231.19	22.70	69.34	0.26	97.45	12.65	33.42
5.00	830.00	0.01	0.07	0.06	4.55	106.40	22.65	69.19	0.49	96.86	5.80	28.96
6.00	840.00	0.01	0.05	0.03	2.53	59.60	22.56	68.93	0.85	95.78	3.23	20.80
7.00	850.00	0.01	0.05	0.02	1.71	40.61	22.47	68.64	1.24	94.51	2.18	15.32
8.00	860.00	0.01	0.05	0.02	1.25	29.93	22.32	68.21	1.68	93.53	1.60	11.76
9.00	870.00	0.01	0.05	0.01	0.94	22.86	22.11	67.57	2.24	91.05	1.20	7.66
10.00	880.00	0.01	0.05	0.01	0.73	18.13	21.77	66.54	2.90	87.33	0.93	6.73
11.00	910.00	0.01	0.09	0.01	0.82	20.46	21.60	66.04	2.58	86.42	1.04	3.94
12.00	940.00	0.01	0.11	0.01	0.82	20.65	20.96	64.11	2.57	83.41	1.05	3.20
13.00	970.00	0.01	0.17	0.02	0.85	21.72	20.85	63.79	2.48	81.86	1.09	2.16
14.00	1000.00	0.01	0.19	0.01	0.75	18.77	20.72	63.39	2.82	82.97	0.96	1.71
15.00	1030.00	0.01	0.17	0.01	0.50	11.95	19.63	60.12	4.27	81.68	0.63	1.27
16.00	1060.00	0.01	0.17	0.00	0.30	7.20	18.08	55.45	7.09	75.21	0.38	0.76
17.00	1160.00	0.01	0.42	0.01	0.56	15.58	21.01	64.26	3.76	75.69	0.72	0.58
18.00	1230.00	0.02	0.37	0.01	0.38	15.17	27.54	83.79	5.55	68.66	0.48	0.44
19.00	1400.00	0.05	0.97	0.02	0.29	26.73	41.01	123.42	7.23	44.48	0.37	0.13

ID HK22-MM29	Temp (°C)	36Ar (mV)	37Ar (mV)	38Ar (mV)	39Ar (mV)	40Ar (mV)	40/39	Age (Ma)	± 2σ (Ma)	40Ar (%)	39Ar (%)	K/Ca
1	550	0.11	0.51	0.13	8.55	141.44	12.72	39.24	0.15	76.89	2.57	7.23
2	600	0.06	1.40	0.15	11.14	206.14	16.90	51.96	0.13	91.35	3.35	3.42
3	640	0.07	1.22	0.21	15.83	325.01	19.17	58.82	0.12	93.40	4.76	5.58
4	680	0.24	0.31	0.32	21.92	531.70	20.99	64.30	0.15	86.53	6.59	30.64

5	720	0.05	0.15	0.39	30.66	708.02	22.63	69.23	0.13	97.99	9.22	88.16
6	760	0.03	0.14	0.42	33.88	808.43	23.59	72.10	0.13	98.86	10.19	106.67
7	790	0.03	0.13	0.43	34.11	832.12	24.16	73.82	0.14	99.05	10.25	116.24
8	810	0.02	0.10	0.40	31.92	792.42	24.60	75.14	0.14	99.10	9.60	143.25
9	830	0.02	0.09	0.43	34.31	864.48	24.99	76.32	0.14	99.20	10.31	160.00
10	850	0.02	0.08	0.36	29.36	759.29	25.65	78.27	0.15	99.19	8.83	158.66
11	870	0.02	0.08	0.32	25.57	684.00	26.50	80.82	0.15	99.07	7.69	136.76
12	890	0.02	0.09	0.26	20.58	571.26	27.46	83.67	0.16	98.92	6.19	96.20
13	910	0.02	0.08	0.18	14.53	415.89	28.25	86.03	0.17	98.69	4.37	78.71
14	930	0.02	0.07	0.12	8.97	263.45	28.85	87.82	0.19	98.22	2.70	52.55
15	950	0.01	0.09	0.07	4.98	148.72	29.01	88.29	0.23	97.14	1.50	24.72
16	960	0.01	0.07	0.03	2.34	70.86	28.82	87.71	0.42	95.29	0.70	13.65
17	970	0.01	0.07	0.02	1.28	40.06	28.99	88.22	0.62	92.34	0.38	8.18
18	980	0.01	0.06	0.01	0.73	24.53	29.24	88.97	1.06	86.89	0.22	4.94
19	990	0.01	0.06	0.01	0.45	16.48	29.34	89.28	1.74	79.25	0.13	3.18
20	1000	0.01	0.04	0.01	0.29	11.35	29.11	88.59	2.63	74.94	0.09	2.91
21	1010	0.01	0.04	0.01	0.19	7.31	29.42	89.50	3.98	76.67	0.06	1.96
22	1020	0.00	0.04	0.00	0.14	5.06	30.88	93.85	5.52	83.17	0.04	1.55
23	1030	0.00	0.04	0.00	0.10	3.51	31.30	95.07	7.37	90.57	0.03	1.19
24	1040	0.00	0.03	0.00	0.08	2.82	31.74	96.40	9.28	90.52	0.02	1.23
25	1050	0.00	0.02	0.00	0.07	2.25	27.90	84.99	10.51	89.38	0.02	1.83
26	1060	0.00	0.02	0.00	0.06	1.75	23.74	72.56	11.92	85.57	0.02	1.57
27	1070	0.00	0.02	0.00	0.06	1.56	20.68	63.38	13.42	74.50	0.02	1.01
28	1100	0.00	0.04	0.00	0.08	2.61	23.01	70.38	10.17	66.20	0.02	0.85
29	1160	0.00	0.09	0.00	0.14	3.84	23.12	70.71	5.53	84.27	0.04	0.66
30	1230	0.00	0.14	0.01	0.19	5.56	25.49	77.81	4.03	86.99	0.06	0.57
31	1400	0.00	0.21	0.00	0.16	5.77	31.51	95.69	4.70	86.93	0.05	0.32

ID HK23-MM36	**Temp** (°C)	**36Ar** (mV)	**37Ar** (mV)	**38Ar** (mV)	**39Ar** (mV)	**40Ar** (mV)	**40/39**	**Age** (Ma)	**± 2σ** (Ma)	**40Ar** (%)	**39Ar** (%)	**K/Ca**
1	600	0.21	0.25	0.22	13.64	3710.90	267.34	0.68	0.00	98.30	3.56	23.87
2	610	0.02	0.03	0.04	2.80	473.87	166.98	0.46	0.00	98.60	0.73	36.23
3	620	0.02	0.03	0.04	2.32	442.80	188.12	0.51	0.00	98.77	0.61	36.26
4	630	0.02	0.02	0.03	2.19	451.64	204.41	0.55	0.00	98.93	0.57	39.44
5	640	0.02	0.02	0.03	2.21	484.78	217.55	0.58	0.00	98.99	0.58	59.00
6	650	0.02	0.02	0.03	2.31	534.45	229.69	0.60	0.00	99.10	0.60	44.18
7	660	0.02	0.01	0.03	2.36	574.15	240.89	0.63	0.00	99.14	0.62	74.73
8	670	0.01	0.02	0.03	2.11	534.23	251.40	0.65	0.00	99.28	0.55	40.92
9	680	0.02	0.02	0.04	2.69	708.06	261.21	0.67	0.00	99.23	0.70	58.12
10	690	0.02	0.02	0.04	2.75	747.84	270.06	0.69	0.00	99.35	0.72	71.89
11	700	0.02	0.03	0.04	2.89	813.61	280.00	0.71	0.00	99.36	0.75	48.84
12	710	0.02	0.01	0.04	3.00	869.96	288.58	0.73	0.00	99.39	0.78	97.07

13	720	0.02	0.02	0.04	3.12	932.16	297.45	0.75	0.00	99.42	0.81	63.25
14	730	0.02	0.02	0.05	3.28	1008.34	305.79	0.77	0.00	99.43	0.85	67.28
15	740	0.02	0.02	0.05	3.44	1097.16	316.69	0.79	0.00	99.39	0.90	70.36
16	750	0.02	0.03	0.05	3.76	1237.41	327.74	0.81	0.00	99.49	0.98	60.93
17	760	0.03	0.02	0.06	4.16	1421.67	340.20	0.83	0.00	99.44	1.08	110.24
18	770	0.03	0.03	0.06	4.55	1653.25	361.32	0.88	0.00	99.49	1.19	59.14
19	780	0.03	0.01	0.07	5.12	1985.41	386.50	0.92	0.00	99.59	1.33	158.11
20	790	0.03	0.02	0.08	5.53	2315.45	417.26	0.98	0.00	99.65	1.44	131.30
21	800	0.03	0.02	0.08	6.06	2715.19	446.24	1.03	0.00	99.66	1.58	144.29
22	810	0.03	0.02	0.09	6.58	3149.22	477.50	1.09	0.00	99.72	1.71	113.95
23	820	0.04	0.02	0.10	7.12	3610.84	505.85	1.13	0.00	99.71	1.86	191.53
24	830	0.04	0.03	0.12	8.86	4946.57	556.82	1.22	0.00	99.75	2.31	146.94
25	840	0.03	0.04	0.10	8.04	4511.38	560.27	1.22	0.00	99.79	2.10	88.45
26	850	0.03	0.02	0.10	7.58	4292.26	565.18	1.23	0.00	99.78	1.98	157.61
27	860	0.03	0.02	0.10	7.21	4106.85	567.89	1.24	0.00	99.76	1.88	125.23
28	870	0.03	0.03	0.10	7.10	4051.14	569.05	1.24	0.00	99.75	1.85	103.18
29	880	0.04	0.02	0.09	6.89	3916.40	567.16	1.23	0.00	99.73	1.80	121.53
30	890	0.04	0.03	0.09	6.66	3740.51	559.62	1.22	0.00	99.70	1.74	84.76
31	900	0.04	0.04	0.09	6.55	3599.25	547.75	1.20	0.00	99.67	1.71	74.50
32	910	0.05	0.05	0.09	6.46	3446.84	531.12	1.18	0.00	99.61	1.69	58.23
33	920	0.05	0.03	0.09	6.32	3222.81	507.76	1.14	0.00	99.58	1.65	98.76
34	930	0.05	0.03	0.09	6.32	3042.93	479.00	1.09	0.00	99.53	1.65	85.24
35	940	0.05	0.04	0.10	6.58	2969.23	448.77	1.04	0.00	99.48	1.72	77.94
36	950	0.05	0.03	0.10	6.76	2837.80	417.30	0.98	0.00	99.44	1.76	98.63
37	960	0.06	0.04	0.10	6.96	2718.45	388.15	0.93	0.00	99.38	1.81	71.06
38	970	0.06	0.04	0.11	7.34	2689.04	364.17	0.88	0.00	99.37	1.91	87.53
39	980	0.06	0.04	0.11	7.59	2653.00	347.32	0.85	0.00	99.36	1.98	83.07
40	990	0.06	0.04	0.11	7.69	2620.96	338.62	0.83	0.00	99.37	2.01	78.66
41	1000	0.05	0.03	0.11	7.88	2689.12	339.09	0.83	0.00	99.40	2.06	105.10
42	1010	0.05	0.04	0.11	8.14	2861.06	349.36	0.85	0.00	99.45	2.12	81.24
43	1020	0.05	0.04	0.11	8.22	3055.47	369.92	0.89	0.00	99.55	2.14	93.98
44	1030	0.04	0.03	0.11	8.30	3268.29	392.12	0.93	0.00	99.60	2.16	103.92
45	1040	0.04	0.05	0.11	8.43	3449.40	407.83	0.96	0.00	99.65	2.20	74.43
46	1050	0.04	0.03	0.11	8.00	3223.57	401.60	0.95	0.00	99.66	2.09	121.95
47	1060	0.03	0.04	0.10	7.13	2625.02	366.95	0.89	0.00	99.62	1.86	68.96
48	1070	0.03	0.05	0.09	6.47	2022.68	311.21	0.78	0.00	99.53	1.69	57.30
49	1100	0.05	0.07	0.13	9.45	2215.88	232.91	0.61	0.00	99.36	2.46	58.78
50	1160	0.13	0.16	0.38	28.00	4005.96	141.73	0.39	0.00	99.05	7.30	77.37
51	1230	0.27	0.21	0.83	61.42	7610.18	122.60	0.35	0.00	98.95	16.01	127.85
52	1400	0.11	0.04	0.12	7.21	2936.81	402.84	0.95	0.00	98.86	1.88	71.58

ID HK22-CM4	Temp (°C)	36Ar (mV)	37Ar (mV)	38Ar (mV)	39Ar (mV)	40Ar (mV)	40/39	Age (Ma)	± 2σ (Ma)	40Ar (%)	39Ar (%)	K/Ca
1	550	0.10	0.09	0.08	5.06	161.39	26.25	80.23	0.65	82.30	2.14	23.21
2	600	0.05	0.55	0.10	7.09	188.25	24.61	75.32	0.46	92.62	2.99	5.56
3	640	0.04	0.42	0.14	9.98	261.03	25.01	76.53	0.34	95.61	4.21	10.11
4	650	0.02	0.10	0.09	6.56	171.14	25.21	77.13	0.50	96.65	2.77	29.56
5	660	0.01	0.05	0.08	5.87	153.14	25.43	77.78	0.55	97.44	2.48	54.07
6	670	0.01	0.02	0.06	4.82	125.01	25.47	77.90	0.67	98.24	2.04	83.71
7	680	0.01	0.04	0.08	5.99	156.13	25.56	78.18	0.54	98.00	2.53	71.56
8	690	0.01	0.04	0.08	6.19	161.56	25.61	78.31	0.52	98.06	2.61	75.61
9	700	0.01	0.04	0.08	6.33	165.48	25.65	78.46	0.51	98.17	2.67	60.79
10	710	0.01	0.03	0.08	6.46	168.57	25.68	78.53	0.50	98.38	2.73	85.83
11	720	0.01	0.03	0.09	6.63	173.04	25.69	78.57	0.49	98.43	2.80	97.45
12	730	0.01	0.05	0.08	6.50	169.62	25.70	78.60	0.50	98.49	2.75	56.61
13	740	0.01	0.04	0.08	6.54	170.79	25.76	78.78	0.50	98.69	2.76	64.40
14	750	0.01	0.05	0.09	6.78	177.14	25.80	78.90	0.48	98.70	2.86	63.10
15	760	0.01	0.04	0.09	6.99	183.01	25.85	79.03	0.47	98.70	2.95	76.72
16	770	0.01	0.03	0.09	7.42	194.55	25.89	79.17	0.44	98.80	3.14	104.18
17	780	0.01	0.02	0.10	7.84	206.15	25.97	79.39	0.42	98.73	3.31	182.97
18	790	0.01	0.02	0.10	7.98	210.56	26.08	79.73	0.42	98.81	3.37	192.32
19	800	0.01	-0.01	0.10	8.37	221.96	26.22	80.15	0.40	98.86	3.53	-628.60
20	810	0.01	0.02	0.10	8.33	222.17	26.36	80.57	0.40	98.82	3.52	210.48
21	820	0.01	0.04	0.12	9.34	250.62	26.51	81.03	0.36	98.86	3.95	95.44
22	830	0.01	0.02	0.14	11.28	304.37	26.71	81.62	0.31	99.03	4.77	247.22
23	850	0.01	0.02	0.16	12.85	349.63	26.95	82.33	0.28	99.02	5.43	293.72
24	890	0.02	0.04	0.28	22.19	613.75	27.40	83.69	0.20	99.10	9.37	229.27
25	930	0.02	0.03	0.29	23.45	658.64	27.83	84.96	0.19	99.10	9.90	303.92
26	1000	0.02	0.09	0.17	13.72	393.05	28.18	86.00	0.27	98.36	5.79	64.98
27	1070	0.02	0.11	0.04	2.88	124.24	41.53	125.36	1.10	96.15	1.21	11.24
28	1140	0.01	0.16	0.02	1.38	129.35	91.42	265.45	2.30	97.23	0.58	3.61
29	1230	0.01	0.24	0.02	1.40	136.08	94.78	274.52	2.28	97.42	0.59	2.49
30	1400	0.02	0.13	0.01	0.57	92.01	149.67	416.48	5.78	93.02	0.24	1.90

ID HK22-CM5	Temp (°C)	36Ar (mV)	37Ar (mV)	38Ar (mV)	39Ar (mV)	40Ar (mV)	40/39	Age (Ma)	± 2σ (Ma)	40Ar (%)	39Ar (%)	K/Ca
1	550	0.08	0.20	0.08	4.65	136.94	24.10	73.79	0.57	81.86	1.93	9.97
2	600	0.03	0.40	0.09	6.32	171.08	25.57	78.19	0.42	94.45	2.62	6.82
3	640	0.08	0.35	0.13	9.01	258.76	26.10	79.76	0.31	90.87	3.73	11.07
4	650	0.06	0.17	0.09	5.73	169.56	26.35	80.51	0.46	89.08	2.37	14.11
5	660	0.05	0.13	0.08	5.15	151.36	26.51	80.99	0.50	90.16	2.13	16.40

6	670	0.03	0.10	0.06	4.30	124.61	26.56	81.16	0.60	91.67	1.78	18.03
7	680	0.04	0.13	0.07	5.37	154.82	26.60	81.28	0.48	92.29	2.22	17.70
8	690	0.03	0.12	0.07	5.62	158.85	26.62	81.33	0.46	94.26	2.33	20.46
9	700	0.02	0.11	0.07	5.77	158.41	26.66	81.43	0.45	97.16	2.39	23.10
10	710	0.01	0.10	0.08	6.05	164.82	26.60	81.26	0.43	97.62	2.51	26.58
11	720	0.01	0.09	0.08	6.32	172.19	26.61	81.29	0.41	97.70	2.62	30.63
12	730	0.01	0.11	0.08	6.57	178.15	26.54	81.08	0.40	97.81	2.72	26.43
13	740	0.01	0.12	0.09	6.94	187.55	26.47	80.89	0.38	97.91	2.87	25.68
14	750	0.01	0.13	0.09	6.88	186.26	26.50	80.96	0.38	97.90	2.85	23.38
15	760	0.01	0.09	0.08	6.29	169.75	26.47	80.88	0.42	98.12	2.61	31.79
16	770	0.01	0.10	0.08	6.44	173.37	26.52	81.01	0.41	98.43	2.67	28.37
17	780	0.01	0.12	0.09	7.18	193.69	26.60	81.26	0.37	98.62	2.98	26.42
18	790	0.01	0.13	0.09	7.69	208.05	26.72	81.62	0.35	98.78	3.19	25.69
19	800	0.01	0.19	0.12	10.16	277.05	26.98	82.39	0.27	98.88	4.21	23.17
20	810	0.02	0.84	0.28	22.01	616.42	27.77	84.77	0.16	99.17	9.12	11.26
21	820	0.02	2.10	0.39	31.58	907.47	28.52	87.01	0.14	99.27	13.08	6.48
22	830	0.02	1.72	0.26	20.63	609.82	29.30	89.33	0.17	99.15	8.55	5.15
23	850	0.02	0.89	0.17	13.55	411.66	30.01	91.44	0.22	98.81	5.61	6.55
24	890	0.02	0.59	0.13	9.94	315.99	31.34	95.38	0.28	98.60	4.12	7.27
25	930	0.01	0.58	0.08	6.12	206.33	33.11	100.63	0.43	98.27	2.54	4.51
26	1000	0.01	0.81	0.05	4.15	161.84	38.08	115.27	0.63	97.68	1.72	2.20
27	1070	0.01	0.97	0.04	3.31	149.85	44.22	133.16	0.78	97.60	1.37	1.47
28	1140	0.01	0.78	0.04	3.31	158.41	46.86	140.83	0.78	97.97	1.37	1.82
29	1230	0.01	0.71	0.03	2.27	122.29	52.27	156.42	1.15	97.01	0.94	1.38
30	1400	0.04	0.81	0.03	2.06	90.06	37.96	114.92	1.25	86.93	0.85	1.09

ID HK22-CM11	**Temp** (°C)	**36Ar** (mV)	**37Ar** (mV)	**38Ar** (mV)	**39Ar** (mV)	**40Ar** (mV)	**40/39**	**Age** (Ma)	**± 2σ** (Ma)	**40Ar** (%)	**39Ar** (%)	**K/Ca**
1	550	0.13	0.41	0.10	6.24	136.20	15.80	48.65	0.26	72.37	1.77	6.58
2	600	0.05	1.48	0.11	7.75	168.77	19.80	60.79	0.20	90.97	2.20	2.25
3	640	0.06	1.54	0.14	10.27	241.77	21.95	67.26	0.17	93.23	2.91	2.86
4	650	0.03	0.31	0.09	6.59	159.38	22.77	69.73	0.23	94.14	1.87	9.03
5	660	0.05	0.16	0.08	5.76	148.85	23.31	71.33	0.26	90.14	1.63	15.91
6	670	0.07	0.09	0.07	4.67	131.84	23.58	72.14	0.32	83.49	1.33	21.77
7	680	0.09	0.07	0.09	5.75	163.85	23.88	73.05	0.28	83.86	1.63	33.70
8	690	0.05	0.06	0.08	5.68	153.56	24.26	74.19	0.27	89.69	1.61	41.66
9	700	0.02	0.06	0.07	5.94	150.89	24.44	74.72	0.25	96.26	1.69	43.31
10	710	0.02	0.07	0.08	6.25	158.48	24.63	75.29	0.24	97.16	1.77	40.71
11	720	0.02	0.07	0.09	6.62	169.06	24.83	75.89	0.23	97.27	1.88	41.05
12	730	0.02	0.07	0.08	6.60	170.27	25.08	76.66	0.23	97.30	1.87	40.79
13	740	0.02	0.09	0.08	6.92	181.55	25.53	77.99	0.23	97.29	1.96	33.87
14	750	0.02	0.06	0.09	7.33	195.12	25.87	79.00	0.22	97.17	2.08	48.53

15	760	0.02	0.04	0.10	8.16	219.68	26.20	79.99	0.21	97.29	2.32	96.42
16	770	0.02	0.05	0.10	8.24	221.93	26.21	80.03	0.20	97.31	2.34	69.66
17	780	0.02	0.03	0.10	8.44	227.99	26.39	80.57	0.20	97.67	2.39	104.39
18	790	0.02	0.08	0.11	8.81	239.03	26.50	80.91	0.20	97.70	2.50	47.27
19	800	0.02	0.04	0.11	9.07	247.75	26.70	81.48	0.20	97.77	2.57	95.80
20	810	0.02	0.06	0.13	9.90	272.26	26.92	82.14	0.19	97.85	2.81	71.15
21	820	0.02	0.05	0.12	9.72	269.24	27.10	82.67	0.19	97.83	2.76	85.00
22	830	0.02	0.04	0.15	12.17	339.79	27.43	83.67	0.18	98.26	3.45	117.35
23	850	0.02	0.07	0.19	15.03	425.17	27.83	84.86	0.16	98.40	4.27	92.88
24	890	0.04	0.13	0.36	28.97	845.35	28.78	87.68	0.15	98.62	8.22	93.64
25	930	0.05	0.15	0.48	38.04	1164.97	30.24	92.03	0.15	98.75	10.79	105.95
26	1000	0.08	0.22	0.71	57.01	1933.08	33.49	101.66	0.16	98.78	16.18	109.64
27	1070	0.07	0.27	0.38	29.63	1131.38	37.43	113.24	0.19	98.03	8.41	47.60
28	1140	0.02	0.16	0.11	8.79	312.72	34.77	105.44	0.23	97.71	2.49	23.59
29	1230	0.03	0.09	0.07	5.47	150.37	26.04	79.53	0.28	94.77	1.55	25.60
30	1400	0.04	0.23	0.04	2.55	85.22	28.14	85.79	0.54	84.33	0.72	4.84

Appendix C: EDS Elemental Spectra

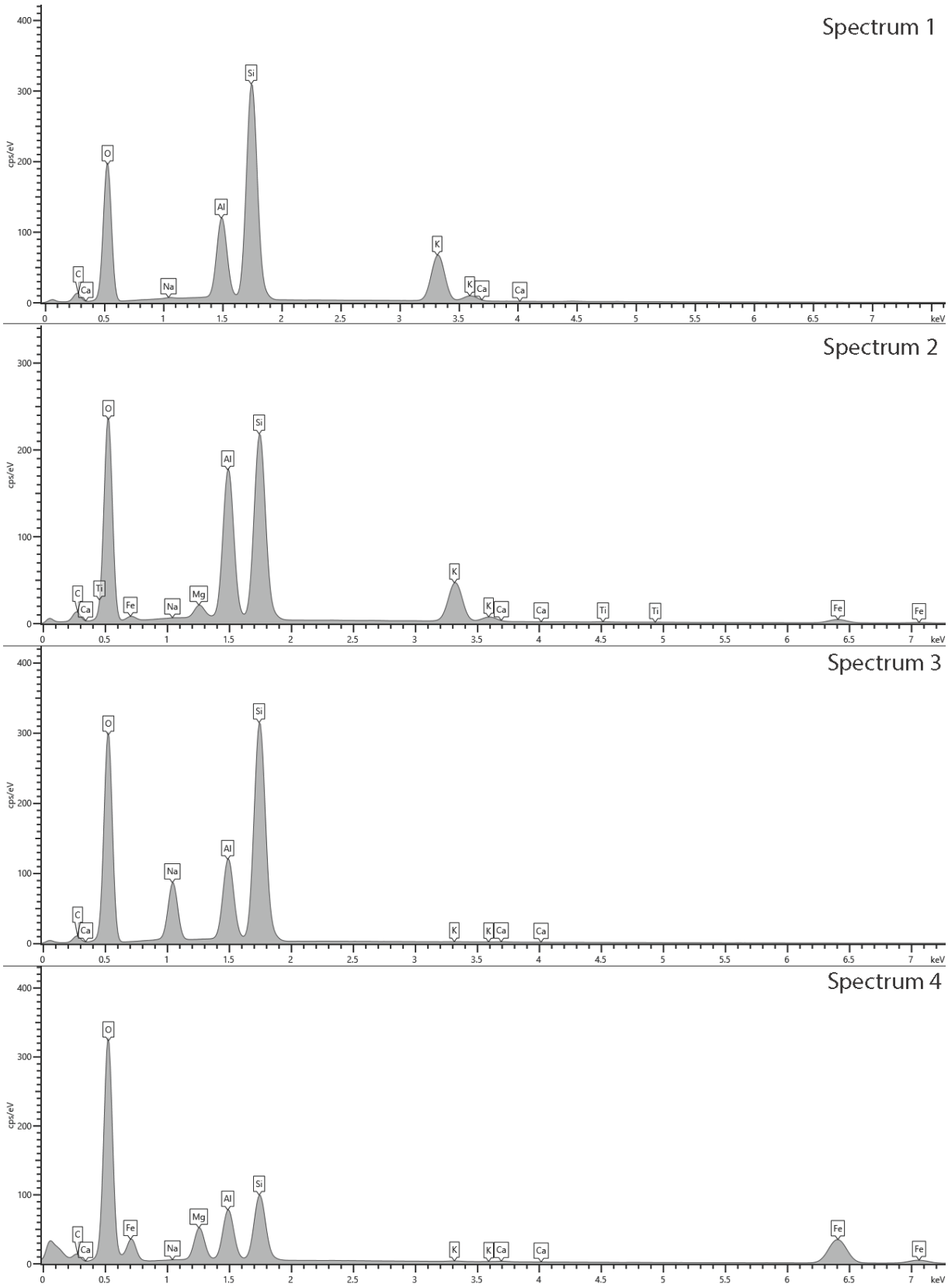

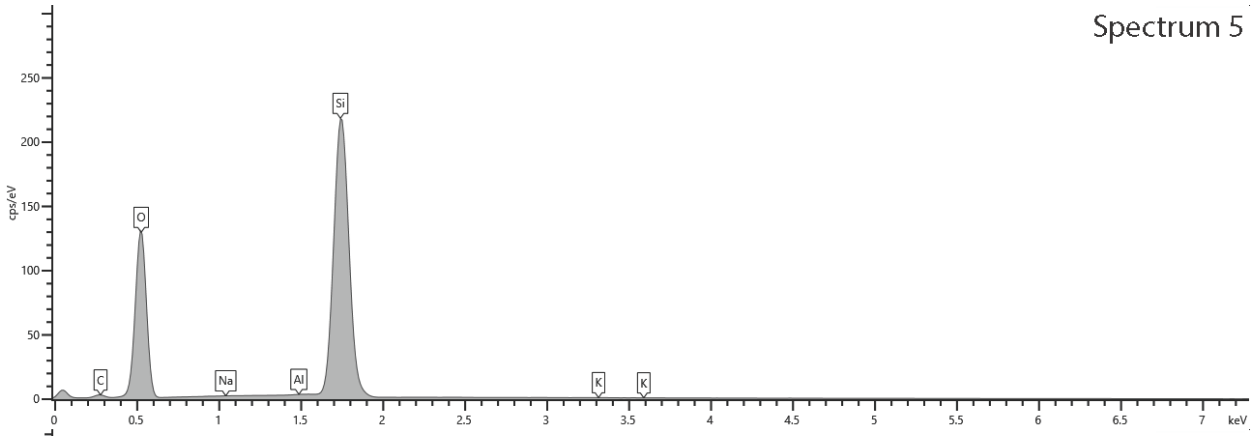
Spectrum 5
cps/eV
keV
C
O
Na
Al
Si
K
K

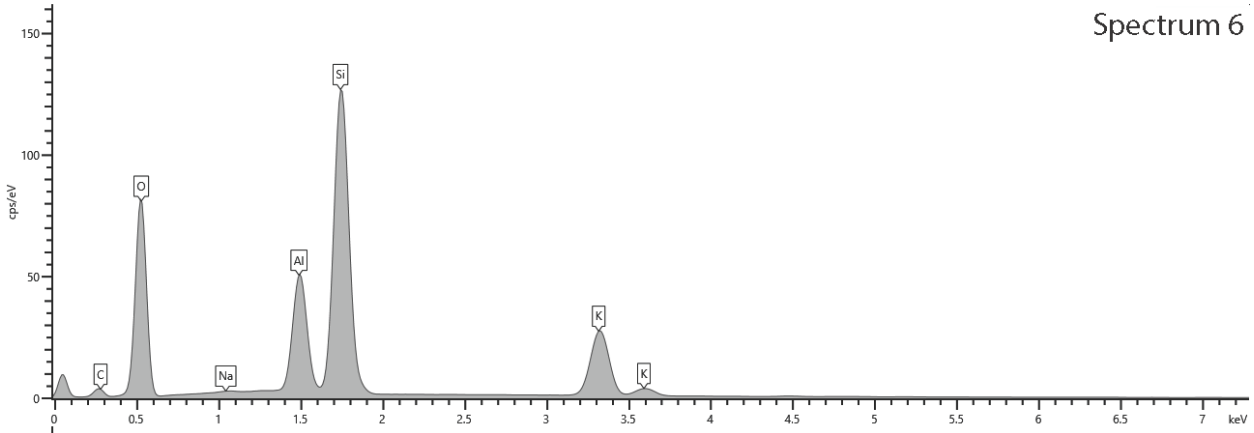
Spectrum 6
cps/eV
keV
C
O
Na
Al
Si
K
K

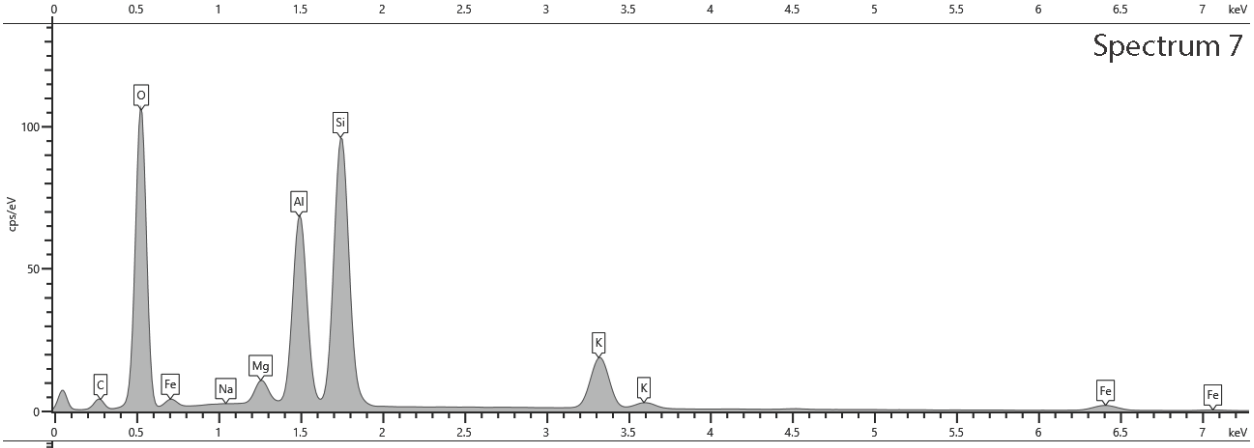
Spectrum 7
cps/eV
keV
C
O
Fe
Na
Mg
Al
Si
K
K
Fe
Fe

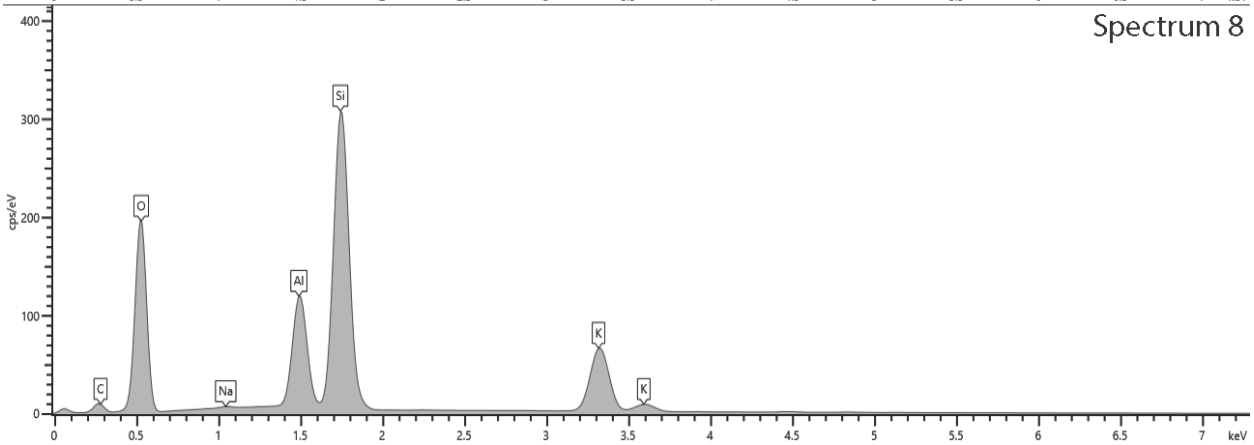
Spectrum 8
cps/eV
keV
C
O
Na
Al
Si
K
K

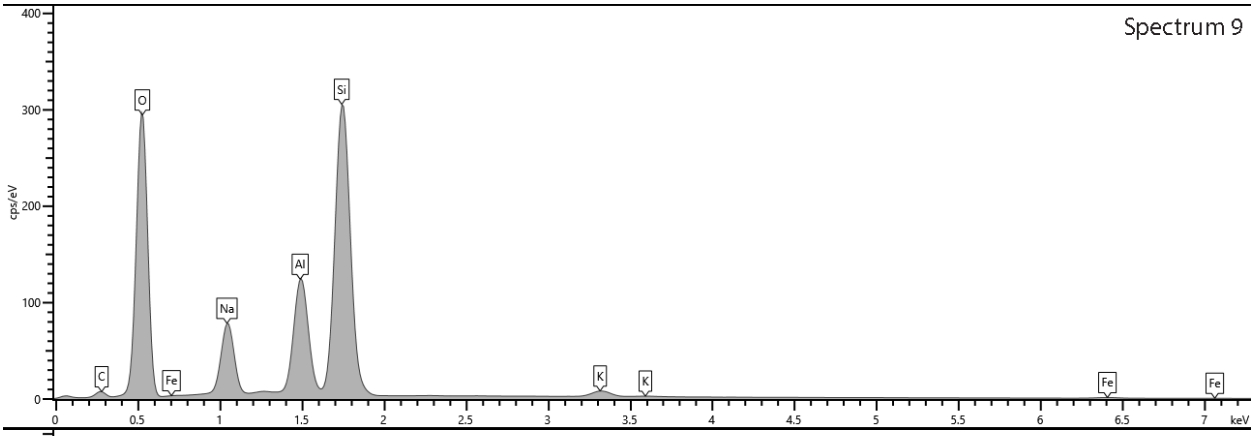
Spectrum 9
cps/eV
keV
C
O
Fe
Na
Al
Si
K
K
Fe
Fe

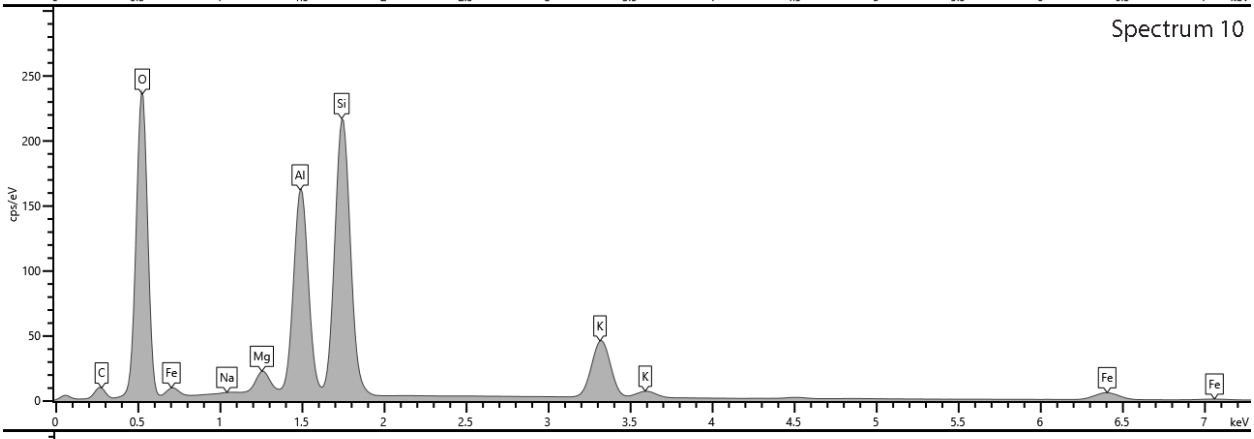
Spectrum 10
cps/eV
keV
C
O
Fe
Na
Mg
Al
Si
K
K
Fe
Fe

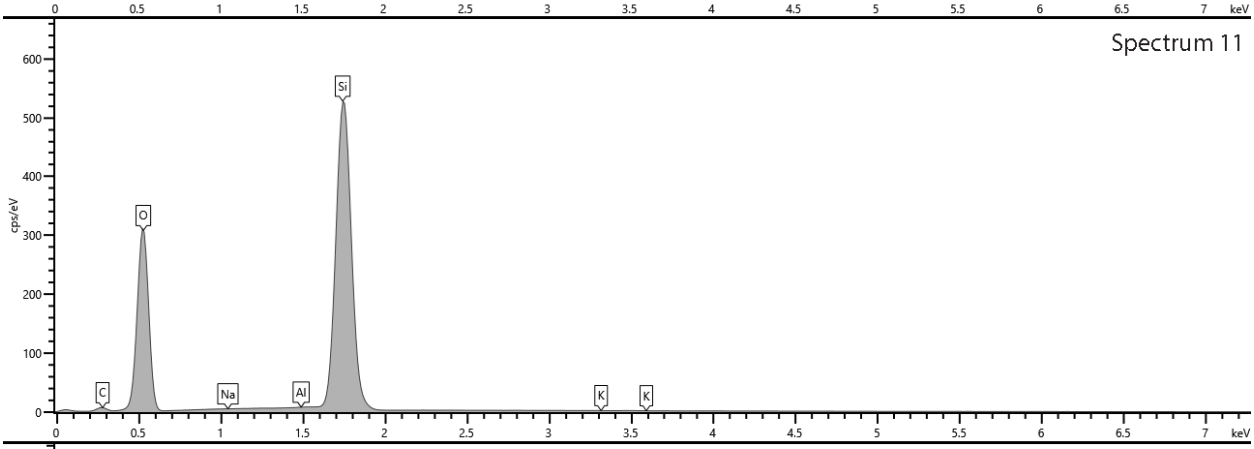
Spectrum 11
cps/eV
keV
C
O
Na
Al
Si
K
K

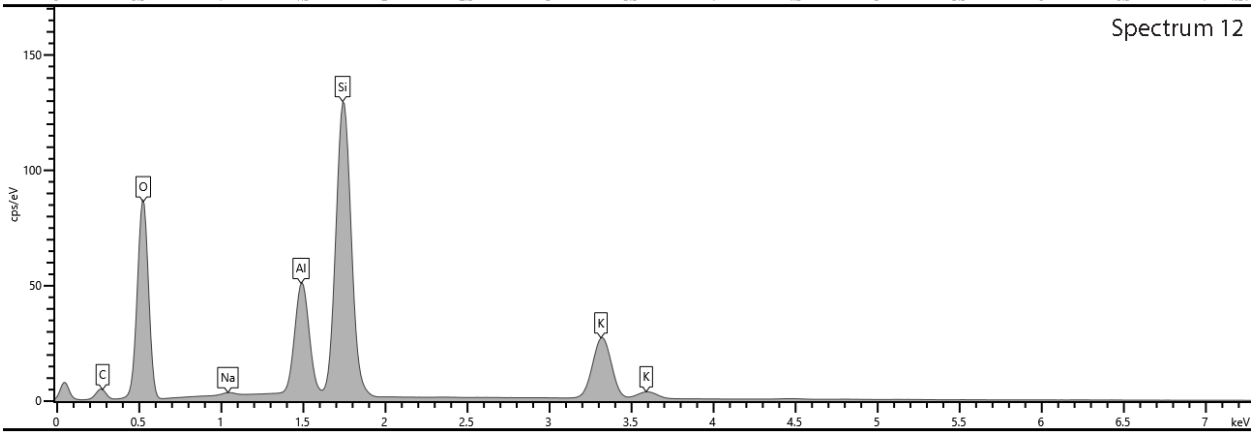
Spectrum 12
cps/eV
keV
C
O
Na
Al
Si
K
K

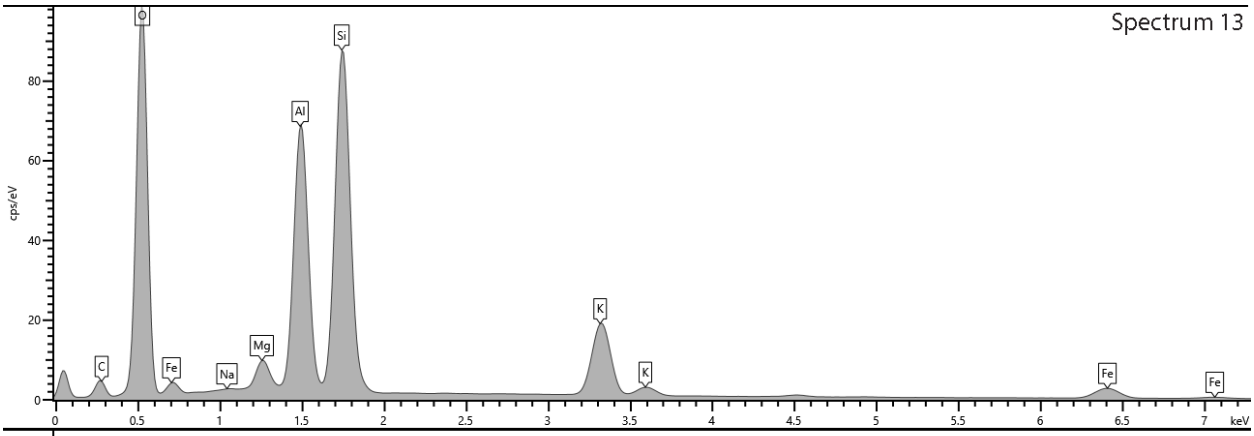
Spectrum 13
cps/eV
keV
O
Si
Al
K
C
Fe
Na
Mg
K
Fe
Fe

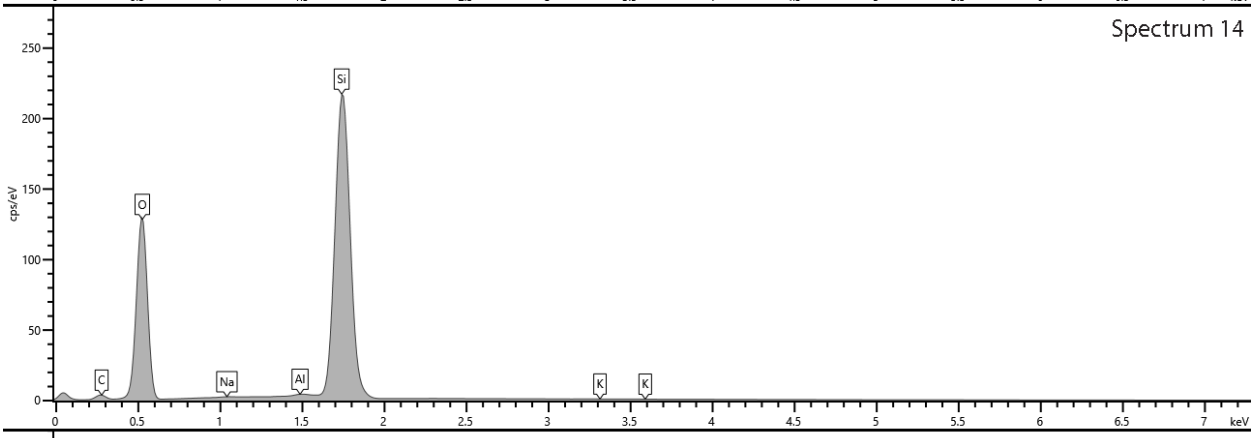
Spectrum 14
cps/eV
keV
Si
O
C
Na
Al
K
K

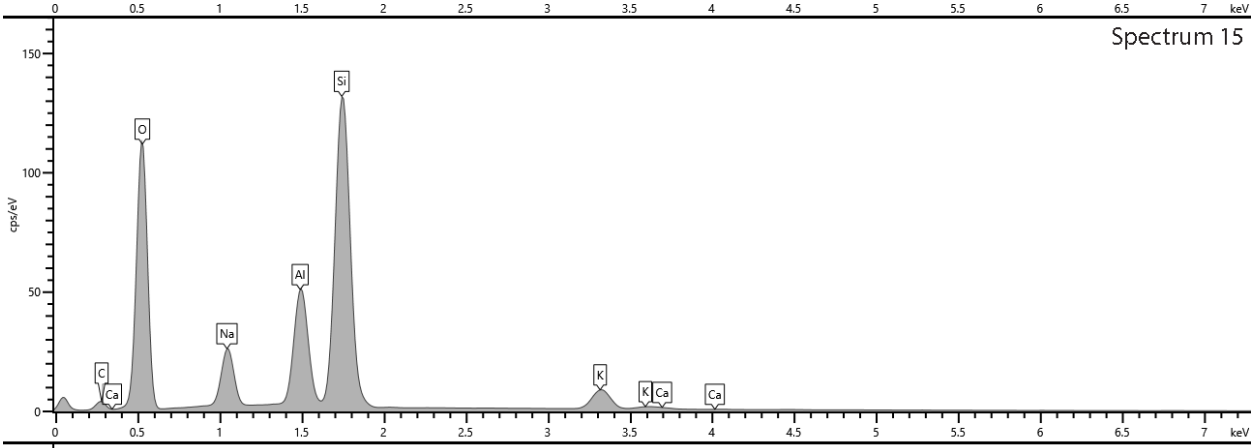
Spectrum 15
cps/eV
keV
Si
O
Al
Na
C
Ca
K
K
Ca
Ca

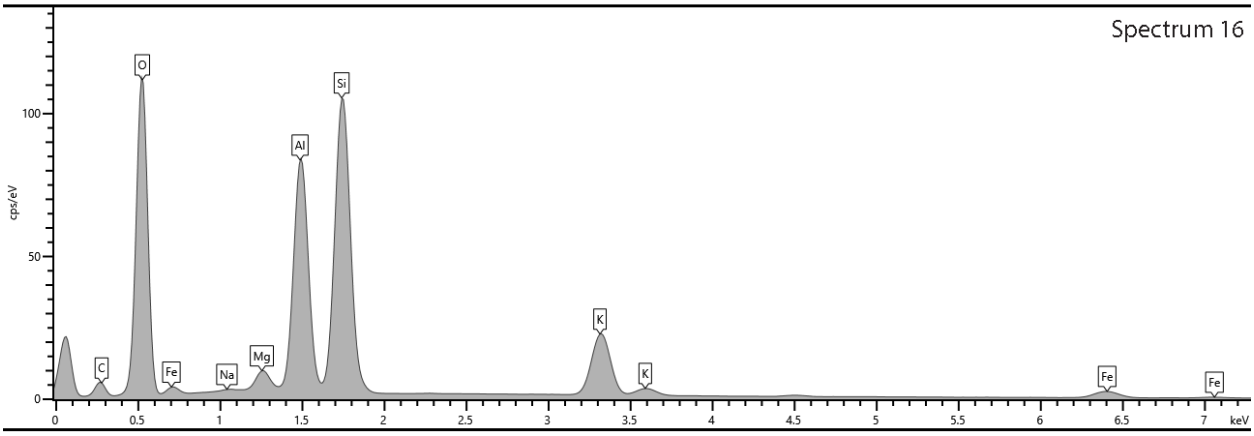
Spectrum 16
cps/eV
keV
O
Si
Al
K
C
Fe
Na
Mg
K
Fe
Fe

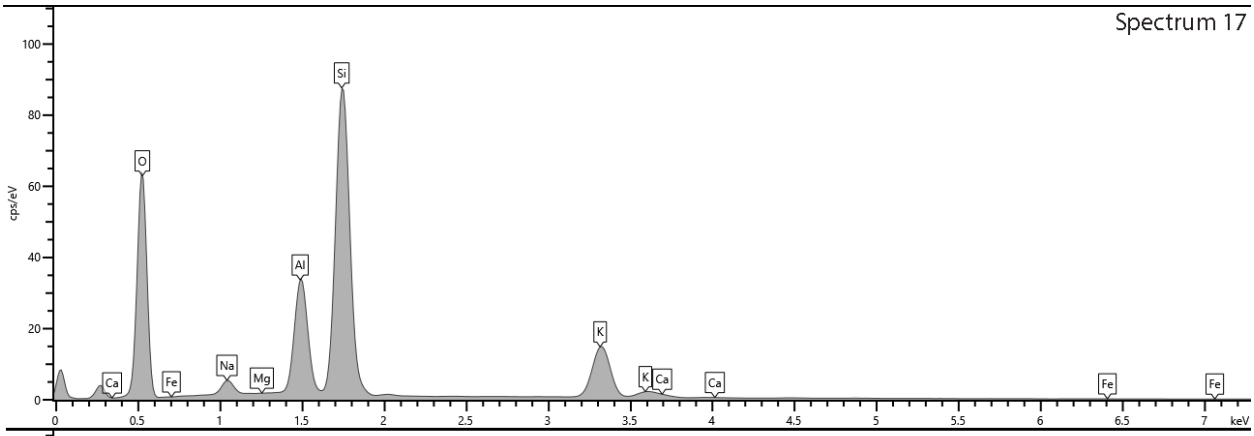
Spectrum 17
cps/eV
keV
O
Si
Al
K
Na
Mg
Ca
Fe

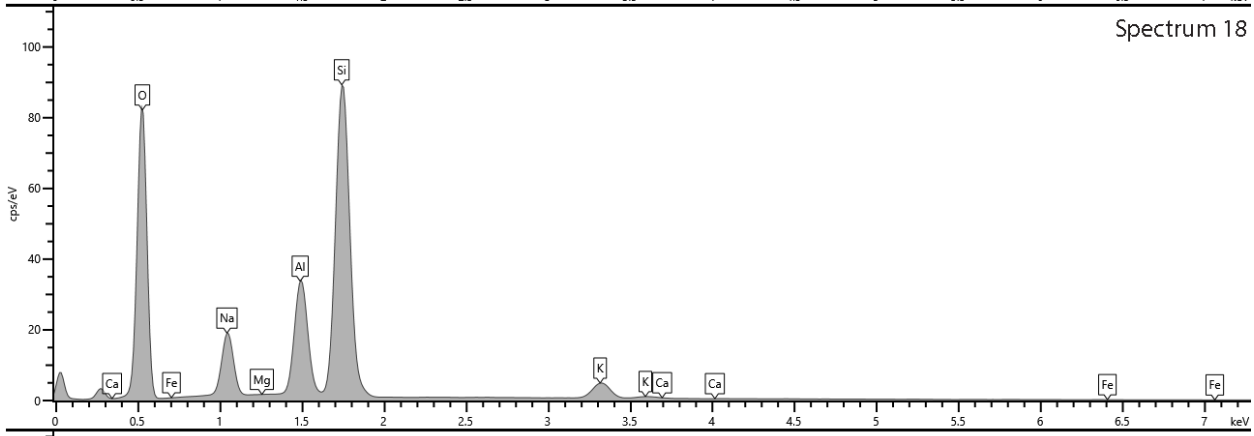
Spectrum 18
cps/eV
keV
O
Si
Al
Na
K
Mg
Ca
Fe

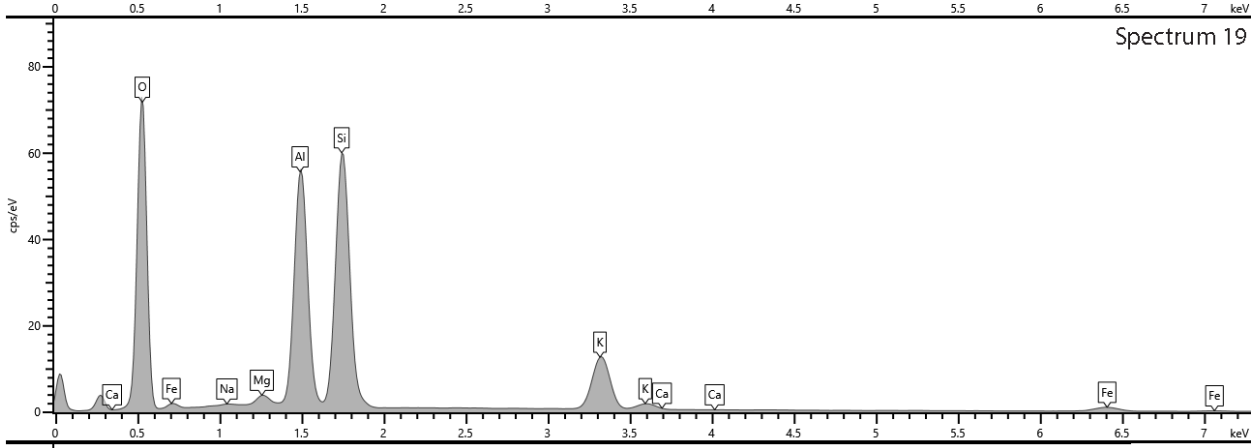
Spectrum 19
cps/eV
keV
O
Al
Si
K
Mg
Na
Ca
Fe

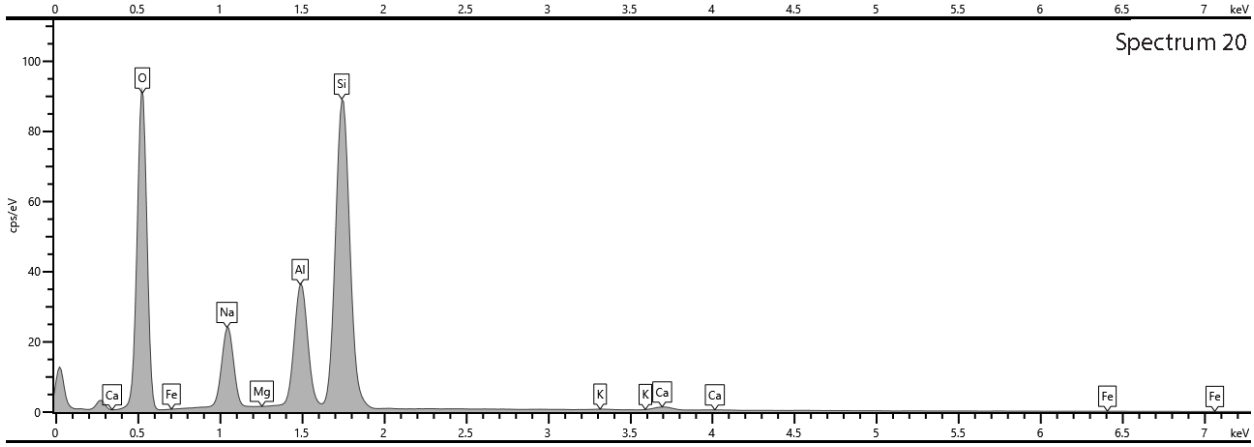
Spectrum 20
cps/eV
keV
O
Si
Al
Na
Mg
K
Ca
Fe

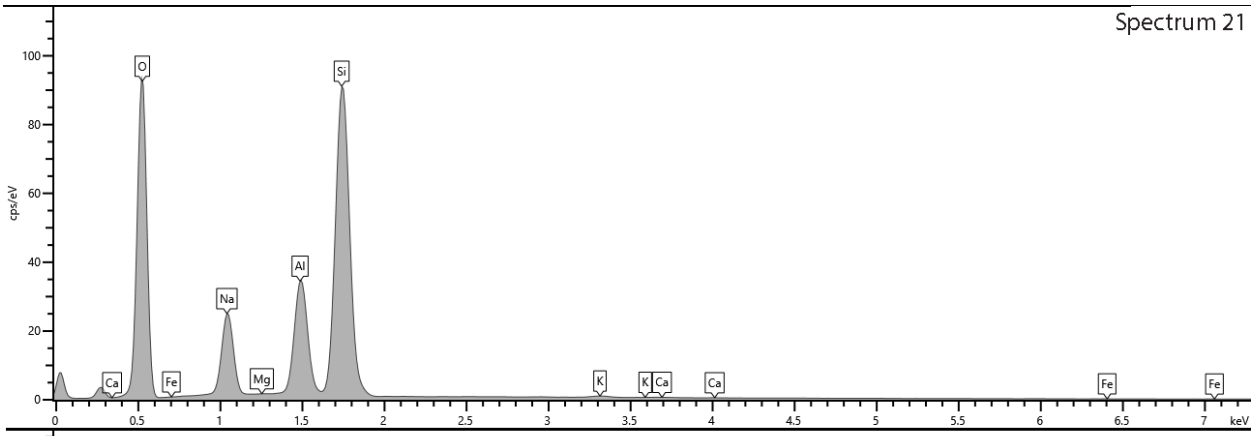
Spectrum 21
cps/eV
O
Si
Al
Na
Ca
Fe
Mg
K
K
Ca
Ca
Fe
Fe
keV

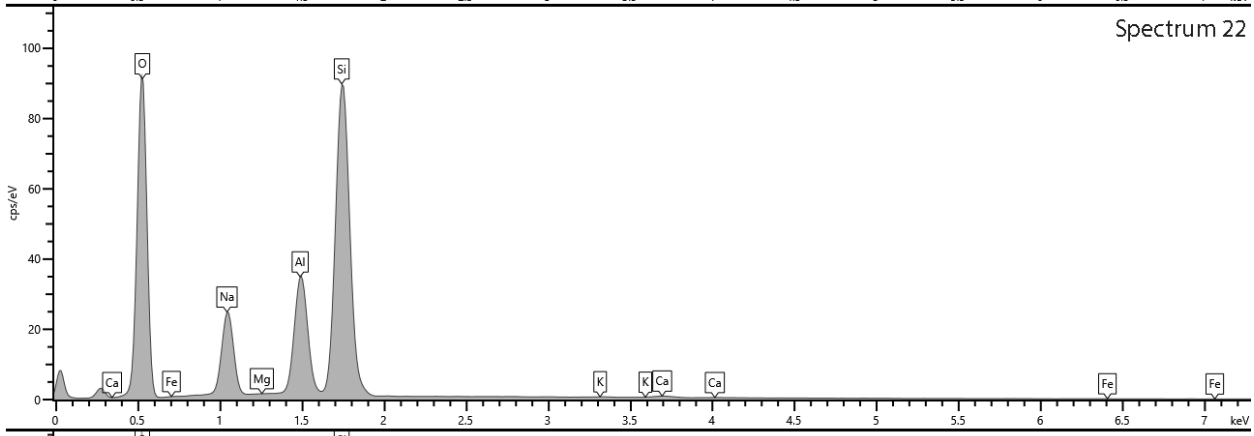
Spectrum 22
cps/eV
O
Si
Al
Na
Ca
Fe
Mg
K
K
Ca
Ca
Fe
Fe
keV

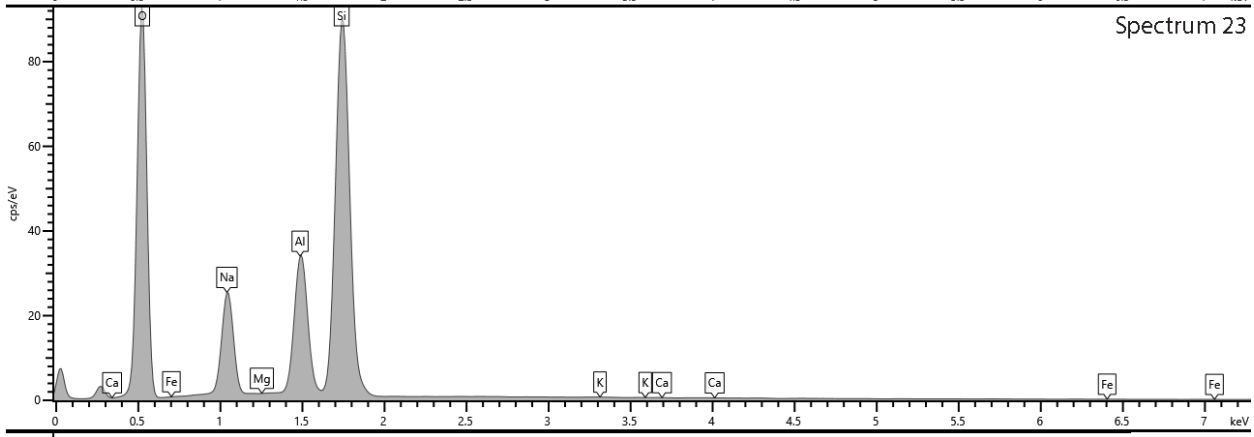
Spectrum 23
cps/eV
O
Si
Al
Na
Ca
Fe
Mg
K
K
Ca
Ca
Fe
Fe
keV

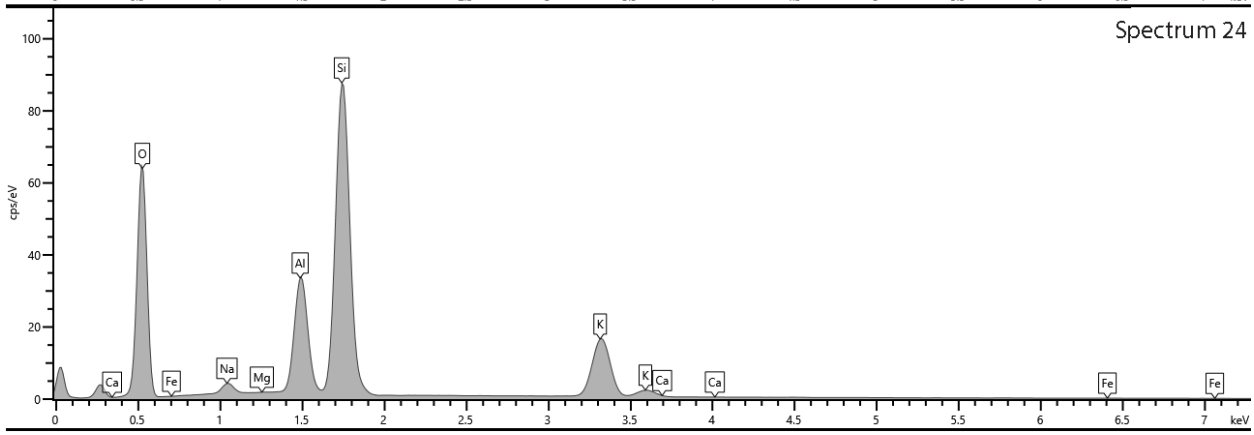
Spectrum 24
cps/eV
Si
O
Al
K
Na
Ca
Fe
Mg
K
Ca
Ca
Fe
Fe
keV

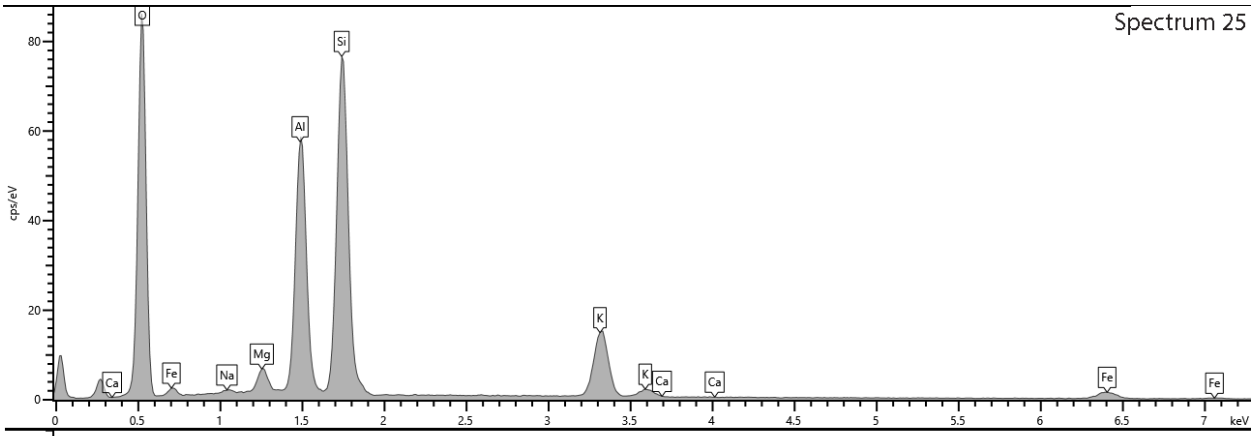
Spectrum 25
cps/eV
keV
O
Si
Al
K
Mg
Na
Fe
Ca

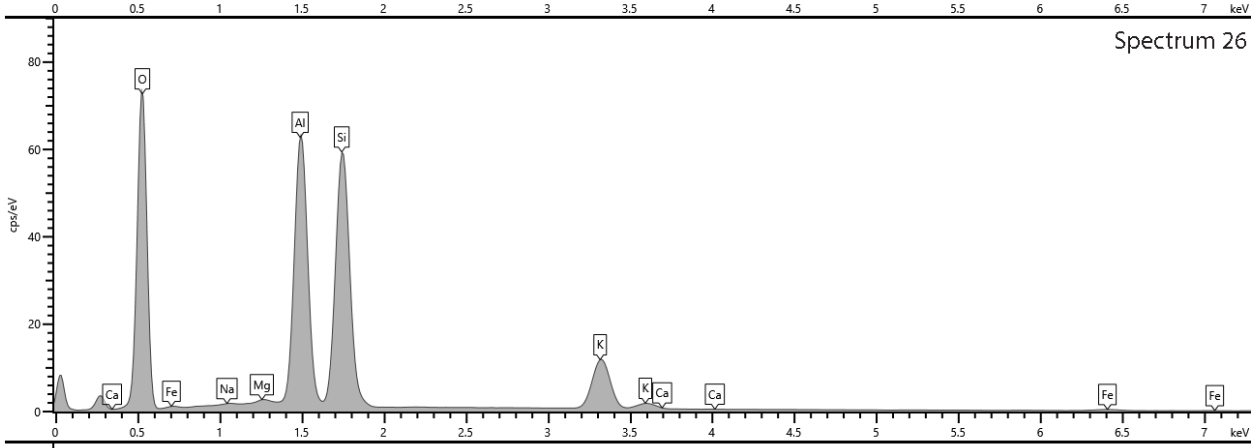
Spectrum 26
cps/eV
keV
O
Al
Si
K
Ca
Fe
Na
Mg

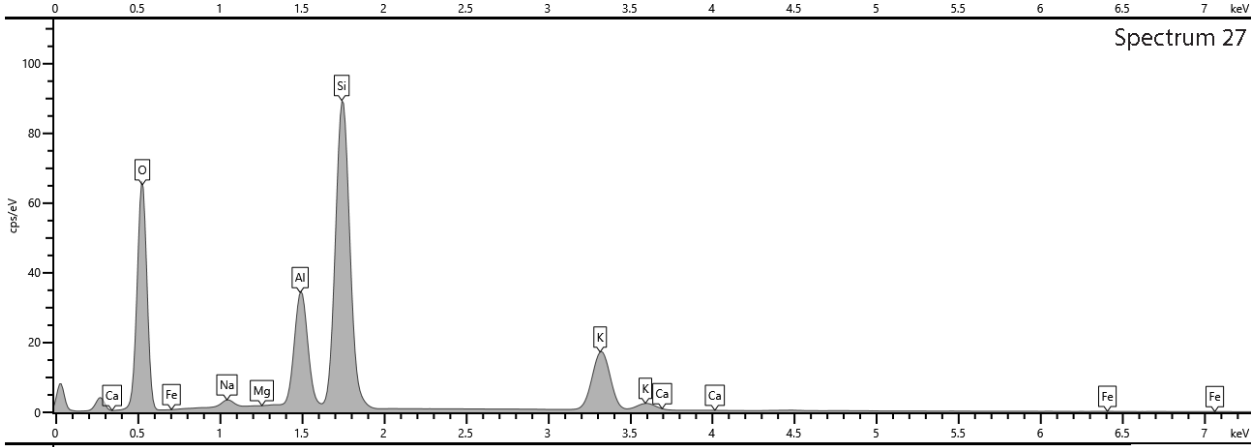
Spectrum 27
cps/eV
keV
Si
O
Al
K
Ca
Fe
Na
Mg

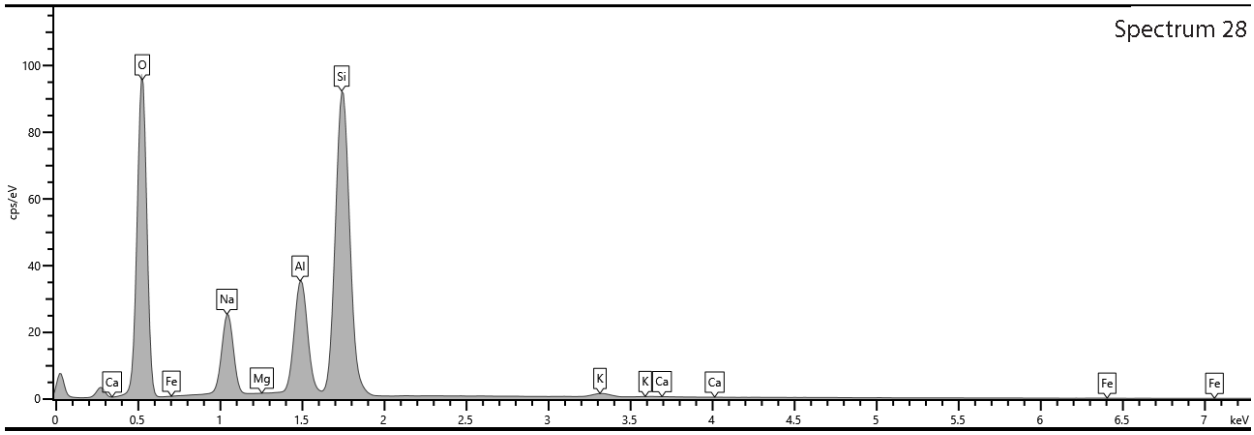
Spectrum 28
cps/eV
keV
O
Si
Al
Na
Ca
Fe
Mg
K

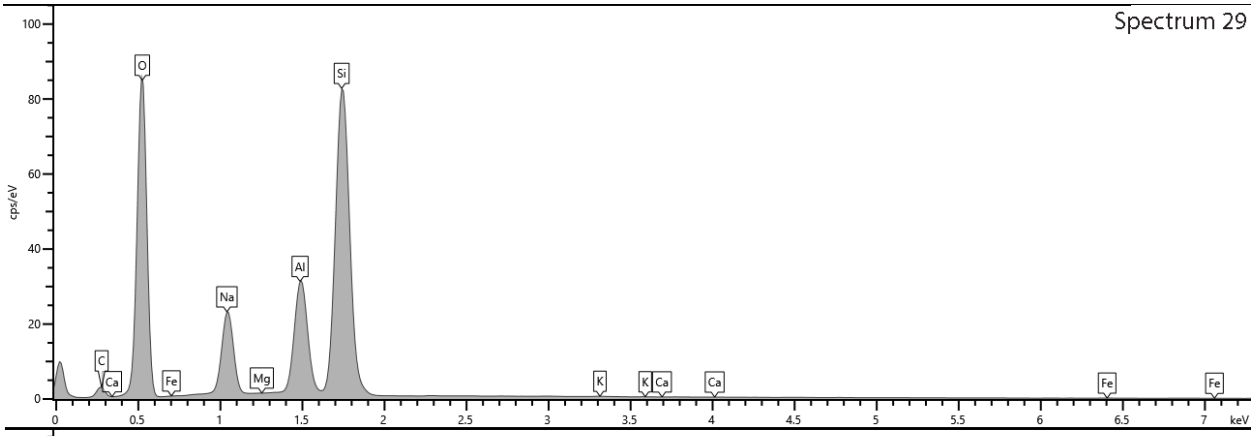
Spectrum 29
cps/eV
keV
O
Si
Na
Al
C
Ca
Fe
Mg
K
K
Ca
Ca
Fe
Fe

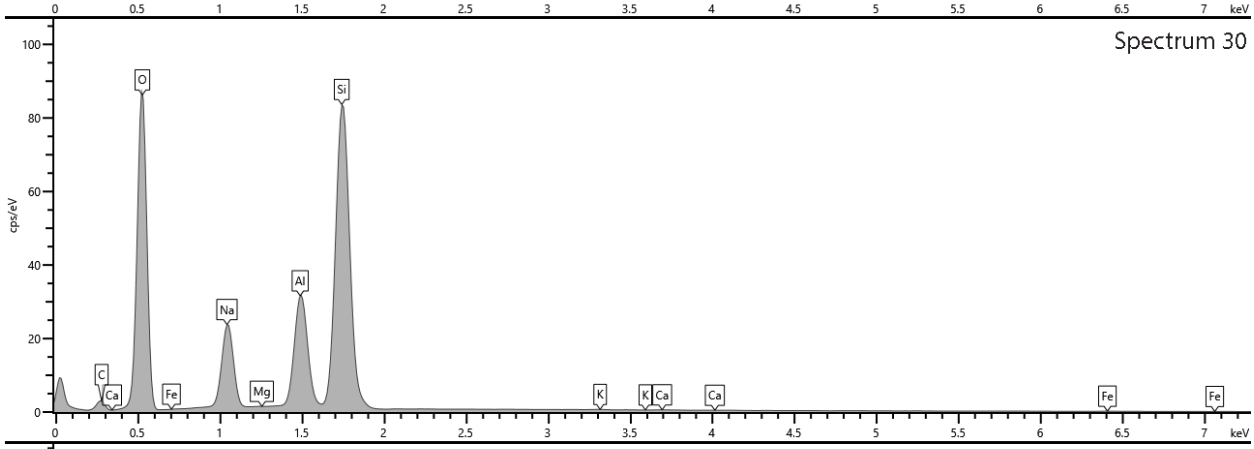
Spectrum 30
cps/eV
keV
O
Si
Na
Al
C
Ca
Fe
Mg
K
K
Ca
Ca
Fe
Fe

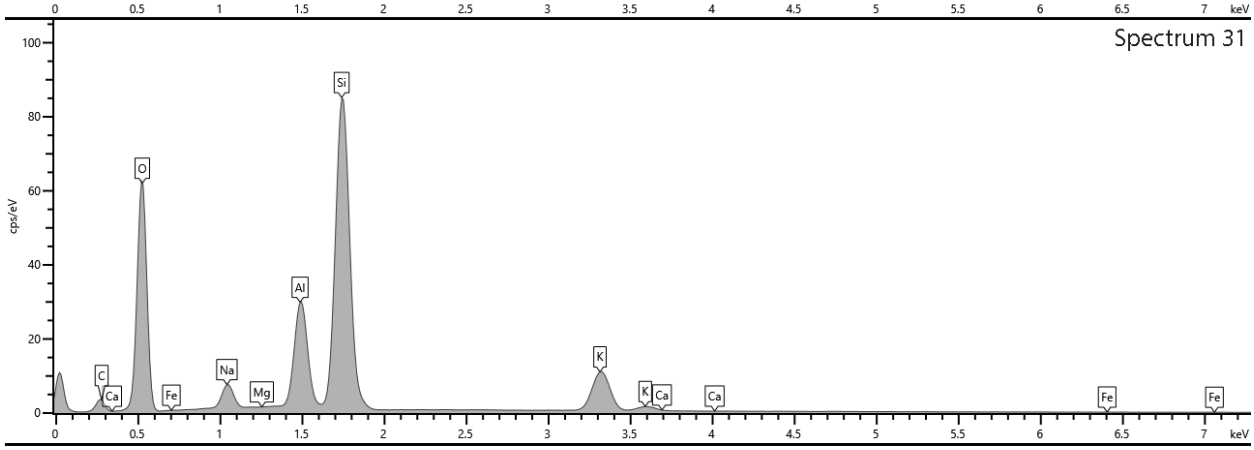
Spectrum 31
cps/eV
keV
Si
O
Al
K
Na
C
Ca
Fe
Mg
K
Ca
Ca
Fe
Fe

Appendix D: IPF-z Maps and Key for EBSD Samples

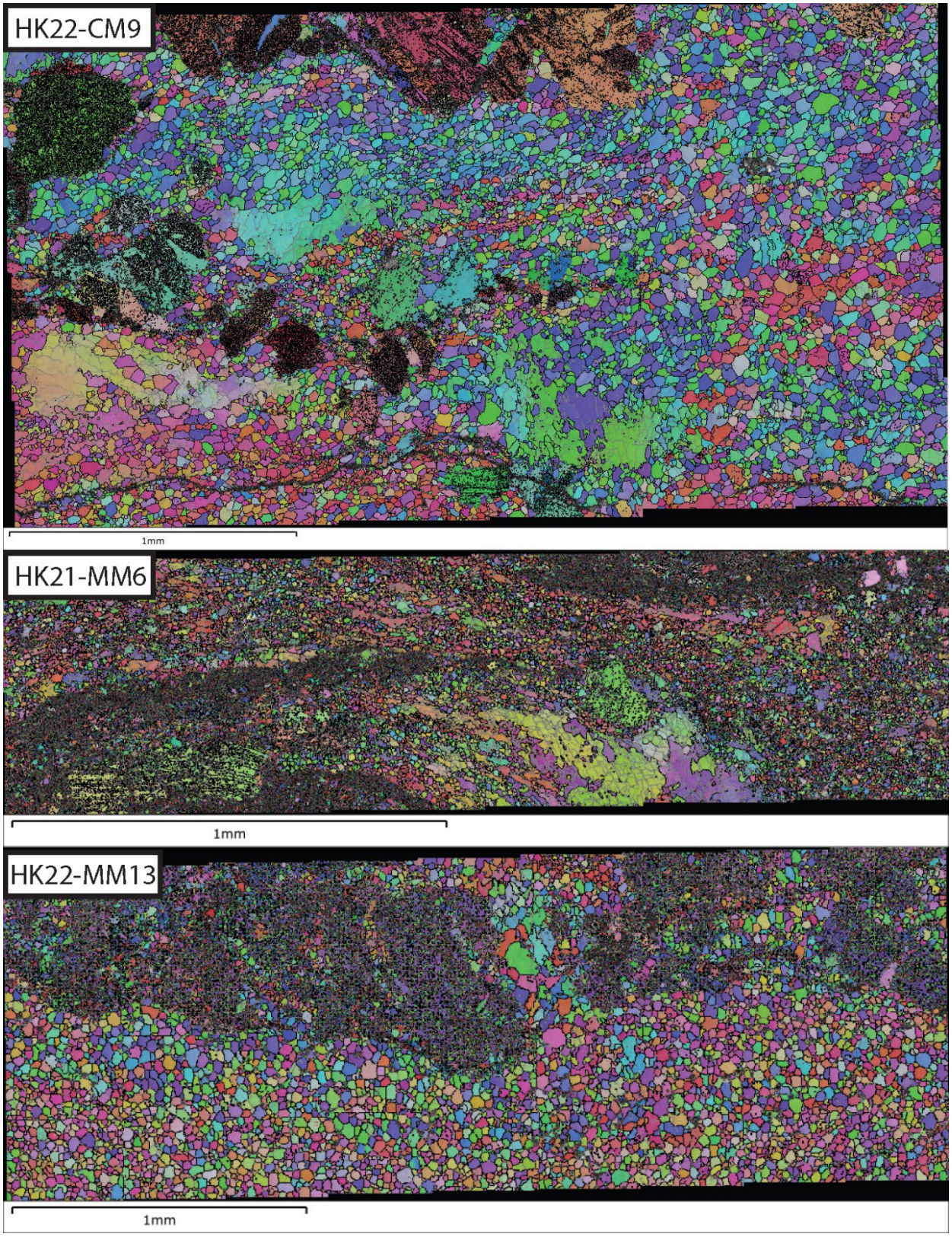

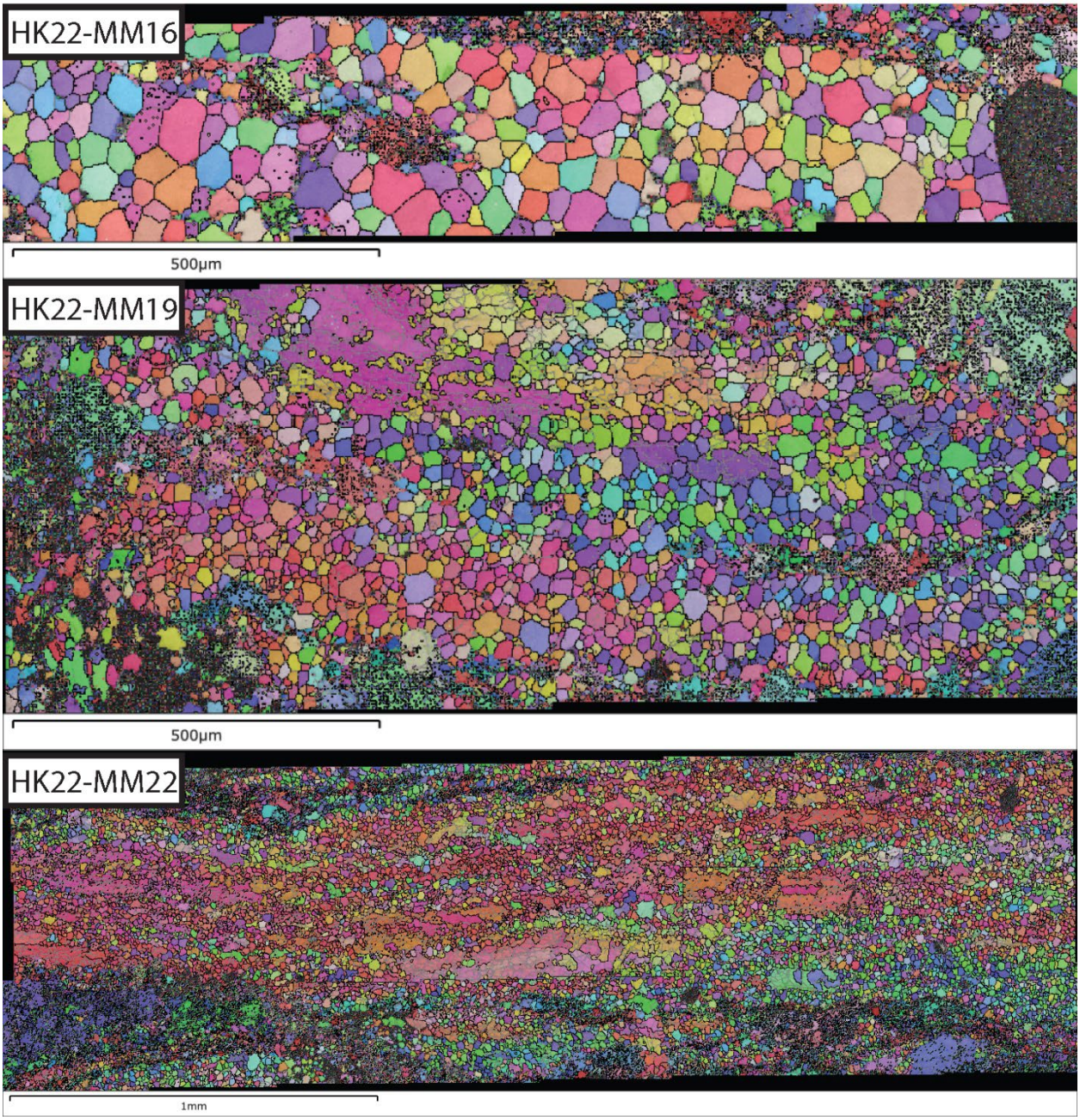
HK22-MM16
500μm
HK22-MM19
500μm
HK22-MM22
1mm

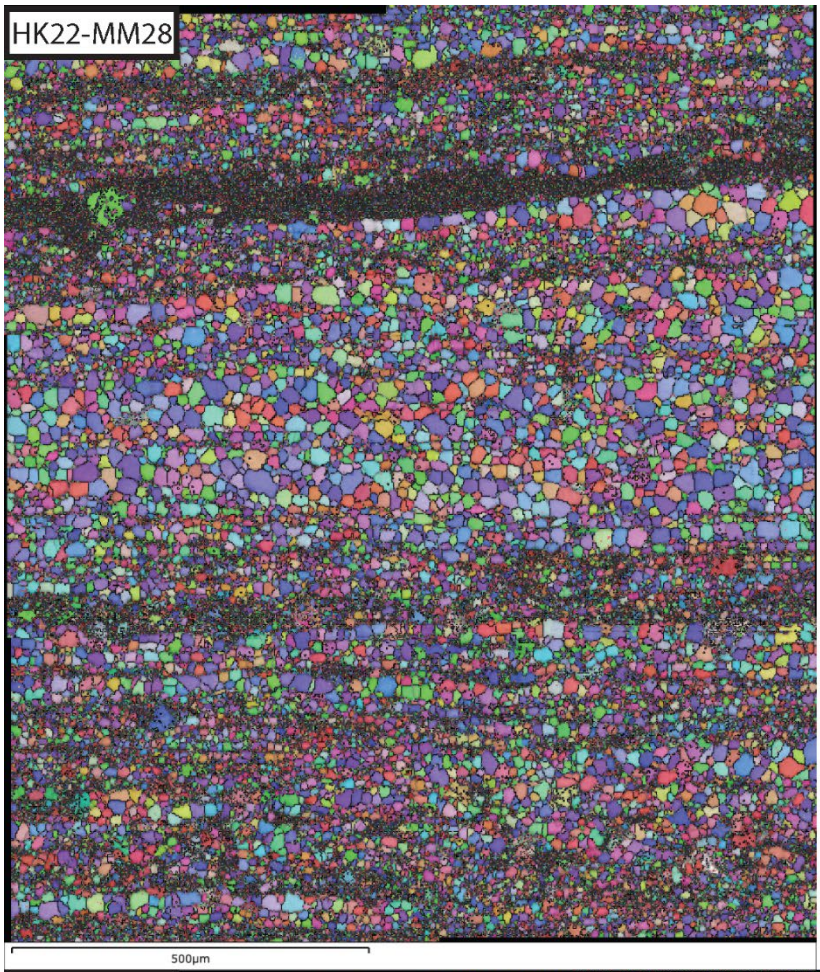
HK22-MM28
500µm

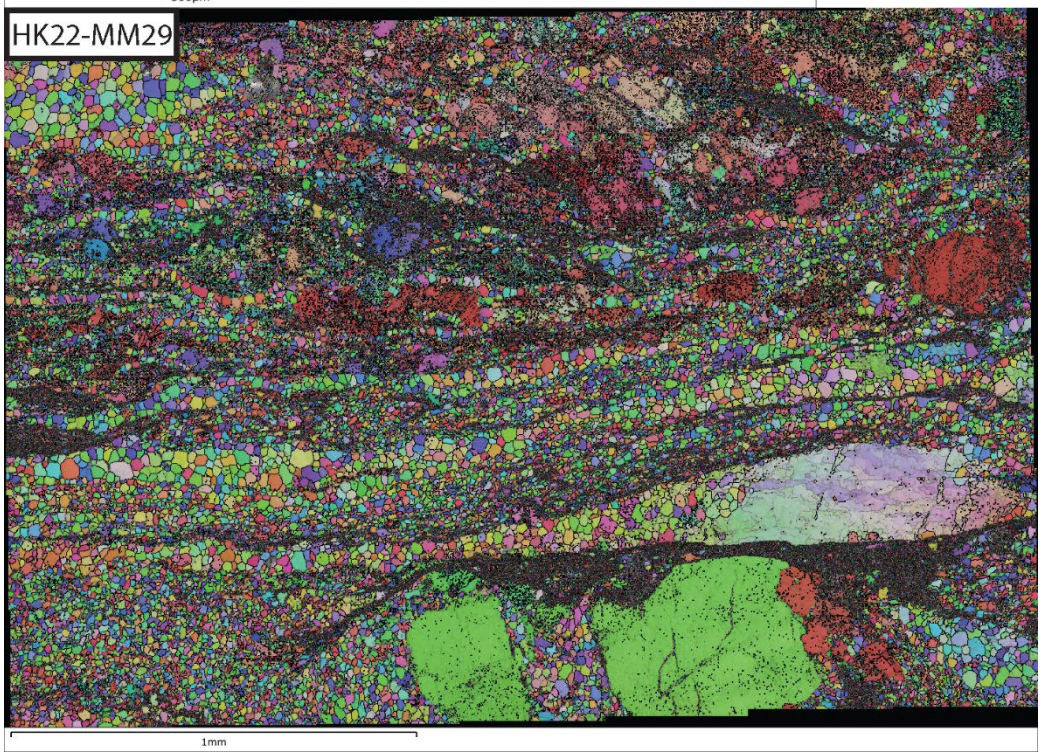
HK22-MM29
1mm

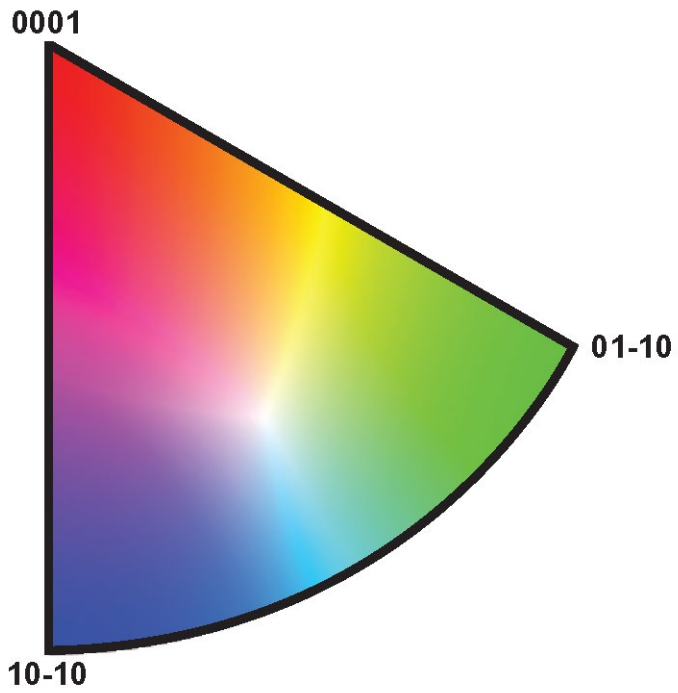
0001
01-10
10-10

Appendix E: Grain Size Distribution Histograms

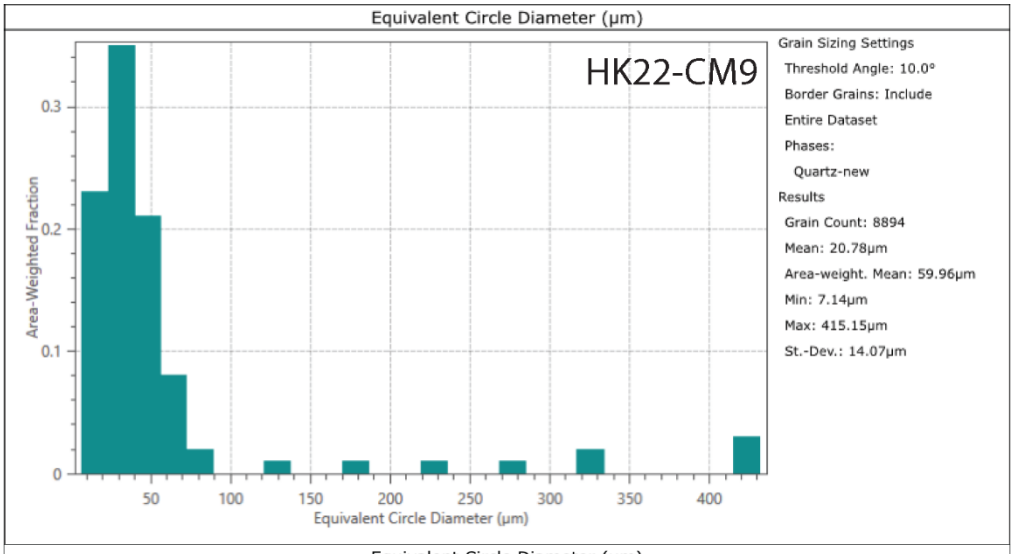

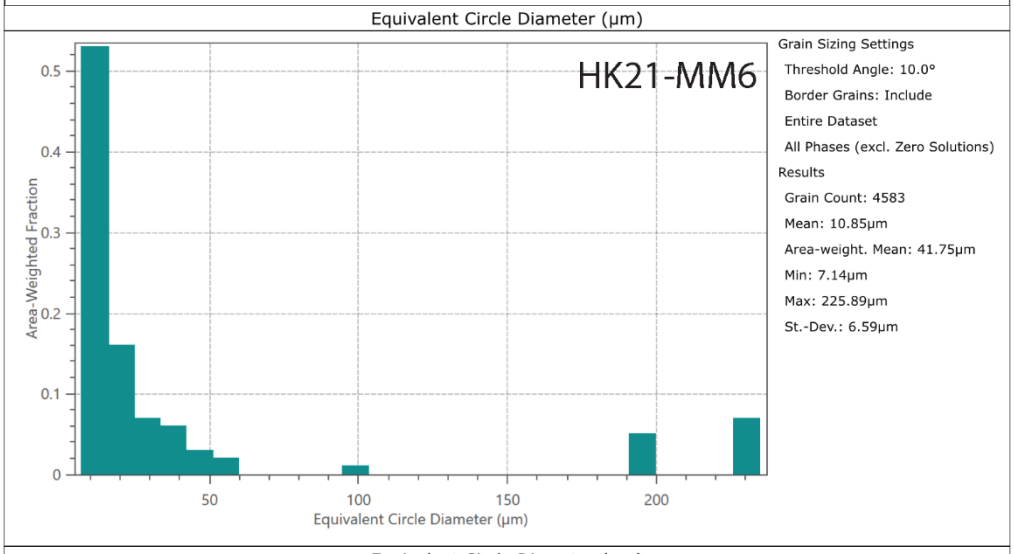

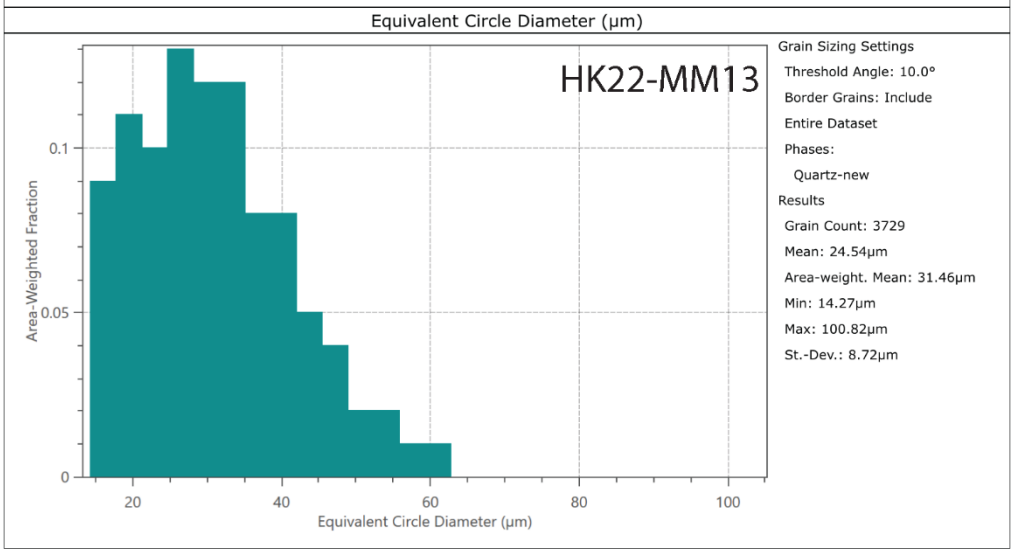

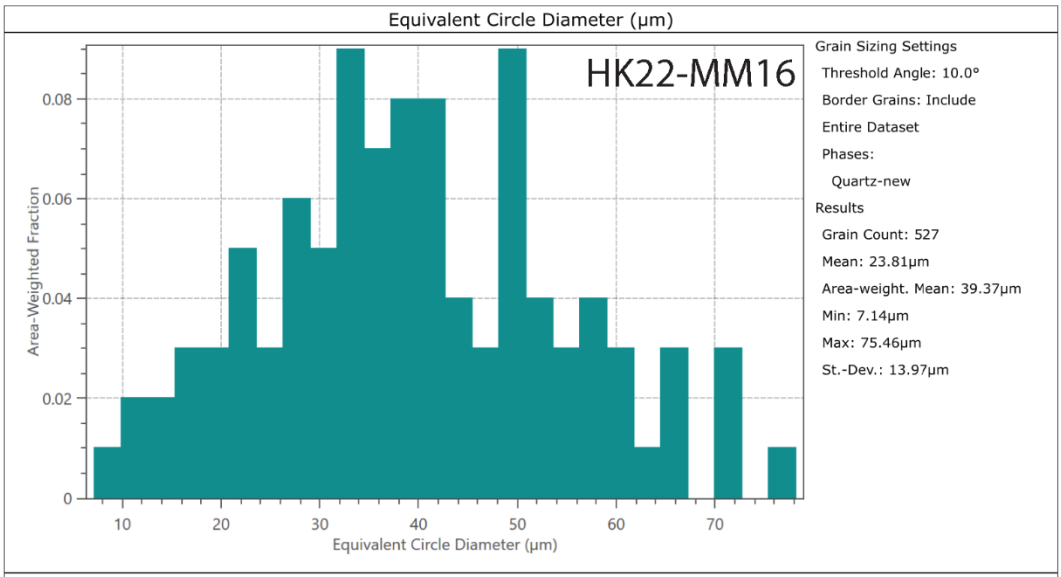
Equivalent Circle Diameter (µm)
HK22-MM16
Area-Weighted Fraction
0.08
0.06
0.04
0.02
0
10
20
30
40
50
60
70
Equivalent Circle Diameter (µm)
Grain Sizing Settings
Threshold Angle: 10.0°
Border Grains: Include
Entire Dataset
Phases:
Quartz-new
Results
Grain Count: 527
Mean: 23.81µm
Area-weight. Mean: 39.37µm
Min: 7.14µm
Max: 75.46µm
St.-Dev.: 13.97µm

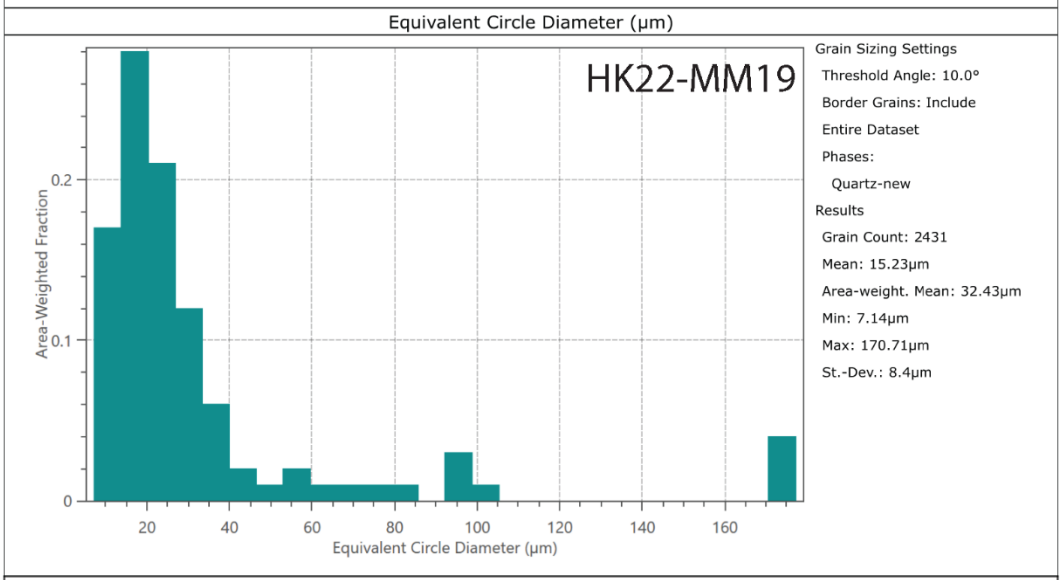
Equivalent Circle Diameter (µm)
HK22-MM19
Area-Weighted Fraction
0.2
0.1
0
20
40
60
80
100
120
140
160
Equivalent Circle Diameter (µm)
Grain Sizing Settings
Threshold Angle: 10.0°
Border Grains: Include
Entire Dataset
Phases:
Quartz-new
Results
Grain Count: 2431
Mean: 15.23µm
Area-weight. Mean: 32.43µm
Min: 7.14µm
Max: 170.71µm
St.-Dev.: 8.4µm

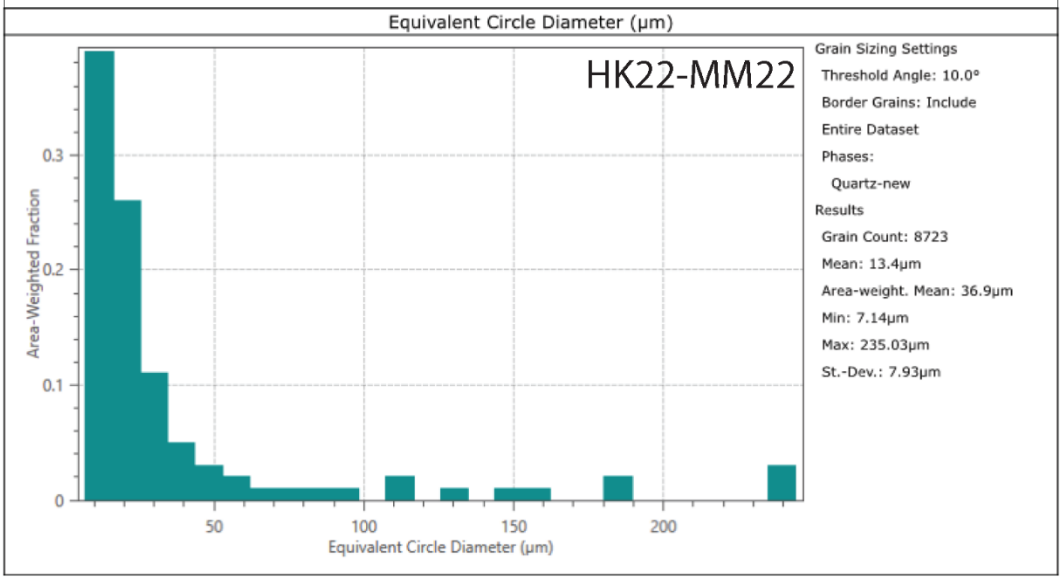
Equivalent Circle Diameter (µm)
HK22-MM22
Area-Weighted Fraction
0.3
0.2
0.1
0
50
100
150
200
Equivalent Circle Diameter (µm)
Grain Sizing Settings
Threshold Angle: 10.0°
Border Grains: Include
Entire Dataset
Phases:
Quartz-new
Results
Grain Count: 8723
Mean: 13.4µm
Area-weight. Mean: 36.9µm
Min: 7.14µm
Max: 235.03µm
St.-Dev.: 7.93µm

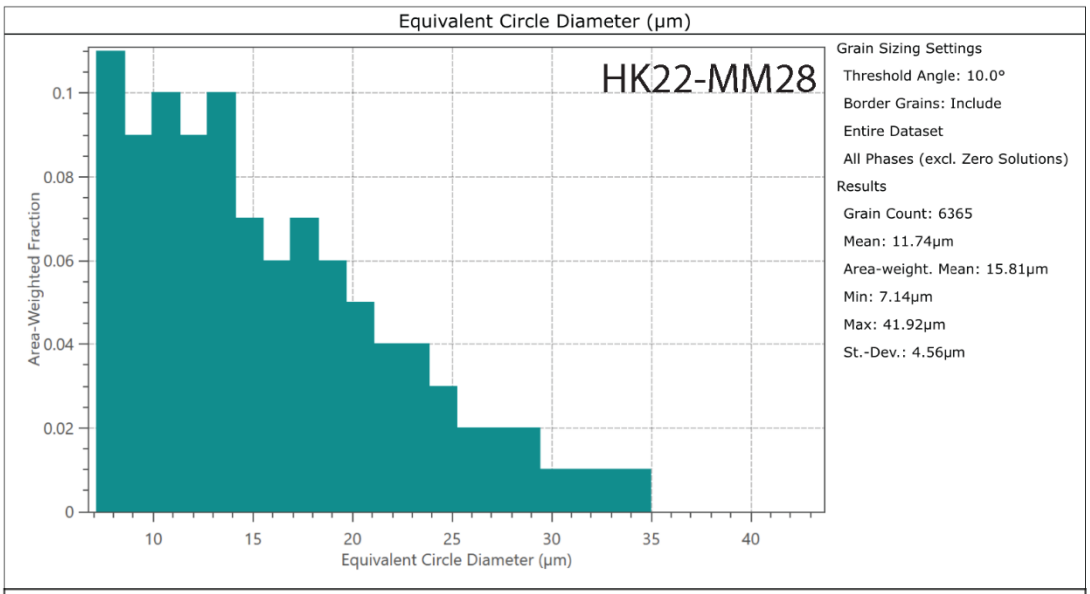
Equivalent Circle Diameter (µm)
HK22-MM28
Area-Weighted Fraction
0.1
0.08
0.06
0.04
0.02
0
10
15
20
25
30
35
40
Equivalent Circle Diameter (µm)
Grain Sizing Settings
Threshold Angle: 10.0°
Border Grains: Include
Entire Dataset
All Phases (excl. Zero Solutions)
Results
Grain Count: 6365
Mean: 11.74µm
Area-weight. Mean: 15.81µm
Min: 7.14µm
Max: 41.92µm
St.-Dev.: 4.56µm

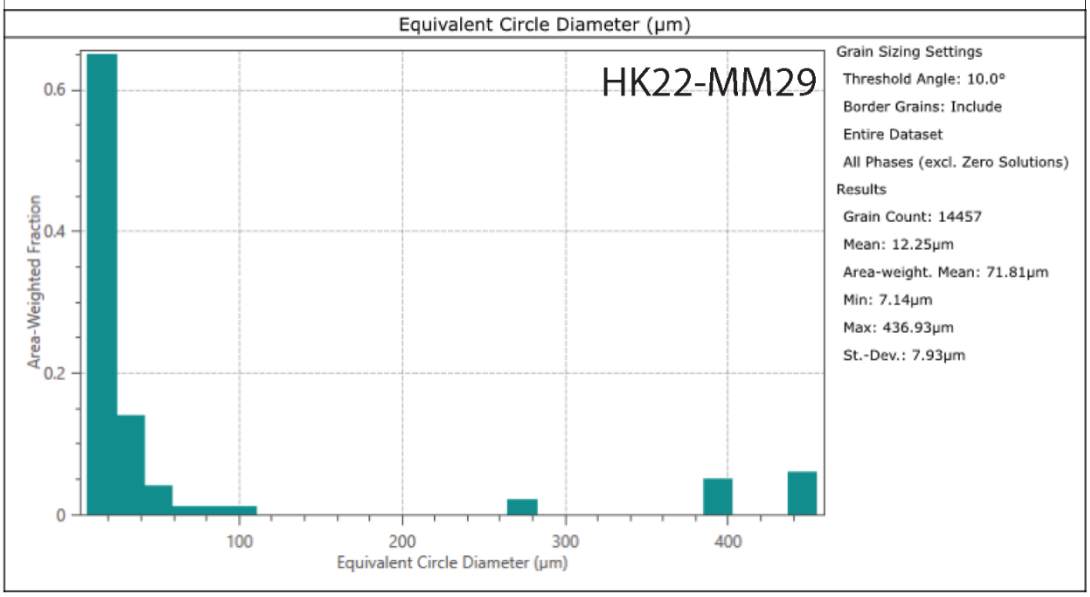
Equivalent Circle Diameter (µm)
HK22-MM29
Area-Weighted Fraction
0.6
0.4
0.2
0
100
200
300
400
Equivalent Circle Diameter (µm)
Grain Sizing Settings
Threshold Angle: 10.0°
Border Grains: Include
Entire Dataset
All Phases (excl. Zero Solutions)
Results
Grain Count: 14457
Mean: 12.25µm
Area-weight. Mean: 71.81µm
Min: 7.14µm
Max: 436.93µm
St.-Dev.: 7.93µm

Appendix F: Sample Locations

Sample Name	Latitude	Longitude	Lithology	Feature
HK21-MM4	35°40'9.18"N	115°42'57.41"W	Mylonitic Orthogneiss	Winters Pass Thrust
HK21-MM5	35°42'29.60"N	115°46'41.87"W	Mylonitic Orthogneiss	Winters Pass Thrust
HK21-MM6	35°42'16.06"N	115°46'28.24"W	Mylonitic Orthogneiss	Winters Pass Thrust
HK22-MM10	35°39'38.46"N	115°45'29.26"W	Mylonitic Orthogneiss	Winters Pass Thrust
HK22-MM12	35°39'41.00"N	115°45'22.16"W	Mylonitic Orthogneiss	Winters Pass Thrust
HK22-MM13	35°40'10.66"N	115°45'8.85"W	Mylonitic Orthogneiss	Winters Pass Thrust
HK22-MM16	35°40'14.38"N	115°45'3.45"W	Mylonitic Orthogneiss	Winters Pass Thrust
HK22-MM19	35°41'6.27"N	115°45'30.71"W	Mylonitic Orthogneiss	Kingston-Halloran Detachment
HK22-MM22	35°40'27.85"N	115°43'50.43"W	Mylonitic Orthogneiss	Kingston-Halloran Detachment
HK22-MM28	35°41'4.35"N	115°45'35.80"W	Mylonitic Quartzite	Kingston-Halloran Detachment
HK22-MM29	35°41'8.54"N	115°45'54.60"W	Mylonitic Orthogneiss	Winters Pass Thrust
HK22-CM4	35°34'5.56"N	115°39'59.30"W	Mylonitic Orthogneiss	Powerline Road Thrust
HK22-CM5	35°34'3.71"N	115°39'52.26"W	Mylonitic Orthogneiss	Powerline Road Thrust
HK22-CM9	35°31'25.18"N	115°39'3.23"W	Mylonitic Granite	Pachalka Thrust
HK22-CM11	35°31'25.25"N	115°39'9.14"W	Mylonitic Granite	Pachalka Thrust

REFERENCES

Axen, G. J., van Wijk, J. W., & Currie, C. A. (2018). Basal continental mantle lithosphere displaced by flat-slab subduction. *Nature Geoscience*, *11*(12), 961-964.

Balbas, A., Jung, C., & Konrad, K. (2023). The origin of the Musicians Seamount Province and its inferences for Late Cretaceous Pacific Plate Motion. *Marine Geology*, *465*, 107166.

Barba, W. K. (2020). *Tectonic evolution of the Tucki Mountain Metamorphic Core Complex, Southeastern California: Evidence for Late Cretaceous extension within the Sevier-Laramide Orogen* (Master's thesis, University of Nevada, Las Vegas).

Barth, A. P., & Schneiderman, J. S. (1996). A comparison of structures in the Andean orogen of northern Chile and exhumed midcrustal structures in southern California, USA: An analogy in tectonic style?. *International Geology Review*, *38*(12), 1075-1085.

Barth, A. P., Wooden, J. L., Coleman, D. S., & Fanning, C. M. (2000). Geochronology of the Proterozoic basement of southwesternmost North America, and the origin and evolution of the Mojave crustal province. *Tectonics*, *19*(4), 616-629.

Barth, N. C., Hacker, B. R., Seward, G. G., Walsh, E. O., Young, D., & Johnston, S. (2010). Strain within the ultrahigh-pressure Western Gneiss region of Norway recorded by quartz CPOs. *Geological Society, London, Special Publications*, *335*(1), 663-685.

Behrmann, J. H. (1987). A precautionary note on shear bands as kinematic indicators. Journal of Structural Geology, 9(5-6), 659-IN8.

Boyer, S. E., & Elliott, D. (1982). Thrust systems. *AAPG bulletin*, *66*(9), 1196-1230.

Brown, V. (2022). Integrating Microkinematic Crystallographic Vorticity Axis (CVA) Analysis and Petrochronology to Investigate the Temporal Development of Fabric Within a Transpressional Shear Zone, New Zealand (Doctoral dissertation, California State University, Northridge).

Buck, W. R. (1988). Flexural rotation of normal faults. *Tectonics*, *7*(5), 959-973.

Burchfiel, B.C., and Davis, G.A., 1971, Clark Mountain thrust complex in the Cordillera of southeastern California: Geologic summary and field trip guide, in Elders, W.A., ed., Geological Excursions in Southern California: Riverside, California, University of California, p. 1–28.

Burchfiel, B., & Davis, G. A. (1972). Structural framework and evolution of the southern part of the Cordilleran orogen, western United States. *American Journal of Science*, *272*(2), 97-118.

Burchfiel, B. C., Fleck, R. J., Secor, D. T., Vincelette, R. R., & Davis, G. A. (1974). Geology of the Spring Mountains, Nevada. *Geological Society of America Bulletin*, *85*(7), 1013-1022.

Burchfiel, B. C., & Davis, G. A. (1975). Nature and controls of Cordilleran orogenesis, western United States: Extensions of an earlier synthesis. American Journal of Science, 275(A), 363-396.

Burchfiel, B. C., and Davis, G. A., 1981, Mojave Desert and environs, in Ernst, W. G., eds., The geotectonic development of California (Rubey Volume 1): Englewood Cliffs, New Jersey, Prentice-Hall, p. 217–252.

Burchfiel, B. C., Davis, G. A., Weide, D. L., & Faber, M. L. (1988). Mesozoic thrust faults and Cenozoic low-angle normal faults, eastern Spring Mountains, Nevada, and Clark Mountains thrust complex, California. In *This extended land, geological journeys in the southern Basin and Range: Geological Society of America, Cordilleran Section Field Trip Guidebook* (pp. 87-106).

Burchfiel, B.C., Cowan, D.S., and Davis, G.A., 1992, Tectonic overview of the Cordilleran orogen in the western United States, in Burchfiel, B.C., et al., eds., The Cordilleran Orogen: Conterminous U.S.: Boulder, Colorado, Geological Society of America, Geology of North America, v. G-3, p. 407–414,

Burchfiel, B. C., & Royden, L. H. (1991). Antler orogeny: A Mediterranean-type orogeny. *Geology*, *19*(1), 66-69.

Calzia, J. P., Troxel, B. W., Wright, L. A., Burchfiel, B. C., Davis, G. A., & McMackin, M. R. (2000). *Geologic map of the Kingston Range, southern Death Valley, California* (No. 2000-412). US Geological Survey.

Carl, B. S., & Miller, C. F. (1991). Western Old Woman Mountains shear zone: Evidence for late ductile extension in the Cordilleran orogenic belt. *Geology*, *19*(9), 893-896.

Chapman, A. D., Kidder, S., Saleeby, J. B., & Ducea, M. N. (2010). Role of extrusion of the Rand and Sierra de Salinas schists in Late Cretaceous extension and rotation of the southern Sierra Nevada and vicinity. *Tectonics*, *29*(5).

Christiansen, E.H., Baxter, N.L., Ward, T.P., Zobell, E., Chandler, M.R., Dorais, M., Kowallis, B.J., & Clark, D.L. (2007). Cenozoic Soldiers Volcanic Field, Central Utah—Implications for the Transition to Extension-Related Magmatism in the Basin and Range Province.

Constenius, K. N. (1996). Late Paleogene extensional collapse of the Cordilleran foreland fold and thrust belt. *Geological Society of America Bulletin*, *108*(1), 20-39.

Crittenden, M. D., Coney, P. J., Davis, G. H., & Davis, G. H. (Eds.). (1980). *Cordilleran metamorphic core complexes* (Vol. 153). Geological Society of America.

Dahlen, F. A. (1990). Critical taper model of fold-and-thrust belts and accretionary wedges. *Annual Review of Earth and Planetary Sciences*, *18*(1), 55-99.

Davis, G. A., Fowler, T. K., Bishop, K. M., Brudos, T. C., Friedmann, S. J., Burbank, D. W., Parke, M. A. & Burchfiel, B. C. (1993). Pluton pinning of an active Miocene detachment fault system, eastern Mojave Desert, California. *Geology*, *21*(7), 627-630.

DeCelles, P. G. (2004). Late Jurassic to Eocene evolution of the Cordilleran thrust belt and foreland basin system, western USA. American Journal of Science, 304(2), 105-168.

DeCelles, P. G., Ducea, M. N., Kapp, P., & Zandt, G. (2009). Cyclicity in Cordilleran orogenic systems. *Nature Geoscience*, *2*(4), 251-257.

DeCelles, P. G., & Mitra, G. (1995). History of the Sevier orogenic wedge in terms of critical taper models, northeast Utah and southwest Wyoming. *Geological Society of America Bulletin*, *107*(4), 454-462.

Dickinson, W. R. (1971). Plate tectonic models of geosynclines. *Earth and Planetary Science Letters*, *10*(2), 165-174.

Dickinson, W. R. (2008). Accretionary Mesozoic–Cenozoic expansion of the Cordilleran continental margin in California and adjacent Oregon. *Geosphere*, *4*(2), 329-353.

Dumitru, T. A. (1990). Subnormal Cenozoic geothermal gradients in the extinct Sierra Nevada magmatic arc: Consequences of Laramide and post-Laramide shallow-angle subduction. *Journal of Geophysical Research: Solid Earth*, *95*(B4), 4925-4941.

Dumitru, T. A., Gans, P. B., Foster, D. A., & Miller, E. L. (1991). Refrigeration of the western Cordilleran lithosphere during Laramide shallow-angle subduction. *Geology*, *19*(11), 1145-1148.

Dunlap, W.J. (1997). Neocrystallization or cooling? 40Ar/39Ar ages of white micas from low-grade mylonites. Chemical Geology, Volume 143, Issues 3–4, Pages 181-203

Engebretson, D. C., Cox, A., & Thompson, G. A. (1984). Correlation of plate motions with continental tectonics: Laramide to Basin-Range. *Tectonics*, *3*(2), 115-119.

Faulds, James & Henry, Christopher & Hinz, Nick. (2005). Kinematics of the northern Walker Lane: An incipient transform fault along the Pacific–North American plate boundary. Geology. 33

Fleck, R. J., Mattinson, J. M., Busby, C. J., Carr, M. D., Davis, G. A., & Burchfiel, B. C. (1994). Isotopic complexities and the age of the Delfonte volcanic rocks, eastern Mescal Range, southeastern California: Stratigraphic and tectonic implications. *Geological Society of America Bulletin*, *106*(10), 1242-1253.

Fleck, R. J., & Carr, M. D. (1990). The age of the Keystone Thrust: laser-fusion 40Ar/39Ar dating of foreland basin deposits, southern Spring Mountains, Nevada. *Tectonics*, *9*(3), 467-476.

Friedmann, S. J., & Burbank, D. W. (1995). Rift basins and supradetachment basins: Intracontinental extensional end-members. *Basin Research*, *7*(2), 109-127.

Fossen, H. (2016). *Structural geology*. Cambridge university press.

Furlong, K. P. (1984). Lithospheric behavior with triple junction migration: An example based on the Mendocino triple junction. *Physics of the Earth and Planetary Interiors*, *36*(3-4), 213-223.

Gapais, D., & White, S. H. (1982). Ductile shear bands in a naturally deformed quartzite. *Textures and microstructures*, *5*(1), 1-17.

Giallorenzo, M. A., Wells, M. L., Yonkee, W. A., Stockli, D. F., & Wernicke, B. P. (2018). Timing of exhumation, Wheeler Pass thrust sheet, southern Nevada and California: Late Jurassic to middle Cretaceous evolution of the southern Sevier fold-and-thrust belt. GSA Bulletin, 130(3-4), 558-579.

Gerald, J. F., & Stünitz, H. (1993). Deformation of granitoids at low metamorphic grade. I: Reactions and grain size reduction. *Tectonophysics*, *221*(3-4), 269-297.

Giorgis, S., Michels, Z., Dair, L., Braudy, N., & Tikoff, B. (2017). Kinematic and vorticity analyses of the western Idaho shear zone, USA. *Lithosphere*, *9*(2), 223-234.

Graveleau, F., Malavieille, J., & Dominguez, S. (2012). Experimental modelling of orogenic wedges: A review. *Tectonophysics*, *538*, 1-66.

Goddard, R. M., Hansen, L. N., Wallis, D., Stipp, M., Holyoke III, C. W., Kumamoto, K. M., & Kohlstedt, D. L. (2020). A subgrain-size piezometer calibrated for EBSD. *Geophysical Research Letters*, *47*(23).

Hamilton, W., 1969, Mesozoic California and the underflow of Pacific mantle: Geological Society of America Bulletin, v. 80, p. 2409–2430,

Harrison, T. M., Célérier, J., Aikman, A. B., Hermann, J., & Heizler, M. T. (2009). Diffusion of 40Ar in muscovite. *Geochimica et Cosmochimica Acta*, *73*(4), 1039-1051.

Harrison, T.M., (1982). Diffusion of 40 Ar in hornblende. *Contributions to Mineralogy and Petrology*, *78*, 324-331.

Hazzard, J. C., 1937, Paleozoic section in the Nopah and Resting Springs Mountains, Inyo County, California: California Jour. Mines and Geology, v. 33, p. 273-339.

Hess, L. T. (2017). *Late Cretaceous extensional collapse of the southern Cordillera: Evidence from the Bristol and Granite mountains, SE California* (Doctoral dissertation, University of Nevada, Las Vegas).

Hess, L. T., and Wells, M. L., 2016, Development and disaggregation of a plutonic complex in SE California: Constraints on Late Cretaceous collapse of the Sevier orogen, National GSA

Hewett, D. F. (1956). *Geology and mineral resources of the Ivanpah quadrangle, California and Nevada* (Vol. 275). US Government Printing Office.

Hirth, G., & Tullis, J. A. N. (1992). Dislocation creep regimes in quartz aggregates. *Journal of structural geology*, *14*(2), 145-159.

Humphreys, E. D., Schmandt, B., Bezada, M. J., & Perry-Houts, J. (2015). Recent craton growth by slab stacking beneath Wyoming. *Earth and Planetary Science Letters*, *429*, 170-180.

Inger, S., Ramsbotham, W., Cliff, R. A., & Rex, D. C. (1996). Metamorphic evolution of the Sesia-Lanzo Zone, Western Alps: time constraints from multi-system geochronology. Contributions to Mineralogy and Petrology, 126(1), 152-168.

Jones, C. H., Farmer, G. L., Sageman, B., & Zhong, S. (2011). Hydrodynamic mechanism for the Laramide orogeny. *Geosphere*, *7*(1), 183-201.

Kirschner, D. L., Cosca, M. A., Masson, H., & Hunziker, J. C. (1996). Staircase 40/Ar39Ar spectra of fine-grained white mica: Timing and duration of deformation and empirical constraints on argon diffusion. *Geology*, *24*(8), 747-750.

Kruckenberg, S. C., Michels, Z. D., & Parsons, M. M. (2019). From intracrystalline distortion to plate motion: Unifying structural, kinematic, and textural analysis in heterogeneous shear zones through crystallographic orientation-dispersion methods. *Geosphere*, *15*(2), 357-381.

Kuiper, K. F., Deino, A., Hilgen, F. J., Krijgsman, W., Renne, P. R., & Wijbrans, A. J. (2008). Synchronizing rock clocks of Earth history. *science*, *320*(5875), 500-504.

Lagoeiro, L., & Barbosa, P. (2010). Nucleation and growth of new grains in recrystallized quartz vein: An example from banded iron formation in Iron Quadrangle, Brazil. *Journal of Structural Geology*, *32*(4), 595-604.

Lanphere, M. A. (1964). Geochronologic studies in the eastern Mojave Desert, California: Jour. *Geology*, *72*, 381-399.

Law, R. D. (2014). Deformation thermometry based on quartz c-axis fabrics and recrystallization microstructures: A review. *Journal of structural Geology*, *66*, 129-161.

Lawton, T. F., Cashman, P. H., Trexler Jr, J. H., & Taylor, W. J. (2017). The late Paleozoic southwestern Laurentian borderland. Geology, 45(8), 675-678.

Levy, D. A., Zuza, A. V., Haproff, P. J., & Odlum, M. L. (2021). Early Permian tectonic evolution of the Last Chance thrust system: An example of induced subduction initiation along a plate boundary transform. *Bulletin*, *133*(5-6), 1105-1127.

Lister, G. S., & Snoke, A. W. (1984). SC mylonites. *Journal of Structural Geology*, *6*(6), 617-638.

Livaccari, R. F., & Perry, F. V. (1993). Isotopic evidence for preservation of Cordilleran lithospheric mantle during the Sevier-Laramide orogeny, western United States. *Geology*, *21*(8), 719-722.

Liu, S., & Currie, C. A. (2016). Farallon plate dynamics prior to the Laramide orogeny: Numerical models of flat subduction. *Tectonophysics*, *666*, 33-47.

LoBianco, S. J. (2022). *Tectonostratigraphic Reconstruction of the Neoproterozoic Rift-To-Drift Transition in Southeast Death Valley*. University of California, Santa Barbara.

Lund, K. (2008). Geometry of the Neoproterozoic and Paleozoic rift margin of western Laurentia: Implications for mineral deposit settings. *Geosphere*, *4*(2), 429-444.

MacDonald, F.A., Prave, A.R., Petterson, R., Smith, E.F., Pruss, S.B., Oates, K., Waechter, F., Trotzuk, D., (2013). The Laurentian record of Neoproterozoic glaciation, tectonism, and eukaryotic evolution in Death Valley, California. Geol. Soc. Am. Bull.

Mahon, Robert & Dehler, Carol & Link, Paul & Karlstrom, Karl & Gehrels, George. (2014). Geochronologic and stratigraphic constraints on the Mesoproterozoic and Neoproterozoic Pahrump Group, Death Valley, California: A record of the assembly, stability, and breakup of Rodinia. Geological Society of America Bulletin. 126. 652-664.

McKenzie, D. (1978). Some remarks on the development of sedimentary basins. *Earth and Planetary science letters*, *40*(1), 25-32.

McMackin, M.R., (1987), Extension Tectonics in the Southeastern Kingston Range and Northern Mesquite Mountains: Reinterpretation of the Winters Pass "Thrust" Fault. [Unpublished Master's Thesis]. University of California Davis

Michels, Z. D., Kruckenberg, S. C., Davis, J. R., & Tikoff, B. (2015). Determining vorticity axes from grain-scale dispersion of crystallographic orientations. *Geology*, *43*(9), 803-806.

Miller, J. M. (1987). Paleotectonic and stratigraphic implications of the Kingston Peak-Noonday contact in the Panamint Range, eastern California. *The Journal of Geology*, *95*(1), 75-85.

Miranda, E. A., Brown, V., Schwartz, J. J., & Klepeis, K. A. (2023). Making sense of shear zone fabrics that record multiple episodes of deformation: Electron backscatter diffraction–derived and crystallographic vorticity axis–enhanced petrochronology. *Geology*, *51*(6), 591-596.

Neumann, B. (2000). Texture development of recrystallised quartz polycrystals unravelled by orientation and misorientation characteristics. *Journal of Structural Geology*, *22*(11-12), 1695-1711.

Noble, L. F. (1934). Rock formations of Death Valley, California. *Science*, *80*(2069), 173-178.

Quine, R. (2016). Quartz Crystal Preferred Orientation and Recrystallization Patterns from Naturally Deformed Rocks Under Constriction.

Passchier, C. W., & Simpson, C. (1986). Porphyroclast systems as kinematic indicators. *Journal of Structural Geology*, *8*(8), 831-843.

Passchier, C. W., & Trouw, R. A. (2005). *Microtectonics*. Springer Science & Business Media.

Pavlis, T. L., Rutkofske, J., Guerrero, F., & Serpa, L. F. (2014). Structural overprinting of Mesozoic thrust systems in eastern California and its importance to reconstruction of Neogene extension in the southern Basin and Range. *Geosphere*, *10*(4), 732-756.

Petterson, R., Prave, A. R., & Wernicke, B. P. (2011). *Chapter 41 Glaciogenic and related strata of the Neoproterozoic Kingston Peak Formation in the Panamint Range, Death Valley region, California* (Vol. 36, No. 1, pp. 459-465). London: The Geological Society of London.

Prave, A. R. (1999). Two diamictites, two cap carbonates, two δ13C excursions, two rifts: the Neoproterozoic Kingston Peak Formation, Death Valley, California. *Geology*, *27*(4), 339-342.

Piette-Lauzière N, Larson K.P., Kellett D.A., Graziani R., (2020) Intracrystalline vorticity record of flow kinematics during shear zone reactivation, Journal of Structural Geology, Volume 140,

Saleeby, J.B., (2003), Segmentation of the Laramide slab—Evidence from the southern Sierra Nevada region: Geological Society of America Bulletin, v. 115, p. 655–668

Schmid, S. M., & Casey, M. (1986). Complete fabric analysis of some commonly observed quartz c-axis patterns. *Mineral and rock deformation: Laboratory studies*, *36*, 263-286.

Simpson, C., & Schmid, S. M. (1983). An evaluation of criteria to deduce the sense of movement in sheared rocks. *Geological Society of America Bulletin*, *94*(11), 1281-1288.

Snow, J. K., & Wernicke, B. P. (2000). Cenozoic tectonism in the central Basin and Range; magnitude,rate, and distribution of upper crustal strain. American Journal of Science, 300(9), 659-719.

Stewart, J. H. (1970). Upper Precambrian and Lower Cambrian strata in the southern Great Basin California and Nevada.

Stipp, Michael & Stünitz, Holger & Heilbronner, Renée & Schmid, Stefan. (2002). The eastern Tonale fault zone: A 'natural laboratory' for crystal plastic deformation of quartz over a temperature range from 250 to 700 °C. Journal of Structural Geology. 24. 1861-1884.

Stipp, M., Tullis, J., Scherwath, M., & Behrmann, J. H. (2010). A new perspective on paleopiezometry: Dynamically recrystallized grain size distributions indicate mechanism changes. *Geology*, *38*(8), 759-762.

Strickland, A., Wooden, J. L., Mattinson, C. G., Ushikubo, T., Miller, D. M., & Valley, J. W. (2013). Proterozoic evolution of the Mojave crustal province as preserved in the Ivanpah Mountains, southeastern California. *Precambrian Research*, *224*, 222-241

Stone, P., & Stevens, C. H. (1988). Pennsylvanian and Early Permian paleogeography of east-central California: Implications for the shape of the continental margin and the timing of continental truncation. *Geology*, *16*(4), 330-333

Stünitz, H., & Gerald, J. F. (1993). Deformation of granitoids at low metamorphic grade. II: Granular flow in albite-rich mylonites. *Tectonophysics*, *221*(3-4), 299-324.

Tappert, M. C., Rivard, B., Tappert, R., & Feng, J. (2013). Using reflectance spectroscopy to estimate the orientation of quartz crystals in rocks. *The Canadian Mineralogist*, *51*(3), 405-413.

Ten Grotenhuis, S. M., Trouw, R. A. J., & Passchier, C. W. (2003). Evolution of mica fish in mylonitic rocks. *Tectonophysics*, *372*(1-2), 1-21.

Tikoff, B., Housen, B. A., Maxson, J. A., Nelson, E. M., Trevino, S., & Shipley, T. F. (2023). Hit-and-run model for Cretaceous–Paleogene tectonism along the western margin of Laurentia.

Urai, J. L., Means, W. D., & Lister, G. S. (1986). Dynamic recrystallization of minerals. *Mineral and rock deformation: laboratory studies*, *36*, 161-199.

Walker, J. D., Burchfiel, B. C., & Davis, G. A. (1995). New age controls on initiation and timing of foreland belt thrusting in the Clark Mountains, southern California. *Geological Society of America Bulletin*, *107*(6), 742-750.

Wells, M. L., 2016, A major mid-Cretaceous shortening event in the southern Sevier orogenic belt; Continental record of global plate reorganization?, vol. 48, no.7

Wells, M. L., Beyene, M. A., Spell, T. L., Kula, J. L., Miller, D. M., & Zanetti, K. A. (2005). The Pinto shear zone; a Laramide synconvergent extensional shear zone in the Mojave Desert region of the southwestern United States. Journal of Structural Geology, 27(9), 1697-1720.

Wells, M. L., & Hoisch, T. D. (2008). The role of mantle delamination in widespread Late Cretaceous extension and magmatism in the Cordilleran orogen, western United States. *Geological Society of America Bulletin*, *120*(5-6), 515-530.

Wernicke, B., & Axen, G. J. (1988). On the role of isostasy in the evolution of normal fault systems. *Geology*, *16*(9), 848-851.

Wernicke, B., Axen, G. J., & Snow, J. K. (1988). Basin and Range extensional tectonics at the latitude of Las Vegas, Nevada. *Geological Society of America Bulletin*, *100*(11), 1738-1757.

White, J. C., & White, S. H. (1981). On the structure of grain boundaries in tectonites. *Tectonophysics*, *78*(1-4), 613-628.

White, S. H., Burrows, S. E., Carreras, J., Shaw, N. D., & Humphreys, F. J. (1980). On mylonites in ductile shear zones. *Journal of structural geology*, *2*(1-2), 175-187.

Wibberley, C. (1999). Are feldspar-to-mica reactions necessarily reaction-softening processes in fault zones?. *Journal of Structural Geology*, *21*(8-9), 1219-1227.

Witkosky, R., & Wernicke, B. P. (2018). Subsidence history of the Ediacaran Johnnie Formation and related strata of southwest Laurentia: Implications for the age and duration of the Shuram isotopic excursion and animal evolution. *Geosphere*, *14*(5), 2245-2276.

Wright, L. A., Troxel, B. W., Williams, E. G., Roberts, M. T., & Diehl, P. E. (1976). Precambrian sedimentary environments of the Death Valley region, eastern California. *Geologic features of Death Valley, California: California Division of Mines and Geology Special Report*, *106*, 7-15.

Yonkee, W. A., Dehler, C. D., Link, P. K., Balgord, E. A., Keeley, J. A., Hayes, D. S., ... & Johnston, S. M. (2014). Tectono-stratigraphic framework of Neoproterozoic to Cambrian strata, west-central US: Protracted rifting, glaciation, and evolution of the North American Cordilleran margin. *Earth-Science Reviews*, *136*, 59-95.

Yonkee, W.A., and Weil, A.B., (2015), Tectonic evolution of the Sevier and Laramide belts within the North American Cordillera orogenic system: Earth-Science Reviews, v. 150, p. 531‑593

Zuo, J., Webb, A. A. G., Piazolo, S., Wang, Q., Müller, T., Ramírez-Salazar, A., & Haproff, P. J. (2021). Tectonics of the Isua supracrustal belt 2: Microstructures reveal distributed strain in the absence of major fault structures. *Tectonics*, *40*(3).

CURRICULUM VITAE

Hayden M. Kombrink

Hkombrink1@gmail.com

Education

• University of Nevada, Las Vegas – M.S. / Geoscience / 2024

• Arizona State University – B.S. / Earth and Space Exploration (Geological Sciences) / 2019

Research Experience

- M.S. Thesis (UNLV) – Advisor: Dr. Michael Wells
  - Structural geology, tectonics, EBSD, geochronology

Teaching Experience

• Graduate Teaching Assistantship – UNLV

- GEOL-101 / Physical Geology Lab / Fall 2021, Spring 2022, Spring 2023
- GEOL-448 / Field Geology I / Fall 2022 and Fall 2023
- GEOL-102 / Earth and Life Through Time / Spring 2024

Computer/technical skills

• Microsoft suite, Adobe illustrator/photoshop, MATLAB, AZtec crysta, Aztec

• Mineral separation

• Thin section preparation and petrographic analysis

References

• Dr. Michael Wells, Professor of Geoscience, University of Nevada, Las Vegas

Email: michael.wells@unlv.edu / phone: 702-895-3262

• Stephen Reynolds, Professor of Geology, Arizona State University

Email: sreynolds@asu.edu/ phone: 480-965-9049